Molecular tug-of-war regulates *Bacillus subtilis* elongasome dynamics and likely bacterial cell shape

Stuart Middlemiss

Thesis submitted in partial fulfilment of the requirements of the regulation for the degree of Doctor of Philosophy

Newcastle University

Faculty of Medical Sciences

Newcastle University Biosciences Institute

September 2022

Abstract

The shape and size of a bacterial cell is determined its peptidoglycan cell wall. During growth in many rod-shaped bacteria, the elongasome, comprising peptidoglycan synthases and other shape-determining proteins, assembles upon an MreB filament. The elongasome moves processively around the cell circumference, inserting new material into the cell wall. We investigated how Rod complex dynamics are regulated to construct a uniform, rod-shaped sacculus In the Gram-positive model organism *Bacillus subtilis*

I developed a novel method, single molecule Vertical Cell Imaging by Nanostructured Immobilisation (SM-VerCINI) that allows extended observation of MreB trajectories around the whole circumference of the cell. I found that MreB filaments are highly processive, travelling on average halfway around the cell circumference (1.6 μm) until pausing, reversing or unbinding. I found that the elongasome pauses and reverses far more frequent than previously thought, and the rate of elongasome pausing and reversal is set by cellular levels of elongasome synthase RodA. Further, RodA levels determine elongasome speed and processivity, which leads to subsequent changes in cell shape. These results are consistent with molecular motor tug-of-war, where synthesis complexes attach to opposite ends of the MreB filament, causing peptidoglycan synthesis termination and sudden reversal via tug-of-war competition. My results show that elongasome synthase tug-of-war is a key regulator of MreB filament dynamics and likely also determines cell shape in *B. subtilis*.

Acknowledgements

Firstly, I would like to thank Séamus Holden for continuous tutelage, mentorship and support over the past 4 years. It's been a real privilege working with you Séamus! I thank Henrik Strahl for supervision in the latter months of the project, gifting of unpublished strains, as well as invaluable discussions and support over the course of my time in the CBCB. I thank Kevin Whitley for gifting of code used to measure cell diameter. I am grateful to Kevin and Eleni Karinou for guidance and support during the project. Thanks to Jamie Grimshaw for proofreading this thesis. I thank Colin Harwood and Heath Murray for their mentorship and guidance throughout my time in academia. Thank you Daniela, Fran, Julie, Tom and all other CBCB colleagues who ensure reagents are always available and equipment is operational in the lab.

Adam, Grace, Jack, Shane, I thank you all for being such great friends over the past years. I couldn't have asked for better mates to go through this with. The Fam; Robbie and Tanzi, thank you so much for your unconditional support and being the best friends I could ever wish for. I also thank Phil and Mel for unwavering support over the years. Mam and Dad, also referred to as Jan and Howard, your support and belief throughout my education has been massive. I genuinely couldn't have done any of this without you. Rebecca, you have been by my side throughout this whole journey, supporting and believing in me and for that I am truly grateful.

A big thank you to you all.

Contents

Authorship Statement

Candidate Name: Stuart Adam Middlemiss

Principal Investigator: Dr Séamus Holden

Supervisor: Dr Henrik Strahl von Schulten

Title of PhD Thesis: Molecular tug-of-war regulates *Bacillus subtilis* elongasome dynamics and bacterial cell shape

Chapter 1: Introduction

I wrote this chapter with revisions made after comments from Séamus Holden.

Chapter 2: Materials and Methods

I wrote this chapter with revisions made by comments from Séamus Holden. Published code and protocols used are cited where applicable.

Chapter 3: Single-Molecule VerCINI reveals a highly processive elongasome with frequent state switching

Research questions in this chapter were defined by Séamus Holden. I carried out all experiments and data analysis. I wrote the custom code to analyse single-molecule tracking data acquired. Séamus Holden wrote code to deconvolve the effect of photobleaching on observe total track lifetimes of MreB-HaloTag (JF549) and to calculate confidence intervals on switching rates between states. I wrote this chapter with revisions made after comments from Séamus Holden.

Chapter 4: Effect of growth rate and MltG on MreB dynamics

Research questions in this chapter were defined by Séamus Holden and me. I acquired and analysed all data. Séamus Holden calculated confidence intervals for switching rates between states. I wrote this chapter with revisions made after comments from Séamus Holden.

Chapter 5: Effect of elongasome associated peptidoglycan synthases on MreB dynamics

Research questions in this chapter were defined by Séamus Holden and me. Unpublished strain HS553 was gifted by Henrik Strahl. Kevin Whitley wrote code to precisely measure cell diameter. Séamus Holden calculated confidence intervals for switching rates between states. I acquired and analysed all data. I wrote this chapter with revisions made after comments from Séamus Holden.

Chapter 6: Discussion

I wrote this chapter with revisions made after comments from Séamus Holden.

Publications

- Whitley KD, **Middlemiss S**, Jukes C, Dekker C, Holden S. High-resolution imaging of bacterial spatial organization with vertical cell imaging by nanostructured immobilization (VerCINI). Nat Protoc. 2022 Mar;17(3):847–69.

Attended Conferences

- 87th Harden Conference: Single-molecule bacteriology II, 11th – 14th July 2022, Milton Hill House, Oxfordshire: Poster presentation
- Subtillery, 14th – 18th June 2021, Virtual
- 60th Anniversary Meeting of the British Biophysical Society, 14th – 17th September 2020, Virtual
- Subtillery, 8th – 12th June 2020, Virtual
- 6th Great Wall Symposium, 25th – 27th September 2019, Institut Pasteur Paris, Poster presentation
- The physics of microorganisms II, 08th April 2019, The Institute of Physics, London: Poster presentation
- EMBL Conference: From Images to Knowledge with ImageJ & Friends, 06 - 08 December 2018, EMBL Heidelberg, Germany
- 6th Molecular Microbiology Meeting, 16th – 17th June 2018, Centre for Bacterial Cell biology Newcastle Upon Tyne: Poster presentation

List of figures

List of Tables

List of Abbreviations

ATP	Adenosine triphosphate
AFM	atomic force microscopy
CI	confidence intervals
DNA	deoxyribonucleic acid
erm	erythromycin
EDTA	ethylene diamine tetraacetic acid
et al.	*et alii* (and others)
FOV	field of view
GFP	green fluorescent protein
gDNA	genomic DNA
GlcNAc	N-acetylglucosamine
GTP	guanosine triphosphate
HiLO	highly inclined and laminated optical sheet microscopy
IPTG	Isopropyl ß-D-1-thiogalactopyranoside
JF	Janelia fluor
kan	kanamycin
Kb	kilo base pair
LB	Luria-Bertani medium
Linc	Lincomycin

MurNAc	N-acetylmuramic acid
NA	nutrient agar
OD_{600}	optical density measured at wavelength 600 nm
PBP	penicillin binding protein
PCR	polymerase chain reaction
R	resistant
ROI	region of interest
SEDS	shape, elongation, division, sporulation
SIM	structured illumination microscopy
SMM	Spizizen minimal media
SM	single molecule
SNR	signal to noise ratio
TIRF	total internal reflection microscopy
VerCINI	Vertical Cell Imaging by Nanostructured Immobilisation
WT	wild-type

Chapter 1: Introduction

The cell wall is an integral physiological feature of species within all domains of life. However, the makeup of the cell wall differs between domains. In bacteria, the cell wall is made up of peptidoglycan (Typas et al., 2011), whereas the archaean cell wall contains of various polysaccharides and glycoconjugates (Kandler and König, 1998). The plant cell wall is comprised of polysaccharide polymers such as cellulose, hemicellulose, and pectin (Zhang et al., 2021). It is thought that the cell wall in bacteria and archaea have evolved independently from a common ancestor lacking a cell wall and the cell wall in eukaryotes has evolved *via* lateral gene transfer (Niklas, 2004). Although co-evolution has produced cell walls varying in structure and composition, the function is remarkably consistent between domains. The cell wall is integral in cell shape, structure and growth as well as acting as a barrier to the extracellular environment (Dörr et al., 2019; Houston et al., 2016; Klingl et al., 2019). In all domains, synthesis of the cell wall is essential for growth and replication of the cell (Cosgrove, 2005; Klingl et al., 2019; Typas et al., 2011), with rare exceptions (Mercier et al., 2014)

Bacterial cell shape and size homeostasis is a fundamental cellular process. Cell shape and size is implicated in numerous biological processes such as nutrient acquisition, host-pathogen interactions and stress resistance (van Teeseling et al., 2017). Cell shape homeostasis is a key mechanism which must be tightly regulated to maintain a consistent shape and size at birth to maintain homogeneity over multiple generations (Westfall and Levin, 2017). Bacteria are found in an various morphologies (Cabeen and Jacobs-Wagner, 2005). The overall shape and size of a bacterium is determined by the cell wall (Typas et al., 2012), which also acts as a physical barrier to turgor pressure brought about by osmotic imbalance (Vollmer et al., 2008). This is especially important in Gram-positives like *Bacillus subtilis*, where around 20 atmospheres of turgor pressure is estimated to act upon the membrane and cell-wall during vegetative growth (Whatmore and Reed, 1990).

Synthesis and growth dynamics of the cell wall determines cell shape. This can be achieved by various modes of growth. In archaea such as *Streptomyces*, growth and cell shape is brought about by tip growth and branching of hyphae (Flärdh, 2003).

Bacteria come in various morphologies. The spherical *Staphylococcus* subtly changes shape throughout the cell cycle. Cells elongate slightly before a septum is formed for cell division, this allows cells to increase volume enough to maintain cell size over multiple generations (Monteiro et al., 2015). Some rod shaped bacteria like *Corynebacterium* grow similarly to *Streptomyces* and grow from the poles (Daniel and Errington, 2003). Most rod-shaped bacteria, including *Escherichia coli* and *B. subtilis* (model organisms for Gram-negatives and Gram-positives, respectively) grow by inserting nascent peptidoglycan throughout the long axis of the cell (Typas et al., 2012).

1.1 The peptidoglycan sacculus

1.1.1 Bacterial peptidoglycan structure

The cell wall, a mesh like sacculus made from peptidoglycan, is almost always essential for bacterial growth and viability. As a result, cell wall synthesis inhibitors are among the most effective antimicrobials (Sarkar et al., 2017). Gram-negative bacteria like *E. coli* contain a single, 3–6 nm peptidoglycan layer, whereas Gram-positives like *B. subtilis* harbour a much thicker 30 nm of peptidoglycan (Vollmer and Seligman, 2010).

Peptidoglycan is made up of glycan strands crosslinked by short peptides. Glycan strands are made up of alternate N-acetylglucosamine (GlcNAc) and N-acetylmuramic acid (MurNAc). GlcNAc and MurNAc monomers are linked by a pyrophosphate bridge to form a disaccharide unit (**Figure 1.1** (left)) (Münch and Sahl, 2015).

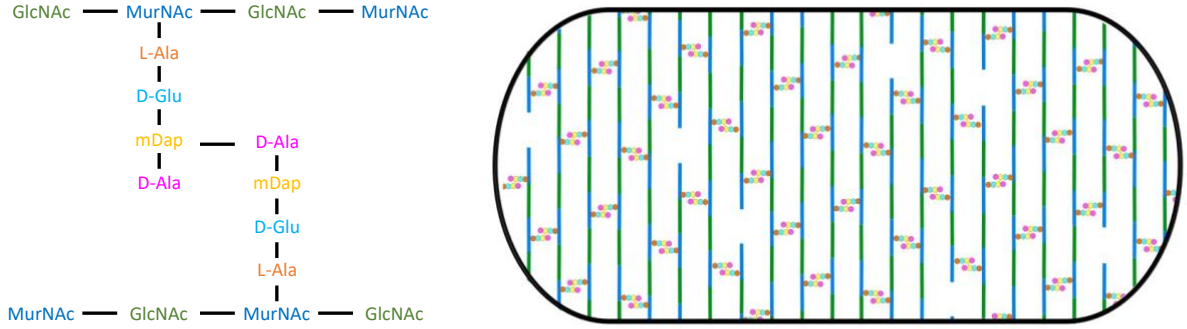

Figure 1.1. Schematic representation of the molecular makeup of peptidoglycan (left) and the overall sacculus structure (right).

Glycan strands have little flexibility and provide strength to the peptidoglycan (Höltje, 1998). Long glycan strands wrapping around the circumference of the cell (**Figure 1.1** (right)) are apparent by atomic force microscopy (AFM) (Pasquina-Lemonche et al., 2020). The length of glycans presumably plays an important role in maintenance of cell diameter as they provide the inward force against the turgor pressure of the cell. Glycan strands have short (3-5 residues), protruding peptides, which crosslink to make the mesh-like peptidoglycan macromolecule (Typas et al., 2012). The pentapeptdes vary in composition between species and growth conditions, but are typically made up of L-alanine (L-Ala), D-glutamine (D-iGlu), meso-diaminopimelic acid (mDap), D-alanine (D-Ala), D-Ala, as in *B. subtilis* and *E. coli* (Atrih et al., 1999, p. 5; Glauner, 1988). Most cross linkages occur between the carboxyl group of the D-Ala at residue 4 and the amino group of m-Dap at residue 3 (Heijenoort and Gutmann, 2000). In *B. subtilis,* but not *E. coli,* the carboxyl group of mDap is amidated (Dajkovic et al., 2017).

The specific architecture of peptidoglycan is an evolving field, with glycan strand length being a somewhat elusive feature. Most of the pioneering labs in peptidoglycan research focus on Gram-negative bacteria, owing to the technical difficulties of isolating and measuring the multi-layered Gram-positive peptidoglycan, compared to the uniformity of the single-layered *E. coli* peptidoglycan. As a result, there is much more published data referring to *E. coli* peptidoglycan in comparison to that of *B. subtilis*. Historically, glycan strand length in *E. coli* peptidoglycan has been estimated around 20-40 nm long, with each disaccharide unit measuring 1 nm, using reversed-phase high-performance liquid chromatography (Harz et al., 1990), by quantification of the muropeptides with 1,6-anhydroMu*N*Ac residues, which are found at the termini of a glycan strand (Glauner et al., 1988; Höltje et al., 1975). Glycan strand length is dependent on strain and growth conditions (Vollmer and Seligman, 2010). Recently, in the Foster group, Turner and colleagues have actually measured glycan strands around 200 nm long in *E. coli*, using AFM (Turner et al., 2018), the first findings of such long glycan strands in Gram-negative bacteria.

In Gram-positive bacteria, glycan strands have been found to be much longer. Early work found *B. subtilis* glycan strands to be around 100 nm in length (Ward, 1973), but as in *E. coli*, AFM studies in the Foster lab found this to be an underestimation; Hayhurst *et al.* found glycan strands in *B. subtilis* to be up to 5 microns in length (Hayhurst et al., 2008). The

differences between *E. coli* and *B. subtilis* could reveal more detail about the function of peptidoglycan in Gram-positives compared to Gram-negatives. Perhaps the difference in length of glycan strands is linked to the resistance against turgor pressure, which is much higher in Gram-positives.

The AFM work carried out in the Foster lab has given the longest glycan strand length measurements for *B. subtilis* and *E. coli* to date. The technique is somewhat limited though. The use of AFM to measure glycan strand length requires peptidoglycan isolation and cannot be carried out *in vivo.* (Jalili and Laxminarayana, 2004). In addition, the isolation and purification of peptidoglycan is laborious (Hayhurst et al., 2008; Turner et al., 2018), making analysis of various strains and growth conditions time consuming and sample-size limiting.

1.1.2 Peptidoglycan synthesis

Peptidoglycan synthesis is imperative in bacterial growth throughout the cell cycle and must be highly coordinated to ensure that after division, daughter cells obtain adequate size, volume and a whole genome (Reyes-Lamothe and Sherratt, 2019). In the longitudinally growing *B. subtills*, cell division, specifically septum placement and timing of division is crucial to ensure a whole chromosome is inherited by each daughter cell after division. This is aided by the nucleoid occlusion system, which prevents the chromosome being broken by the septum (Wu and Errington, 2011). In addition, the timing of cell division determines cell length as elongation rate remains constant throughout the cell cycle (Taheri-Araghi et al., 2015).

Peptidoglycan synthesis begins in the cytoplasm with the production of Lipid II (**Figure 1.2**). This is the peptidoglycan precursor, comprised of a disaccharide unit and a pentapeptide (Münch and Sahl, 2015). The multistage process begins with the synthesis of lipid I, which is made up of MurNAc, UDP and pentapeptide. This is synthesised by MurA-F, Ddl, Alr, DadX, MurI in the cytoplasm, and and MraY at the membrane (**Figure 1.2**) (van Heijenoort, 2007; VanNieuwenhze et al., 2001). MurG then catalyses the transfer of the GlcNAc moiety from UDP-GlcNAc to lipid I, forming Lipid II (Bouhss et al., 2008; van Heijenoort, 2007). Lipid II is then translocated across the membrane by then flipase, MurJ (Meeske et al., 2015), using an alternating access mechanism (Kuk et al., 2019; Kumar et al., 2018). On the extracellular side of the membrane, disaccharide units of lipid II are polymerised by a glycosyltransferase

(glycosyltransferase) producing a glycan chain (**Figure 1.2**) (Vollmer et al., 2008), releasing UDP, which is recycled for further lipid II transport (Egan Alexander J. F. et al., 2015). After this, pentapeptides are crosslinked by a dd-transpeptidase (transpeptidase), a reaction that cleaves the D-Ala residue at position 5 of the pentapeptide and results in the incorporation of the nascent glycan strand into the existing peptidoglycan sacculus (Vollmer et al., 2008). This is carried out by Penicillin binding proteins (PBPs). PBPs can be monofunctional, with either glycosyltransferase or transpeptidase activity, or be bifunctional and have both (Sauvage et al., 2008). Some SEDS (shape, elongation, division and sporulation) proteins also have glycosyltransferase and transpeptidase activity (Emami et al., 2017).

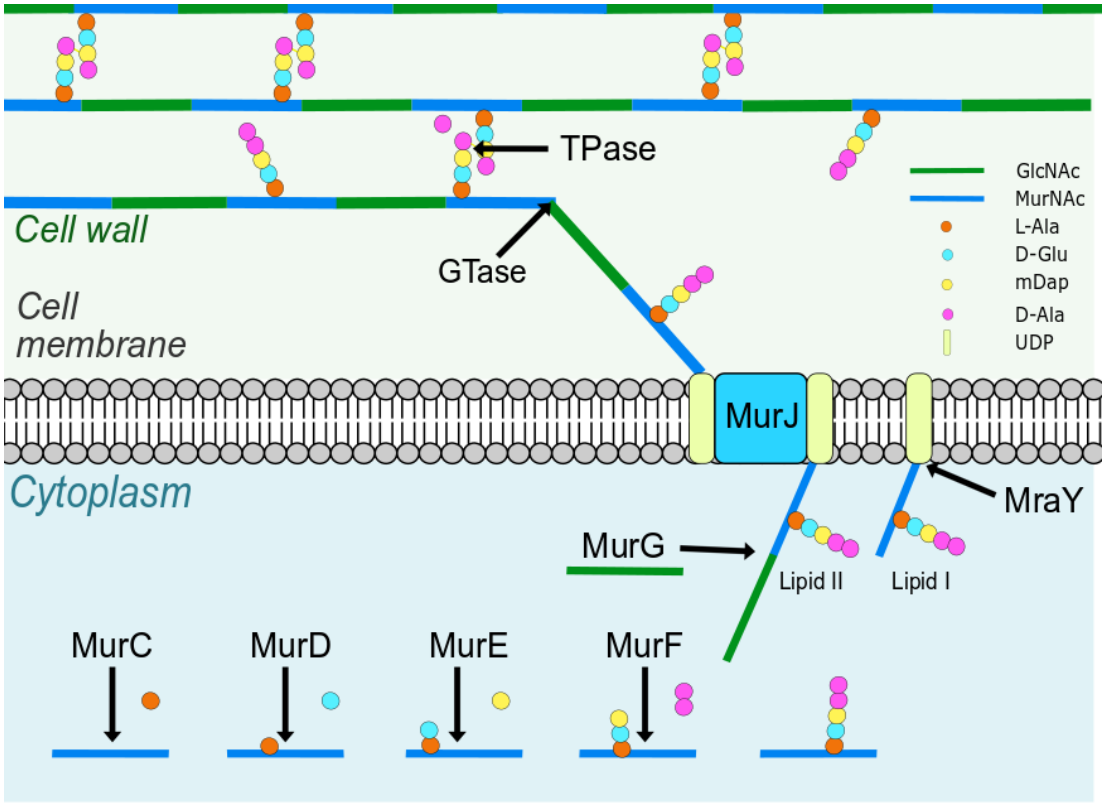

Figure 1.2. Schematic Representation of peptidoglycan synthesis. The peptidoglycan precursor, lipid II, is synthesised in the cytoplasm before insertion into the existing cell wall. Adapted from (Typas et al., 2011)

Peptidoglycan hydrolases also aid the maintenance of a viable sacculus, allowing the insertion of nascent peptidoglycan into the existing structure (Vollmer et al., 2008). Hydrolases cleave and break down peptidoglycan from the cell wall, leading to up to half of the existing peptidoglycan being removed from the sacculus in Gram-positives, with the cleaved material

being recycled and incorporated into nascent peptidoglycan (Johnson et al., 2013; Reith and Mayer, 2011). Cell wall turnover products can also regulate antibiotic resistance expression (Johnson et al., 2013). Hydrolases also allow cleavage of peptidoglycan at the septum and subsequent separation of two daughter cells (Heidrich et al., 2001).

Peptidoglycan synthesis and insertion into the sacculus is a highly dynamic process carried out throughout the side wall of the cell and at the septum by the elongasome and the divisome, respectively. Cell length homeostasis is maintained by a constant rate of nascent peptidoglycan insertion and cellular elongation, together with the timing of cell division, which is onset by the accumulation of cell division proteins which form the divisome (Taheri-Araghi et al., 2015).

The divisome constructs the septum at mid cell, which is eventually cleaved as two daughter cells separate after division. The elongasome, a multiprotein complex, with cytoplasmic, transmembrane and extracellular components, is responsible for peptidoglycan insertion along the side wall of the cell throughout the vegetative cell cycle and must be highly robust in order to maintain constant cellular elongation throughout the cell cycle over multiple generations.

1.2 The elongasome

The elongasome is a complex of proteins associated with cell shape and peptidoglycan synthesis. The multiprotein machine spans from the cytoplasm, through the membrane into the extracellular space, and the periplasm in Gram-positives and Gram-negatives, respectively. The elongasome is coordinated by MreB (van Teeffelen and Renner, 2018) and contains a variety of proteins required for maintenance of cell shape (**Figure 1.3**).

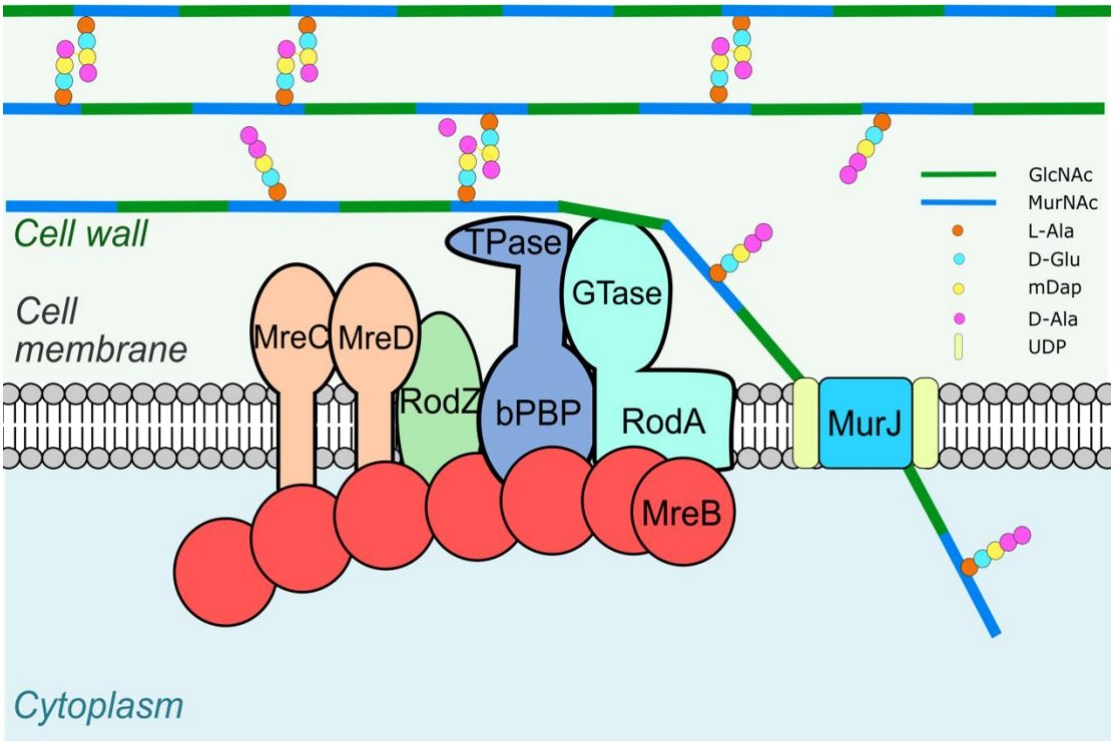

Figure 1.3. Schematic representation of the *B. subtills* elongasome and nascent peptidoglycan insertion. Lipid II is translocated across the membrane by MurJ before disaccharide polymerisation by glycosyltransferase proteins. Nascent glycan strand is inserted into the existing layer by crosslinking of peptide chains by transpeptidase proteins.

PBPs are integral to the elongation process. PBPH and PBP2A are individually non-essential, mutually redundant class B PBPs (bPBP)s (Kobayashi et al., 2003). The pair have transpeptidase activity during elongation (Wei et al., 2003). Both of these PBPs have been found to co-localise with MreB and the rest of the elongasome under certain conditions (Domínguez-Escobar et al., 2011; Garner et al., 2011). Under normal conditions, PBPH co-localises with the elongasome (Domínguez-Escobar et al., 2011), whereas PBP2A is diffusely

distributed throughout the membrane (Scheffers et al., 2004). In a *ΔpbpH* background, PBP2A takes over from PBPH and co-localises with the elongasome (Domínguez-Escobar et al., 2011; Garner et al., 2011). The essential RodA was recently determined to provide the glycosyltransferase activity of the elongasome (Emami et al., 2017). RodA is membrane associated, and co-localises with the elongasome (Domínguez-Escobar et al., 2011).

Another component of the elongasome is RodZ, which is required for correct rod-shape formation (Jones et al., 2001). RodZ has three distinct domains: cytoplasmic, transmembrane and extracellular (Pereira et al., 2015). RodZ interacts with a variety of elongasome proteins (Cleverley et al., 2019), and is required for correct rod-shape formation (Alyahya et al., 2009; Muchová et al., 2013). It also regulates localisation of other elongation proteins, like MreB (Colavin et al., 2018). RodZ is also important for other cellular processes like septal placement and z-ring formation in cell division (Yoshii et al., 2019). Other membrane associated proteins, like MreC and MreD are also required for rod formation and maintenance (Levin et al., 1992). MreC and MreD act transmembrane linkers between MreB proteins and other peptidoglycan synthesis proteins (Leaver and Errington, 2005). Both proteins are essential under normal growth conditions (Kobayashi et al., 2003), and show similar phenotypes when depleted. Without adequate expression of MreC and MreD, cells will lose correct rod shape and eventually lyse, unless excess magnesium is present (Leaver and Errington, 2005). Again, MreC and MreD show similar localisation and dynamics to the rest of the elongasome (Domínguez-Escobar et al., 2011). MurJ is a flippase, which translocates the lipid II precursor from the cytoplasm over the membrane for insertion into the existing cell wall by peptidoglycan synthases (Sham et al., 2014) but does not co-localise with the elongasome (Liu et al., 2018).

Many of the elongasome proteins have been shown to co-localise and to show similar dynamics to MreB proteins. Because MreB moves in the same direction as glycan strands, and motion is driven by active peptidoglycan synthesis, I hypothesise that the distance travelled by the elongasome (processivity) determines the length of cylindrical peptidoglycan strands and subsequently plays an important role in cell shape. However, processivity has not been quantified in MreB or any other members of the elongasome. Without quantification of processivity, it is not possible to draw conclusions about how the elongasome works as a dynamic, molecular machine in order to coordinate peptidoglycan synthesis.

1.2.1 MreB is integral to cell shape

The precise function MreB has been widely studied and debated since the identification of its role in maintenance of the rod-shape of *B. subtilis* (Levin et al., 1992) and *E. coli* (Doi et al., 1988). Most rod-shaped bacteria, including *B. subtilis* and *E. coli* contain at least one *mreB* homologue, and grow by inserting nascent peptidoglycan throughout the longitudinal axis of the cell, with the exception of those that elongate from the poles (Daniel and Errington, 2003). Initial genetic studies suggested a role for MreB in dispersed growth along the cylindrical side-wall of rod-shaped bacteria (Daniel and Errington, 2003; Errington, 2015). Unlike *E. coli,* which only contains one MreB protein, *B. subtilis* contains three MreB-like proteins; MreB, MreBH and Mbl all participate in rod-shape determination (Carballido-López et al., 2006; Jones et al., 2001) and show similar localisation and dynamics to MreB (Domínguez-Escobar et al., 2011). The paralogues are partially functionally redundant as any one of the MreB proteins in *B. subtilis* can be depleted and the other two proteins allow peptidoglycan synthesis and cell shape determination (Kawai et al., 2009).

Early localisation studies (Jones et al., 2001) promoted the hypothesis that MreB has an actin-like function (Errington, 2015), providing spatial regulation of peptidoglycan synthesis machinery and directing synthases to insert nascent peptidoglycan equally along the long axis of the cell. This idea was reinforced by structural work carried out van den Ent and colleagues (Ent et al., 2001), showing MreB to have a remarkably similar tertiary structure to actin, even though genetically rather different (Bork et al., 1992; Levin et al., 1992).

Much of the structural work on MreB has been carried out on *Thermatoga maritima* MreB proteins, mainly MreB1, which is 56% identical to *B. subtilis* MreB (Shaevitz and Gitai, 2010). However, biochemically there are some notable differences. MreB can hydrolyse ATP and GTP (Mayer and Amann, 2009). This is required for polymerisation in *T.maritima* MreB *in vitro* (Ent et al., 2001). In *B. subtilis,* MreB hydrolyses the nucleotides, but this has no bearing on polymerisation (Mayer and Amann, 2009).

In a study by Salje and colleagues, membrane association of MreB was shown in multiple organisms (Salje et al., 2011) and is presumably a consistent feature in all MreB proteins. There are differences in the mechanism of membrane association. In *E. coli* this is mediated

by an N-terminal amphipathic helix, whereas in *T. maritima*, an insertion loop at L93/F94 is responsible (Salje et al., 2011). An MreB amino sequence alignment suggests *B. subtilis* to exploit the insertion loop mechanism, as the species' MreB proteins lack the cluster of hydrophobic N-terminal residues that predict the amphipathic helix in *E. coli* (Salje et al., 2011). In the study, membrane association was found essential for functionality, independent of binding mechanism (Salje et al., 2011).

1.2.2 Dynamic localisation patterns of MreB polymers

MreB localisation has been studied in depth in attempts to elucidate its precise role in cell shape control, posing various challenges to cell biologists and microscopists. Early fluorescence microscopy work found MreB forms continuous helical filaments that wrap around the circumference of the cell (**Figure 1.4(left)**) (Jones et al., 2001). This was found consistent in Mbl and MreBH in *B. subtilis* (Carballido-López et al., 2006). Many of the fluorescent fusions used N-terminal tags, and were not able to replace the native proteins (Jones et al., 2001), showing they were not fully functional This was rectified by the construction of a C-terminal tag, which did not show any defects when expressed as the sole copy (Carballido-López and Errington, 2003). The fully functional fusions also showed long helical filaments (Carballido-López and Errington, 2003). Moreover, immunofluorescence imaging also found long helical structures (Figge et al., 2004). Other elongasome proteins were found to localise in helical configurations (Leaver and Errington, 2005). These proteins were less abundant, and showed a more discontinuous form, albeit seemingly dispersed along a helical track (Errington, 2015). Also, peptidoglycan synthesis was tracked with fluorescent antibiotics, showing patterns of synthesis similar to the helical filaments supposedly formed by MreB proteins (Daniel and Errington, 2003; Tiyanont et al., 2006). These patterns were less definitive compared to the protein localisation studies. The peptidoglycan synthesis tracking did not convincingly adhere to the long filament model, however it was plausible that the peptidoglycan synthesis patterns could be compatible with long helical filaments of MreB (Errington, 2015).

Multiple studies, using a variety of techniques had provided a substantial body of evidence that MreB proteins form extended helical filaments, wrapping around the circumference of the cell. The long structures found provided a model where the filaments could guide

peptidoglycan synthesis, inserting new material at distinct tracks, evenly dispersed around the side-wall of the cell to achieve uniform longitudinal growth (Errington, 2015).

However, with progression of microscopy and fluorescent protein technologies, the long helical filament model (Jones et al., 2001) was challenged. Helical, continuous MreB structures found using an *mreB-yfp* construct (Shih et al., 2003), were found to be artefacts by subsequent electron cryotomography experiments, which found the fluorescent protein to be responsible for the structures, while deconvolution artifacts were likely the cause of the appearance of helices in other studies (Swulius et al., 2011). Cryo-electron microscopy work in *Caulobacter crescentus* found MreB filaments that are tightly membrane bound (van den Ent et al., 2014). The tight membrane association could explain the absence of any filaments in earlier electron cryotomography experiments (Errington, 2015).

Other fluorescence microscopy experiments found that MreB filaments are highly dynamic (Carballido-López and Errington, 2003; Defeu Soufo and Graumann, 2004). Later, total internal reflection (TIRF) microscopy studies analysed MreB and paralogues tagged with GFP. It was actually found that the proteins form short, discontinuous polymers that move circumferentially around the cell (**Figure 1.4.(right)**), (Domínguez-Escobar et al., 2011; Garner et al., 2011; van Teeffelen et al., 2011), further refuting the long helix model. Though the orientation of motion is predominantly at 90 ˚ to the long axis of the cell, some variation in angle is seen (Billaudeau et al., 2019; Domínguez-Escobar et al., 2011; Olshausen et al., 2013). Importantly, this processive movement of MreB was found to be dependent on peptidoglycan synthesis (Domínguez-Escobar et al., 2011; Garner et al., 2011; van Teeffelen et al., 2011).

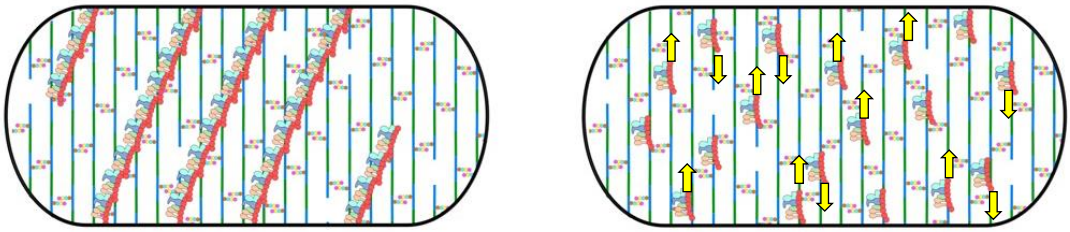

Figure 1.4. Models for MreB localisation. The long helix model (left) suggests that MreB forms continuous polymers that wrap around the cell in the form of a right-handed helix. More recently it has been established that dynamic MreB polymers move circumferentially around the cell (right), perpendicular to the long axis, represented by yellow arrows. This motion is consistent with the directionality of glycan strands in peptidoglycan.

With various studies finding MreB to form discontinuous, dynamic structures, the polymers were often described as 'patches', or 'short filaments' (Domínguez-Escobar et al., 2011; Teeffelen et al., 2011). SIM-TIRF microscopy found MreB filaments varying in length, but typically ~200 nm in length (Billaudeau et al., 2019).

It is important to consider that given the differences in peptidoglycan makeup between Gram-positives and Gram-negatives, there may be differences in the precise role and behaviour of MreB. For example, glycan strand length between *E. coli* and *B. subtilis* is apparently significantly different (Hayhurst et al., 2008; Turner et al., 2018), suggesting the processivity of the elongasome could be different between the two. Because constant elongation rate is integral in maintaining cell shape and size homeostasis (Taheri-Araghi et al., 2015), elongasome dynamics are presumably highly regulated to robustly construct a uniform cylindrical rod shaped sacculus over the whole cell cycle, at a constant rate, over multiple generations.

1.2.3 MreB filament transport

The molecular mechanism by which the MreB filament is transported around the circumference of the cell is not clearly characterised. The reversals and pauses of MreB observed (Billaudeau et al., 2017; Olshausen et al., 2013) have prompted the suggestion of a model where a molecular tug-of-war takes place on the MreB filament by molecular motors (Olshausen et al., 2013). Because MreB motion is driven by peptidoglycan synthesis,

elongasome associated peptidoglycan synthases PBP2A, PBPH and RodA are thought to be the possible drivers of the tug-of-war. In the model, it is suggested that multiple molecular motors bind and unbind to the filament but can act in either direction. The direction with the most motors acting in that direction wins and the MreB filament moves in that direction. When the filament has an equal number of motors acting in each direction, the filament is stalled and pausing of MreB is observed, until a motor binds or unbinds, tipping the balance of motors, allowing one direction to prevail.

This mode of cargo transport is prominent in eukaryotic systems. Bidirectional transport is common in eukaryotes and is reported to transport numerous cargoes such as mitochondria, pigment granules and lipid droplets (Welte, 2004). Variations of the tug-of-war mechanism of transport where molecular motors bind to the cargo and act in either a plus or minus end direction and the end with the most motors wins and transport proceeds in that direction. In a scenario where one motor can attach to each end of the filament or cargo, several possible outcomes are possible. One scenario is that each motor is bound to a different end, and the strongest motor wins, directing transport. Another, is that two motors can bind the same end, leading to transport in that direction. Another suggestion is that the motors are coordinated, and while both motors are bound to the cargo, only one is bound to the track (Welte, 2004). In the case of MreB, the track is peptidoglycan and transport of the MreB filament is driven by active synthesis.

In another recent study, SIM-TIRF was used to measure density of MreB filaments to calculate that only one peptidoglycan strand is synthesised per MreB filament and associated elongasome (Billaudeau et al., 2019). This contradicts the tug-of-war model, which states that multiple actively synthesising peptidoglycan synthases are associated to each filament (Olshausen et al., 2013). In the model proposed by Billaudeau *et al.*, collisions between filaments are thought to be the cause of reversals of MreB filaments, but super-resolution microscopy experiments observed reversals of filaments with no other filaments in proximity (Olshausen et al., 2013). Another explanation for reversals could be collisions with landmarks within the cell wall such as termini of glycan strands.

1.2.4 MreB, peptidoglycan synthesis and sacculus structure

MreB has long been established as critical for cell shape determination (Levin et al., 1992). Cell shape regulation is an intricate mechanism, with feedback between physical cell shape, peptidoglycan synthesis and elongasome proteins. MreB polymers in a processive elongasome are required for stability, directing peptidoglycan synthesis and preventing other components from diffusing throughout the membrane (Domínguez-Escobar et al., 2011). Recent work describes how MreB polymers work as a cell thinning mechanism, acting as an inward force on peptidoglycan synthesis. This is said to oppose the cell widening mechanism of extracellular PBPs such as PBP1 in *B. subtilis* (Dion et al., 2019).

Various non-lethal *mreB* point mutations have been identified to alter cell shape in *E. coli*. The alanine at the 53rd residue of MreB can be replaced with either glycine, leucine, threonine or lysine resulting in varied cell diameter (Monds et al., 2014). Other point mutations such as M272L and K27E make cells thinner and wider, respectively, while E143A introduces large variability in single-cell diameter in a population (Shi et al., 2018). Other point mutants such as D78V, E143A and D83Y also perturb *E. coli*'s innate morphology (Shi et al., 2018). All of these residues are conserved in *B. subtilis* when amino sequences are aligned, however it is unclear whether the same mutations have the same effect on morphology. Early characterisation work in *B. subtilis* revealed the point mutations L296S and M104R to increase cell diameter (Jones et al., 2001).

The presence of MreB paralogues adds complexity to the *B. subtilis* system. MreB and Mbl are essential under normal growth conditions, whereas MreBH isn't (Kobayashi et al., 2003). However, depletion of *ponA*, *ptsI*, *ccpA* (Kawai et al., 2009) or overexpression of GlmR (Foulquier et al., 2011) can restore viability, as can excessive levels of magnesium (Formstone and Errington, 2005). The three paralogues show partial functional redundancy. MreB and Mbl are required for peptidoglycan synthesis and correct shape. Interestingly, any loss of peptidoglycan synthesis or correct shape can be overcome with overexpression of any of the three paralogues, but at least two of the three isoforms are required to sustain functionality of the rod-complex (Kawai et al., 2009). This is in contrast to *E. coli*, which contains a singular *mreB gene*. In *B. subtilis*, the paralogues have been found to form a co-filament (Dersch et al., 2020).

MreB moves processively in the same direction of glycan strands in peptidoglycan, and is peptidoglycan synthesis dependent (Errington, 2015; Garner et al., 2011; Typas et al., 2012) but the orientation and dynamics of MreB are also dependent on cell shape (Hussain et al., 2018; Ouzounov et al., 2016; Reimold et al., 2013), showing a feedback from the cytoskeleton to the sacculus.

MreB dynamics can adapt to cell-shape irregularities, in order to maintain homeostasis of correct rod-shape. For example, in *E. coli,* the orientation of MreB filaments change with local aberrations in cell diameter to maintain constant diameter over multiple generations (Ouzounov et al., 2016), even though MreB motion is mostly perpendicular to the long axis of the cell (Domínguez-Escobar et al., 2011; Garner et al., 2011). More recent work has found diameter homeostasis to be controlled by the dynamic elongasome, synthesises cylindrical peptidoglycan, resulting in thinner cells in conjunction with aPBPs such as PBP1, which has the opposing effect (Dion et al., 2019). Locally, MreB targets areas of the membrane with a negative curvature, to act as a corrective mechanism, directing peptidoglycan synthases to areas of the cell wall with an irregular form (Dion et al., 2019; Hussain et al., 2018). In addition, arrest of peptidoglycan synthesis has been shown in multiple studies to halt MreB dynamics (Domínguez-Escobar et al., 2011; Garner et al., 2011; Hussain et al., 2018). Ultimately, dynamics of MreB, respond to changes in sacculus structure and peptidoglycan synthesis and feedback locally or at a cellular level by redirecting peptidoglycan synthesis (Errington, 2015).

The complexity of the relationship between cell shape, MreB dynamics and peptidoglycan synthesis pose further questions about how cell wall architecture is regulated to maintain shape and size homeostasis of a population over multiple generations. Perturbations of MreB, peptidoglycan synthesis and cell shape reveal much about the interplay between the systems, but the mechanistic understanding of how MreB and the rest of the elongasome work in conjunction as a molecular machine in order to coordinate cell shape is not determined. For example, how are MreB dynamics regulated (Errington, 2015)? How is this regulation coupled to peptidoglycan synthesis and subsequent architecture? Moreover, how processive is the elongasome and how does this affect subsequent peptidoglycan structure? Some have suggested that glycan strands provide a track or template that guides the elongasome (Höltje, 1998). However, this model does not explain the ability of MreB dynamics to respond to

irregular cell shape (Errington, 2015), nor the ability of cells to build a cell wall from scratch as the revert from L-form (peptidoglycan deficient) state (Kawai et al., 2014).

1.2.5 Advantages and limitations of currently used methods to observe MreB dynamics

Since the early localisation studies of MreB, improvements and development of light microscopy techniques has facilitated the progression of our understanding of the role of MreB and the elongasome in peptidoglycan synthesis and cell shape.

Total internal reflection (TIRF) microscopy has been widely used to observe MreB dynamics and at the time of this study is the current gold standard. TIRF microscopy only illuminates ~100 nm above the cover slip and into the cell, therefore, removes noise from the rest of the cell and the slide improving the SNR. This also is an inherent limitation of the method. Because only a subsection of the cell is illuminated, MreB moves out of the illumination plane, truncating trajectories and limiting the time it is possible to observe dynamics.

Single-molecule (SM) microscopy has also been used to improve resolution while tracking protein dynamics. By only labelling single molecules in a cell, dynamics can be tracked in detail as there is no need to resolve subunits from each other. This has been combined with TIRF to provide the best resolution and signal to noise ratio (SNR) (Dersch et al., 2020; Hussain et al., 2018).

Vertical cell imaging by nanostructured immobilization (VerCINI) is a novel method developed to observe protein organisation around the circumference of the cell (Bisson-Filho et al., 2017; Whitley et al., 2022). In the method, an agarose pad is produced from a silicon mould with microholes of around 1 μm in diameter. Cultures are then centrifuged into the holes allowing imaging down the long axis of love cells. This removes the limitations of the field of illumination of TIRF and increases resolution of widefield microscopy as resolution of circumferential proteins can be done in the XY plane rather than Z. This approach will allow observation of MreB around the whole circumference of the cell, improving the time it is possible to observe trajectories.

Lastly, the development of JF (Jenelia Fluor) dyes greatly reduce the other limiting factor when attempting to observe protein dynamics for lengthy time periods. Traditional dyes are bright

and photostable but lack cell permeability so are usually used to label fixed cells. Net neutral dyes have typically been used to label live cells; however, they lack the brightness and photostability of traditional dyes and are prone to photobleaching, which limits the length of time the dyes are observable. JF dyes have been developed with the incorporation of four-membered azetidine rings into classic fluorophore structures (Grimm et al., 2015). This resulted in bright, photostable dyes that are cell permeable, allowing tracking of the fluorophores for long time periods in live cells. Moreover, the use of a dye, rather than a fluorescent fusion protein allows single-molecule labelling without the need for a pre-photobleaching step, which could have a negative impact on the observable lifetime of the fluorophore.

1.3 Research aims

The aim of the study is to develop and optimise SM-VerCINI in order to track MreB subunits for longer time periods than previously possible. This will allow quantification of MreB processivity, which should shed light on how the elongasome moves over time to construct cylindrical peptidoglycan and maintain cell diameter homeostasis. In addition, the ability to track MreB for longer should allow quantification of events such as reversals and pauses, which should provide insight into the mechanism of how the MreB filament is transported by the elongasome. Once optimised, it will be used to observe how various perturbations of cell growth and elongasome associated peptidoglycan synthesis affect MreB dynamics to elucidate how dynamics are regulated to form a uniform rod-shaped peptidoglycan sacculus and optimal elongation.

Chapter 2: Materials and Methods

2.1 General Microbiology and Strain Construction

2.1.1 General practices

Incubations and inoculations were carried out in temperature-controlled rooms with orbital shaking at 175 rpm. Bacterial strains were streaked and inoculated using sterilised toothpicks. Cultures were pelleted by centrifugation of 1.5 ml of cultures in 1.5 ml Eppendorf tubes for 1 minute at 16900 RCF.

2.1.2 Growth Media

All media were sterilised by either autoclave or filter sterilisation with 0.2 µm filters and stored at room temperature except for 100 X Metal Mix, which was stored at 4˚C.

Table 2.1.1. Composition of media and supplements used in this work. All % units are weight to volume.

Medium/ Supplement	Composition/ Concentration/ Vendor
Luria Bertani (LB)	10 g/l Tryptone (Oxoid) 5 g/l Yeast Extract (Oxoid) 10 g/l NaCl (VWR)
Nutrient Agar (NA) Plates	1 X from dehydrated (Fisher)
Spizizen Minimal Media (SMM) Salts (1 X)	0.2 % Ammonium sulphate (VWR) 1.4 % di-Potassium hydrogen phosphate (VWR) 0.6 % Potassium dihydrogen phosphate (VWR) 0.1 % Sodium citrate dihydrate (VWR)
SMM	1 X SMM Salts (Above) 0.5 % D-Glucose (VWR) 2 µg/ml L-Tryptophan (FORMEDIUM) 6 mM Magnesium sulphate heptahydrate (VWR) 16.8 µM Ammonium Iron(III) citrate (Aldrich)

	5 µl Casamino Acids (BD)
Starvation Media	1 X SMM Salts (Above) 0.5 % D-Glucose (VWR) 6 mM Magnesium sulphate heptahydrate (VWR)
Metal Mix (100 X)	2 mM Hydrochloric Acid (HCl) (Honeywell) 190 mM Magnesium Chloride Hexahydrate (Sigma) 65.9 mM Calcium Chloride Dihydrate (Sigma 4.84 mM Manganese Chloride Tetrahydrate (Fisher) 0.106 mM Zinc Chloride (Sigma) 0.196 mM Thiamine Chloride (Sigma) 0.470 mM Iron (III) Chloride Hexahydrate (VWR)
S750 Salts (10 X)	500 mM MOPS (Sigma) 100 mM Ammonium Sulphate (Sigma) Potassium Phosphate Monobasic (VWR) pH adjusted to 7.0 with Potassium Hydroxide (VWR)
S750 Media	1 X S750 salts (Above) 1 X Metal mix (Above) 1 % Carbon source (Glucose or Maltose (VWR)) 10 mM L-Glutamate (Sigma)
Isopropyl ß-D-1-thiogalactopyranoside (IPTG)	Concentration stated where applicable
Erythromycin	1 µg/ml
Lincomycin	25 µg/ml
Kanamycin	5 µg/ml

2.2 *B. subtilis* strains and strain construction

2.2.1 *B. subtilis* transformation and strain confirmation

A single colony of the recipient strain was used to inoculate 2 ml SMM overnight at 37˚C. The following morning, 300 µl of the overnight culture was used diluted in 5 ml SMM and incubated for 3 hours at 37˚C. 5 ml pre-warmed starvation media was added to the cultures which were incubated for a further 3 hours. gDNA was added to 300 µl of culture and incubated for 1 hour at 37˚C. Cultures were then spread onto NA plates containing relevant antibiotic and necessary supplement using glass beads. Plates were incubated overnight at 37˚C. Cultures with no added gDNA were also spread onto NA plates for the purpose of a negative control.

The following morning, a number transformant colonies were re-streaked onto NA plates containing relevant antibiotic and necessary supplement and incubated overnight at 37˚C. This was repeated twice. gDNA was then extracted from transformant strains and PCR carried out to confirm the transformation.

Once confirmed by PCR, a single colony was used to inoculate 2 ml LB with relevant antibiotic and necessary supplement at 37˚C. The following morning, the culture was mixed 1:1 with 50% glycerol (25% final concentration) and stored at -80˚C.

Table 2.2.1. Strain number, genotype and construction details of all strains used in this work.

Strain	Species and Strain	Relevant Genotype	Construction
bYS40	*B. subtilis PY79*	*mreB::mreB-HaloTag*	Published strain (Hussain et al., 2018). Provided by Ethan Garner Lab.
-	*B. subtilis 168*	*trpC2 Δhag::erm^R*	BKE library (Koo et al., 2017).
SM01	*B. subtilis PY79*	*mreB::mreB-HaloTag Δhag::erm^R*	bYS40 transformed with *Δhag::*erm gDNA.

-	*B. subtilis 168*	*trpC2 ΔpbpA::kan^R*	BKK library (Koo et al., 2017).
SM22	*B. subtilis PY79*	*mreB::mreB-HaloTag Δhag::erm^R ΔpbpA::kan^R*	SM01 transformed with *ΔpbpA::kan* gDNA.
-	*B. subtilis 168*	*trpC2 ΔpbpH::kan^R*	BKK library (Koo et al., 2017).
SM23	*B. subtilis PY79*	*mreB::mreB-HaloTag Δhag::ermR ΔpbpH::kan^R*	SM01 transformed with *ΔpbpH::kan* gDNA.
YK2245	*B. subtilis 168CA*	*trpC2 rodA::kan^R-P$_{spac}$-rodA*	Published strain (Emami et al., 2017). Provided by Richard Daniel Lab.
SM28	*B. subtilis PY79*	*mreB::mreB-HaloTag Δhag::erm^R rodA::kan^R-P$_{spac}$-rodA*	SM01 transformed with YK2245 gDNA.
-	*B. subtilis 168*	*trpC2 ΔmltG:kan^R*	BKK library (Koo et al., 2017).
SM41	*B. subtilis PY79*	*mreB::mreB-HaloTag Δhag::erm^R ΔmltG:kan^R*	SM01 transformed with *ΔmltG::kan* gDNA.
HS553	*B. subtilis 168*	*trpC2 mreB::mreB-msfGFP-mreB*	Gifted by Henrik Strahl.
SM26	*B. subtilis 168*	*trpC2 mreB::mreB-msfGFP-mreB ΔpbpA::kan*	HS553 transformed with *ΔpbpA::kan* gDNA.
SM27	*B. subtilis 168*	*trpC2 mreB::mreB-msfGFP-mreB ΔpbpH::kan*	HS553 transformed with *ΔpbpH::kan* gDNA.

2.2.2 Genomic DNA Extraction

Genomic DNA (gDNA) was extracted using an adapted version of the Promega Wizard extraction protocol. A single colony was inoculated overnight at 30˚C in 5 ml LB supplemented with 1 % glucose. The next morning, cultures were pelleted and resuspended in 100 µl EDTA, lysozyme and RNase A and incubated at 37˚C for 1 hour. 500 µl Nuclei Lysis buffer was added before incubation at 80˚C for 5 minutes. The sample was allowed to cool to room temperature, then 200 µl Protein Precipitate solution was added. The sample was thoroughly vortexed then incubated on ice for 10 minutes before centrifugation at 16900 RCF for 10 minutes. The supernatant was removed and added to 600 µl isopropanol and mixed by inversion of the Eppendorf tube until visible precipitation of the DNA. The DNA was pelleted by centrifugation for 10 minutes at 16900 RCF The supernatant was removed, and the DNA pellet washed twice with 600 µl ethanol, with centrifugation for 5 minutes at 16900 RCF. The ethanol was removed, and the DNA pellet was allowed to air-dry before being resuspended in 100 µl elution buffer and incubated at 65˚C with vortexing after 2.5 minutes. DNA concentration was measured, and quality assessed using a Nanodrop spectrophotometer. DNA was stored at -20˚C.

Table 2.2.2. Composition and concentrations of buffers and solutions used in the extraction of gDNA from *B. subtilis.*

Buffer/ Solution	**Concentration/ Vendor**
Ethylenediaminetetraacetic acid (EDTA)	50 mM (Sigma)
Lysozyme	300 µg/ml (Sigma)
RNase A	300 µg/ml (Sigma)
Nuclei Lysis Buffer	1 X (Promega)
Protein Precipitate solution	1 X (Promega)
Isopropanol	100 %

Ethanol	70 %
Elution Buffer	100 % (Monarch, NEB)

2.2.3 Polymerase chain reaction and agarose gel electrophoresis

All PCR experiments were first simulated using Snapgene cloning software to determine annealing temperature of oligonucleotides and expected product size before *in vitro* experiments were carried out.

PCR was carried out using Q5 High-Fidelity DNA polymerase using the protocol suggested by NEB. 50 µl reactions were prepared (**Table 2.2.3**) and carried out in a thermal cycler (**Table 2.2.4**). gDNA was used as the template DNA and deoxynucleotide triphosphates were acquired from Promega and stock solutions prepared with a 1:1:1:1 ratio. PCR experiments were carried out by designing oligonucleotides to flank the genetic region of interest so any insertion or deletion of a gene would still produce a PCR product. The product would then be comparable to the recipient strain and donor strain which were used as negative and positive controls respectively.

Table 2.2.3. PCR setup in accordance with protocol provided with Q5 High-Fidelity DNA polymerase.

Component	**Final concentration**
Q5 Reaction Buffer	1 X
dNTPs	200 µM
Forward Oligonucleotide	0.5 µM
Reverse oligonucleotide	0.5 µM
Template DNA	100-200 ng
Q5 High-Fidelity DNA Polymerase	0.02 U/µl

Table 2.2.4. PCR thermal cycler conditions in accordance with protocol provided with Q5 High-Fidelity DNA polymerase. Extension and final extension times are quoted in seconds per kb of expected product. Steps 'Denaturation' through 'Extension' were repeated for 25 cycles.

Step	Temperature (˚C)	Time (s)
Initial Denaturation	98	30
Denaturation	98	10
Annealing	Oligonucleotide dependent (~60)	10
Extension	72	30/kb
Final Extension	72	30/kb
Store	8	-

All oligonucleotides (**Table 2.2.5**) were purchased from Integrated DNA Technologies (IDT) and stored at -20˚C.

Table 2.2.5. Number, sequence and purpose of all oligonucleotides used in this work

Number	Sequence (5'-3')	Purpose
oSM01	CTGCCTGCAACAAAAGTGGTG	Confirm introduction of *Δhag::erm*^{R} into chromosome.
oSM02	GATGTGATCTCCGCATTATCCTCAC	
oSM19	CTGAATTCCCCCTGCGTATAATG	Confirm introduction of *ΔpbpA::kan*^{R} into chromosome.
oSM20	GAAGGGGAAAATGAAACCATGGAAGAAG	
oSM27	CAAAGGTGTTACAATTAATCTCAGTATATG	Confirm introduction of *ΔpbpH::kan*^{R} into chromosome.
oSM28	GTTTAACATGCTGCGTATCCTGTTC	
oSM78	GAATCCGGTCATCAAGCTGAAATTC	Confirm introduction of *ΔmltG::kan*^{R} into chromosome.
oSM79	GTGAGCTATTCCCGATTGAAACTGAC	
oSM16	GTCATATTTCGTGTAGCTGAAAAAG	Confirm introduction of *rodA::kan*^{R}-P_{spac}-*rodA* into chromosome.
oSM43	GTTGCGTAAAAGAAGAAGAATACCCAC	

For agarose gel electrophoresis, a 1.2 % agarose (Melford) gel in TAE (Formedium) was prepared and supplemented with 2.5 % Nancy-520 (Sigma). Samples were mixed with gel loading dye (NEB) and loaded into the gel alongside a 1 kb ladder (NEB). The gel was run at 100 V until adequate migration of the samples. Visualisation of samples was carried out using a Syngene LED Blue Light Transilluminator (Fisher).

2.2.4 Growth rate measurements

A single colony was used to inoculate 2 ml media with necessary supplement and incubated overnight at 37˚C. The following morning, cultures were diluted to an OD_{600} of 0.05-0.1 in 200 µl in a 96-well plate. This was performed in triplicate for each strain and condition, with media only as the blank as a negative control. Growth curves were performed at 30˚C in a

SPECTROstar Nano spectrophotometer (BMG Labtech). OD_{600} was measured every 5 minutes, with shaking at 200 rpm.

2.3 Microscopy

2.3.1 Cell cultivation for all microscopy experiments

To ensure cells were in exponential growth for imaging experiments, 5 ml media was inoculated with a single colony. From this culture, a further two cultures were set up by serial, 10-fold dilution, decreasing the mass of inoculum. The cultures were incubated overnight at 37˚C. This ensured that the following morning, at least one culture in exponential growth was available. Typically, the culture inoculated with a colony had reached stationary phase and it was possible to compare visually the lower optical density of the diluted cultures to infer exponential phase. The following morning, cultures were diluted to an OD_{600} of 0.05-0.1 in 5 ml media and incubated at 30˚C. Cultures were grown to an OD_{600} of 0.6 ± 0.1, ensuring multiple cell cycles had taken place and the cultures were growing exponentially.

2.3.2 Materials

All microscopy was performed using the same materials (**Table 2.3.1**) unless otherwise stated.

Table 2.3.1. Materials for sample preparation and microscopy.

Material	Relevant specifications/ Vendor
Microscope Slide	Super premium (VWR)
Cover Slip (General)	Square, 22mm, Thickness no. 1.5 (VWR)
GeneFrame	65 µl, 1.5 x 1.6 cm (Fisher)
UltraPure Agarose	(VWR)
Immersion Oil	Type F (Olympus)
Precision Cover Slip	High Precision, 22 x 22 mm, Thickness no. 1.5 (ThorLabs)
Silicone Gasket	9 mm (Sigma)

2.4 VerCINI: Sample preparation and microscopy

VerCINI experiments described below were carried out as published (Whitley et al., 2022). All sample preparation was carried out in a 30˚C temperature-controlled room, except for widefield microscopy experiments. Slides were transported to the microscope room in a pre-warmed pipette tip box.

2.4.1 Single-Molecule labelling of MreB-HaloTag with JF549 for SM-VerCINI

JF549 (Grimm et al., 2015) was used to fluorescently label MreB-HaloTag. JF549 was purchased from Promega and stored at -80˚C. 5 nM stock solutions were prepared in Dimethyl sulfoxide (DMSO) and stored at -80˚C. Upon cultures reaching adequate OD_{600}, 2.5 µl JF549 stock was added to 500 µl culture in a 1.5 ml Eppendorf tube, to a final concentration of 25 pM and incubated at 30˚C for 10 ± 2 minutes. During dye concentration optimisation, stock JF549 solutions were prepared to ensure no more than 1 % DMSO was added to cultures.

2.4.2 Sample preparation

To prepare a VerCINI agarose pad **(Figure 2.1)**, 800 µl 6 % molten UltraPure agarose was spotted onto a micropillar wafer (pillar width = 1.2 µm, pillar height = 4.4 µm) using a wide bore pipette. A microscope slide, with GeneFrame applied was pressed GeneFrame facing downwards onto the agarose covered wafer, centring the GeneFrame around the micropillars. The agarose was allowed to set and was pre-warmed at 30˚C.

After dye incubation, cultures were washed twice in 500 µl pre-warmed media with centrifugation at 16900 RCF for 1 minute. During the final wash, the microscope slide with agarose was peeled from the micropillar wafer revealing open topped microhole array. A silicone gasket was applied atop the pad around the microhole array. After the final wash, the pellet was resuspended in 8 µl pre-warmed media and spotted onto the microhole array inside the silicone gasket. The slide was taped onto a flat-bottomed centrifuge rotor and centrifuged at 3220 RCF for 4 minutes. If no dye stage was necessary, 500 µl of culture was concentrated to 8 µl and spotted onto the pad **(Figure 2.1)**.

After centrifugation, to remove excess horizontal cells, slides were washed by slowly pipetting ~3 ml pre-warmed media over the pad until excess cells were visibly removed (de Jong et al.,

2011). Agarose outside of the microhole array was removed with a scalpel and the pad was allowed to air dry before application of the cover slip (**Figure 2.1**). Cells were allowed to acclimatise at imaging temperature for at least 10 minutes before any data were acquired.

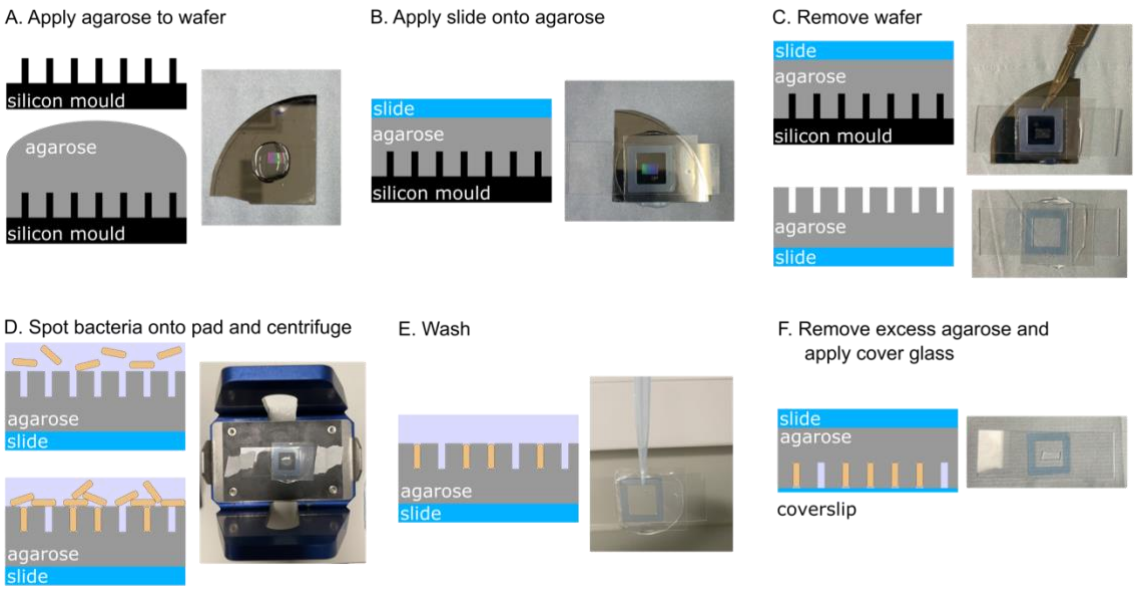

Figure 2.1. Cartoon representation and photographs of VerCINI sample preparation. Figure from (Whitley et al., 2022).

2.4.3 Microscopy

VerCINI was carried out on a custom-built microscope. The slide was applied atop a 100x TIRF objective (Nikon CFI Apochromat TIRF 100XC Oil) with immersion oil. Samples were illuminated with either a 488 nm (Obis) or a 561 nm (Obis) laser, depending on the fluorophore. Cells were typically illuminated at a power density of 16.9 W/cm^2 for 500 ms with a 6 s strobe interval for a total of 8 minutes unless otherwise stated. HILO (Tokunaga et al., 2008) illumination was employed, where galvanometer-driven mirrors (Thorlabs) rotating at 200 Hz to achieve high SNR and a uniform illumination field **(Figure 2.2)**. Images were acquired using a 200 mm tube lens (Thorlabs TTL200) and Prime BSI sCMOS camera (Teledyne Photometrics) with a pixel size of 65 nm in sCMOS mode. The microscope was operated using open-source software, µManager (Edelstein et al., 2014).

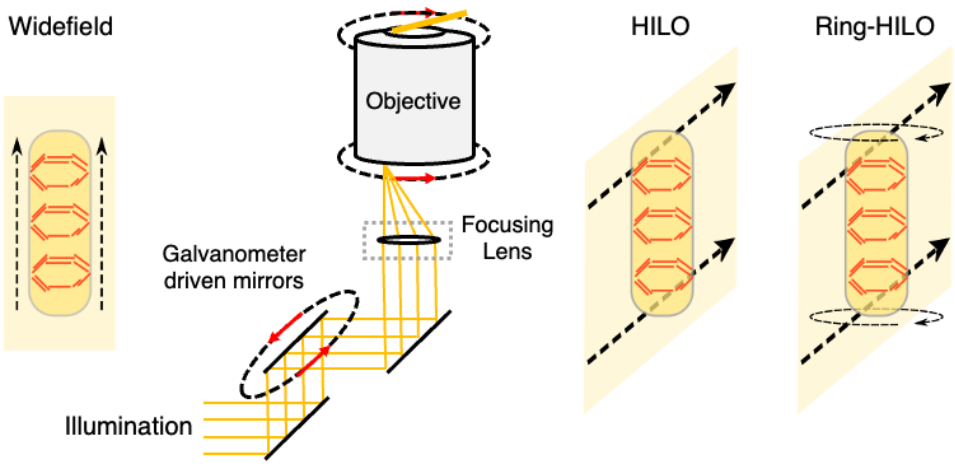

Figure 2.2. Cartoon representation of microscope setup and comparison of illumination field between widefield, HILO and ring-HILO.

2.5 VerCINI: Image analysis

Image analysis was carried out using custom, open-source software and published plugins available at: https://github.com/HoldenLab . Image denoising and ring fitting (2.5.1-2.5.2) was carried out as published (Whitley et al., 2022). Custom code in these sections were written by Séamus Holden. I wrote all custom code in the kymograph analysis stages (2.5.3), which is available open source on the HoldenLab GitHub page.

2.5.1 Image denoising and registration

Image denoising and registration was carried out in FIJI (Schindelin et al., 2012). Images were denoised using the PureDenoise plugin (Luisier et al., 2010) and registered to correct for lateral drift using the StackReg plugin (Thévenaz et al., 1998).

2.5.2 Ring fitting and kymograph extraction

Individual cells were manually selected and cropped using a custom FIJI plugin. Using custom Matlab code written by Séamus Holden, a ring was fitted around the circumference of each vertical cell and the signal around the ring for the duration of the time-lapse was plotted as a kymograph. Time, typically 8 minutes, was plotted on the y-axis of the kymograph, against signal around 0˚- 2160˚ of cell circumference on the x-axis. The x-axis was plotted multiple times around the cell circumference to ensure that the longest trajectories could be fully observed.

2.5.3 SM-VerCINI: Manual kymograph tracing and trajectory analysis

In FIJI, a segmented line was used to trace over trajectories. An ROI set was saved for each kymograph. Only clear trajectories were traced. If tracks crossed over each other, they were only counted if they were clearly distinguishable from each other. Also, if tracks appeared to move in or out of focus they were discounted.

Table 2.5.1. Workflow for analysis of SM-VerCINI data.

Analysis Step	Process	Outcome	Reference
Step 1	Code written by Séamus Holden, with implementation of published software (Whitley et al., 2021).		
Cell selection	Using a custom FIJI plugin, cells are manually selected, and region of interest is drawn around each cell.	Individual cells are isolated, and any cells obstructed by horizontal cells on top of the pad are discarded.	(Whitley et al., 2021)
Denoising	Reduces background noise from the image.	Improved signal to noise ratio making tracks easier to identify.	(Luisier et al., 2010)
Registration	Aligns each slice of the time lapse, using the last slice as a reference point.	Removes any spatial drift from time lapses ensuring drift in images aren't misinterpreted as motion of molecules.	(Thévenaz et al., 1998)
Step 2	Code written by Séamus Holden (Whitley et al., 2021).		
Ring Fitting	Cell circumference is identified to sub-pixel localisation using a custom model.	Cell circumference is identified and plotted, providing a line from which a kymograph can be plotted.	(Whitley et al., 2021)
Kymograph Plotting	The background is subtracted from each image, and a kymograph calculated along the circular line profile of the cell circumference.	A kymograph is plotted, allowing analysis of trajectories.	
Step 3	Code written by me in this study.		
Manual Trajectory Tracing	In FIJI, a segmented line was traced over trajectories on each	Trajectories identified and saved for analysis.	This Study

	kymograph and saved as an ROI set for each kymograph.		
Exporting of Coordinates	Custom FIJI plugin exports coordinates of each point of each trajectory to a .csv file.	Provides numerical data to analyse trajectories.	
Trajectory Analysis	Custom python code written in a jupyter notebook by me. The code uses the coordinates of segmented lines traced on trajectories on kymographs to analyse dynamics. The code analyses lifetime, speed and processivity of both total tracks and subtracks. In addition, time spent in different states and switching rates between states were measured. The code exports a .csv file of the data for each biological replicate, which is then used to plot and compare data.	In-depth analysis of single molecule trajectories. Various measurements quantified as described in Table **2.5.2**.	

A custom FIJI plugin was written export the XY coordinates of the tracks to a .csv which was imported into python for trajectory analysis. Using the coordinates of the trajectories, custom code was written to determine a plethora of measurements to describe SM trajectories (**Table 2.5.1**).

Table 2.5.2. Definitions and descriptions of terms used to describe single molecule trajectories analysed in custom python code in this work.

Term	Definition/ Description
Total Track	A whole observed trajectory.
Subtrack	A section of a total track with a constant speed and directionality.
Lifetime	The time that a track is observed. Measured as Δy on a kymograph.
Processive	A subtrack displaying motion around the cell circumference. A subtrack was deemed processive if it travelled >0.195 µm. Measured by Δx on a kymograph.
Paused/Static	A subtrack displaying no motion around the cell circumference. A subtrack was deemed paused/static if it travelled ≤0.195 µm. Measured by Δx on a kymograph.
Displacement	Distance travelled around the cell circumference. Measured by Δx on a kymograph..
Processivity	Displacement of a subtrack. Measured by Δx on a kymograph.
Reversal	An event where a processive subtrack changes direction to begin another processive subtrack in the opposing direction.
Initiation	An event where a paused subtrack begins motion.
Nucleation	An event where the track is observed to appear within the duration of the time-lapse
Existing track	A track that is observed from the outset of the time-lapse
Pause	An event where a processive subtrack ceases motion to begin a paused/ static subtrack.

Unbinding	Loss of signal from a total track. This infers either the molecule unbinding from the cell membrane, or photobleaching of the fluorophore.
Switching Rate	Number of each transition type from immobile or processive states, divided by the total duration of all immobile or processive states observed in the dataset (Özbaykal et al., 2020)

2.6 TIRF Microscopy

2.6.1 Sample preparation

A 1.2 % UltraPure agarose pad in media was prepared in a GeneFrame as published (de Jong et al., 2011). 300 µl molten agarose was pipetted into a GeneFrame on a microscope slide and another microscope slide applied atop. After the agarose was allowed to set, the microscope slide was removed, and a 5 mm wide strip was cut in the centre of the pad and the rest of the agarose removed. 1 µl of culture was spotted directly onto the pad and allowed to air dry before application of the cover slip. When necessary, samples were labelled with JF549 and resuspended to the initial OD_{600} of the culture and spotted onto the pad before application of the cover slip.

2.6.2 Microscopy

TIRF-microscopy was carried out the custom-built microscope as described above. Ring-TIRF was achieved by altering the radius of the galvanometer-driven mirrors used for HILO illumination. Illumination was achieved with 488 nm and 561 nm lasers at a power density of 16.9 W/cm^2 for dependent on the fluorophore. Samples were illuminated for a 500 ms exposure with a 2 s exposure time for a total of 40 s.

2.6.3 MreB speed quantification

As with VerCINI data, images were denoised and registered using PureDenoise (Luisier et al., 2010) and StackReg (Thévenaz et al., 1998) respectively. In FIJI, a straight line ROI was drawn over MreB filaments **(Figure 2.3.A)** in the direction of motion and an ROI set saved for every field of view. Using the FIJI plugin KymographBuilder (Mary et al., 2016).

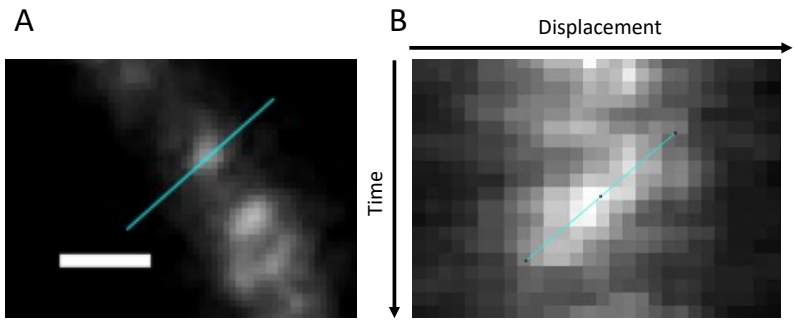

Figure 2.3. Example of TIRF MreB speed analysis steps. **A.** The first frame from a time-lapse of MreB in horizontal cells with a straight line ROI drawn over the MreB filament. Scale bar = 1 µm. **B.** Resulting kymograph showing displacement of the filament against time with a straight line ROI drawn over the track which was subsequently used to determine speed of the filament.

An ROI was traced over the kymograph tracks **(Figure 2.3.B)** and measured using the built-in measure function in FIJI. Results were exported to MS Excel and speeds calculated from the gradient of the track.

2.7 SIM-TIRF Microscopy

2.7.1 Sample prep

Cultures were cultured and labelled with JF549 as described above (2.4.1) however, 500 nM JF549 was used to achieve full labelling of MreB-HaloTag. After labelling, cultures were washed 3 times with pre-warmed media and spotted onto a 1.2% UltraPure agarose pad prepared with media in a GeneFrame (de Jong et al., 2011). The sample was allowed to airdry before application of a precision cover slip. Precision cover slips were plasma cleaned for 15 minutes as described prior to application.

2.7.2 Microscopy

SIM-TIRF microscopy was carried out on a Nikon N-SIM/N- STORM inverted fluorescence microscope with a TIRF-561 grating block. Samples were illuminated for 50 ms with a power density of 11.9 W/cm^2 with a strobe interval of 1 s for a total of 60 s. Reconstruction of the images was performed within NIS elements software using default settings. Brightfield images were also taken for each field of view.

2.7.3 Processive track quantification

Analysis of processive MreB tracks was carried out using the FIJI plugin, TrackMate (Tinevez et al., 2017) similarly to previously published (Dion et al., 2019). A Linear Motion LAP tracker was used with a threshold for spot size of 200 nm and a quality threshold of 20 counts. Only spots with an intensity of ≥ 300 were counted, with a 200 nm linking and gap distance and 1 frame gap linking. Tracks were deemed processive if they had a displacement of ≥ 250 nm and ≥ 6 spots.

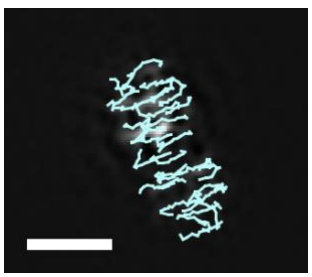

Figure 2.4. Example of MreB tracks detected using TrackMate. Scale bar = 1 µm.

2.7.4 Measurement of cell area from brightfield images

Ilastik (Berg et al., 2019) machine learning segmentation was employed to measure cell area from brightfield images. All the brightfield images used taken in the SIM-TIRF experiments were used to train Ilastik by colouring the cells yellow and the background blue **(Figure 2.5.A)**. The more data that were coloured, the more accurate and precise the software became at measuring cell area. Once trained, the software was run to identify cells against background **(Figure 2.5.B)**. Data were imported into FIJI to measure total cell area in each FOV. The FIJI threshold function was used and set to 'Auto'. This separated the cells from the background by intensity. The measure function was then used to measure the area of the cells in pixels, which was then converted to μm^2 in MS Excel.

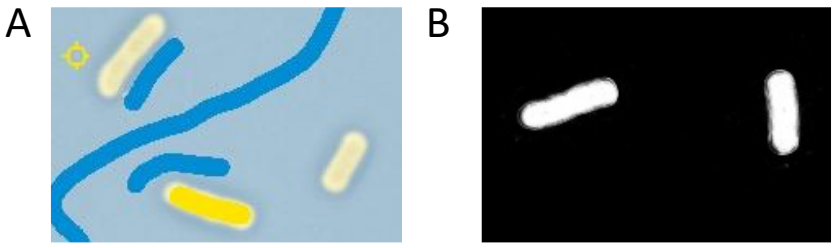

Figure 2.5. Example of morphology measurements from brightfield images using Ilastik. **A.** The software was trained by colouring in cells in yellow and the background in blue. **B.** Once trained, the software produced probabilities to determine cells (white) against background (black).

2.8 Widefield Microscopy for Cell Morphology Measurements

2.8.1 Membrane staining and sample preparation

500 µl culture was incubated for 5 minutes with 1 µg/ml Nile Red (Sigma) in DMSO at growth temperature in a 2 ml Eppendorf with a pierced lid for oxygenation. 1 µl stained culture was spotted onto a 1.2 % UltraPure agarose pad in dH_2O in a GeneFrame and allowed to airdry before application of the cover slip.

2.8.2 Microscopy

Imaging of membrane-stained cells was carried out by widefield microscopy on a Nikon Ti microscope with a Sutter Instrument Lambda LS Xenon-arc light source and a Nikon Plan Fluor 100×/1.30 NA Oil Ph3 objective. Using Metamorph 7.7 software. Samples were illuminated with 560 nm light for 100 ms and images acquired using a Photometrics CoolSNAP HQ2 camera.

2.8.3 Morphology measurements

To measure cell width, a straight line ROI was drawn over the short axis of the cell in FIJI and an intensity profile plotted. The intensity plots were exported to Matlab where the centre of each peak and the distance between them were determined as published (Whitley et al., 2021).To measure cell length, a straight line ROI was drawn from the pole to pole, or pole to septum and the length measured in FIJI.

2.9 Statistics

With the exception of *ΔpbpH* in SM-VerCINI experiments, and both TPase knockouts in TIRF MreB speed experiments, all experiments were carried out with at least 2 biological replicates, which are experiments on separate cultures that originated from a different single-colony on an NA plate. Overall medians and medians of biological replicates are plotted in all figures.

With the exception of single molecule switching rates, all values quoted are medians with 95% confidence intervals calculated by bootstrap resampling (Efron, 1979), while all differences stated are median difference (Cumming and Calin-Jageman, 2016) calculated using the published DABEST (Data Analysis with Bootstrap-coupled ESTimation) software (Ho et al., 2019) with 95% confidence intervals also calculated by bootstrap resampling (Efron, 1979). Confidence intervals on switching rates were calculated via bootstrapping using custom code written by Séamus Holden. Confidence intervals on differences between switching rates were calculated by error propagation using custom code written by Séamus Holden.

Chapter 3: Single-Molecule VerCINI reveals a highly processive elongasome with frequent state switching

3.1 Introduction

Since it was determined that MreB filaments are dynamic, moving around the circumference of the cell (Domínguez-Escobar et al., 2011; Garner et al., 2011; van Teeffelen et al., 2011), a variety of light microscopy techniques have been utilised in recent years to further the understanding of how MreB dynamics relate to cell wall construction and cell shape. One of the key findings in the early studies on MreB dynamics, was the dependence of motion on peptidoglycan synthesis (Domínguez-Escobar et al., 2011; Garner et al., 2011; van Teeffelen et al., 2011). This was evident when cells were subject to various sub minimum inhibitory concentrations (MIC) of peptidoglycan synthesis inhibiting antibiotics (Domínguez-Escobar et al., 2011; Garner et al., 2011; van Teeffelen et al., 2011). In addition, deletion of individual elongasome associated bPBPs perturbed MreB motion, reducing speed of circumferential motion of the filaments (Domínguez-Escobar et al., 2011). Moreover, depletion of essential peptidoglycan component, DAP, was found to reduce MreB motion (van Teeffelen et al., 2011). This relationship suggests that elongasome dynamics should reflect patterns of active peptidoglycan synthesis by the elongasome and subsequent structure of the cell wall. The distance travelled, or processivity of MreB should be in important parameter in determining how the elongasome constructs the peptidoglycan sacculus and be a read-out of elongasome synthesis events because active synthesis drives elongasome motion.

More recently, the elongasome was reported as one of two peptidoglycan synthesis systems, the other being aPBPs, that work in opposition to one another to maintain cell diameter (Dion et al., 2019). It is suggested that the elongasome is responsible for constructing cylindrical peptidoglycan hoops at 90˚ to the long axis of the cell; an increase of elongasome mediated peptidoglycan synthesis decreases cell diameter. This is opposed by aPBPs, which synthesise shorter, less organised peptidoglycan strands, which cause increased cell diameter. Thus, equilibrium of the two systems is crucial to maintain cell shape. In this model, cylindrical peptidoglycan, which have been observed using AFM (Pasquina-Lemonche et al., 2020) should provide the structural foundation of the sacculus and the primary inward force

opposing the turgor pressure of the cell. The structure of the cylindrical peptidoglycan strands should be reflected by processivity of MreB, which reflects active peptidoglycan synthesis events by the elongasome. This reaffirms importance of elongasome dynamics in cell shape homeostasis.

The mechanism of how elongasome dynamics are regulated has not yet been determined. Single-molecule tracking and SIM studies have revealed interesting dynamics, where MreB was found to pause and reverse (Billaudeau et al., 2017; Dersch et al., 2020; Olshausen et al., 2013), albeit infrequently. Less than 2% of MreB tracks have been found to pause or reverse (Billaudeau et al., 2017). This prompted speculation that MreB dynamics are driven by a multiple molecular motor tug-of-war, where transport motors, in this case presumably peptidoglycan synthases, transiently bind and unbind to the MreB filament. The motors are thought to act in different directions, and the direction with the most motors dictates the direction of motion. MreB filament density has been measured and used to calculate that a multiple motor tug-of-war is unlikely because only one PG strand is synthesised per MreB filament (Billaudeau et al., 2019). Others have speculated that the cell wall itself provides a site for initial MreB localisation to guide peptidoglycan synthesis (Özbaykal et al., 2020). Others state that the MreB filament is oriented at 90˚ to the long axis of the cell by aligning to greatest principle membrane curvature, amplifying regions of already cylindrical peptidoglycan (Hussain et al., 2018). Then, the cell wall provides a template for the complex to replicate (Höltje, 1998). The proposed models are lacking conclusive evidence, however, provide interesting avenues to investigate further.

Studies thus far have used microscopy techniques such as single-molecule tracking, TIRF and SIM-TIRF. While they have provided insight into MreB dynamics and their relationship with cell wall synthesis, the techniques used come with certain limitations. Single-molecule studies have been carried out using fluorescent proteins like GFP (Dersch et al., 2020). The length of time for which it is possible to observe MreB is limited to the photostability and bleaching time of the fluorophore. TIRF based techniques have a limited FOV by design. The depth of illumination of the sample is limited to ~100 nm. This means MreB tracks will leave the FOV, only allowing observation of tracks of approximately 1 µm or shorter. These limitations mean it has only been possible to observe short, incomplete trajectories, meaning a limited amount of information could be obtained; most studies focus on speed, angle and sometimes sparsely

observed events such as reversals. To gain insight into how MreB dynamics are regulated, and what impact they have on cell wall synthesis, it is important to be able to observe the trajectory of MreB dynamics for much longer than currently possible. Because active peptidoglycan synthesis drives elongasome motion, MreB dynamics should reflect patterns of cell wall synthesis and subsequent peptidoglycan structure.

Although whole cells can be imaged when positioned horizontally, poor resolution in the z plane prevents precise localisation or tracking of around the circumference of a rod-shaped cell. This problem has been circumvented in the cell division field, where the goal was to observe protein dynamics moving the circumference of the cell, with the use of VerCINI (Bisson-Filho et al., 2017; Whitley et al., 2021). In this work, VerCINI was used to allow tracking of MreB around the whole cell circumference.

It has been reported that MreB persists in a membrane bound state, either processive, paused, or a combination of the two for around 8 s, determined by single-molecule tracking (Dersch et al., 2020). However, the techniques used in this study have severe limitations when observing whole MreB trajectories. The use of TIRF illumination artificially truncates trajectories. Also, the fluorophore used to label MreB was GFP, which is prone to photobleaching. Recently, photostable Janelia Fluor (JF) dyes have been developed (Grimm et al., 2015) with the incorporation of four-membered azetidine rings into classic fluorophore structures. This produced bright, photostable fluorophores, which are a hallmark of organic dyes, while preserving the cell permeability of classic, net neutral fluorophores.

In this study an MreB-HaloTag fusion was used (Hussain et al., 2018). The use of JF dyes allow various levels of labelling density of MreB. In this chapter, single-molecule labelling is used to allowing the highest resolution of MreB dynamics. By reducing the concentration of JF dye, MreB-HaloTag molecules are labelled, sparsely enough so that single molecule resolution can be achieved. Further to the use of JF dyes, stroboscopic illumination is another important tool in observation of fluorescent fluorophores for extended time periods. By increasing the strobe interval, the time between laser exposure and frames of a time-lapse, the overall laser exposure to the sample is reduced over a fixed time. This reduces the effect of photobleaching, and allows observation of fluorophores for longer time periods (Gebhardt et al., 2013; Mignolet et al., 2016).

The aim of this chapter is to establish a robust SM-VerCINI protocol in order to observe MreB dynamics for extended time periods. This will begin to provide insight into how elongasome dynamics are organised over time to construct the cylindrical peptidoglycan sacculus, playing a critical role in cell shape homeostasis.

3.2 Results

3.2.1 Single-Molecule VerCINI allows high resolution observation of MreB around the whole cell circumference

To observe MreB dynamics, a published strain expressing MreB-HaloTag from its native locus (bYS40) (Hussain et al., 2018) was transformed with *Δhag::erm*^{R} gDNA (Koo et al., 2017). To constrict strain *mreB::mreB-HaloTag Δhag::erm*^{R} (SM01). This was used as the 'wild-type' strain throughout this work. Deletion of the *hag* gene reduces chaining of cells, allowing them to fit in the microholes and prevents motility (Hamze et al., 2009), ensuring cells remain immobile while imaging. MreB-HaloTag was labelled with JF549.

To observe MreB dynamics around the whole circumference of the cell at high resolution, Single-Molecule VerCINI was developed. To identify an effective single-molecule labelling concentration of JF549, *mreB::mreB-HaloTag Δhag::erm*^{R} cells were grown in S750^{glucose} and labelled with various concentrations of dye. Cells were loaded into an agarose VerCINI pad **(Figure 3.1.A)** and imaged for 8 minutes. Images were denoised and registered before kymographs were produced as described **(2.5.2)**. Single-Molecule VerCINI kymographs show fluorescence signal around the circumference of the cell in the X- axis, over time in the Y-axis. Kymographs are displayed with the X-axis repeated to allow visualisation of tracks that travel further than 360˚ around the cell circumference. Diagonal tracks show processive motion around the cell circumference, while vertical lines show static tracks over time. Identification of an effective dye concentration was done qualitatively from the images and resulting kymographs from the 8-minute acquisitions **(Figure 3.1.B-C)**. It was determined that 10 pM dye was optimal, giving enough spatial resolution between MreB tracks, while providing enough observable molecules in a field of view to produce a sufficient volume of data from each imaging session.

3.2.2 Stroboscopic illumination increases the time it is possible to observe MreB

One of the primary aims of this study was to observe MreB for whole subunit lifetimes. To achieve this, stroboscopic illumination was used to reduce the overall laser exposure **(Figure 3.1.D)** to the sample and subsequent effects of photobleaching and phototoxicity. Cells expressing MreB-HaloTag (SM01) were grown in S750^{glucose} and labelled with 10 pM JF549 and

imaged using SM-VerCINI. Acquisitions were taken over 8 minutes, with various strobe intervals ranging from 0.5 s to 8 s, and the total track lifetime was measured from the resulting kymographs **(Figure 3.1.D)**. As strobe interval increased, total track lifetime increased until 6 s strobe interval, where the median observed total track lifetime was 82.00 s [95% CI: 74.00, 88.50]. For all subsequent experiments, a 6 s strobe interval was used for standard imaging conditions. This was preferred to 8 s strobe interval to ensure greater temporal resolution of the images.

With total track lifetime data acquired at various strobe intervals, it was possible to determine the effect of photobleaching, and estimate total MreB subunit lifetime (Gebhardt et al., 2013; Mignolet et al., 2016). The method to determine the effect of bleaching considers the following relationship:

$$\frac{1}{t_{eff}} = \frac{1}{t_{off}} + \frac{1}{t_{bl}}$$

Bleaching time (t_{bl}) of the molecule, in this case JF-549, and the MreB lifetime (t_{off}) convolve to produce the observed lifetime of fluorescence (t_{eff}). The observed lifespans measured using different strobe intervals were plotted, and the following was fit to the data:

$$t_{eff} = \left(\frac{1}{t_{off}} + \frac{t_{int}}{t_{bl}\ t_{tl}} \right)^{-1}$$

Here, t_{int} is the camera integration time, which was a constant 500 ms, t_{tl} is the strobe interval, which was varied. From the fit, bleaching time was determined to be 13.03 s [95% CI: 10.99, 15.21], while the total track lifetime was found to be 127.95 s [95% CI: 108.91, 163.55] (**Figure 3.1.E**).

JF549 is dissolved in DMSO, which is known to perturb membranes (Gurtovenko and Anwar, 2007). To ensure DMSO had a minimal effect on the dynamics of the membrane bound MreB in this study, the JF549 stocks were prepared so that the working concentration of dye was achieved by addition of no more than 1 % DMSO to the culture. Furthermore, once the dye concentration was optimised, at 10 pM, the stock concentration and dilution factor was kept consistent throughout the study to ensure that any effect of DMSO on MreB dynamics was

constant across all experiments when comparing dynamics. It is also possible that the process of loading cells into the VerCINI pad and washing steps could acutely affect cell growth. Cells were allowed to acclimatise for at least 10 minutes after application of the cover slip to reduce the impact of any changes in growth conditions (liquid culture to agarose pad) on MreB dynamics. Moreover, speeds and complex dynamics observed using VerCINI and JF549 in DMSO are consistent with those previously observed with the use of fluorescent proteins (Domínguez-Escobar et al., 2011; Olshausen et al., 2013).

For every SM-VerCINI experiment, processive subtrack speed was plotted against elapsed time for every time-lapse acquisition. This was a quality control measure, ensuring minimal effect of phototoxicity on the sample. The example plot **(Figure 3.1.F)** shows that speed is minimally perturbed over the time-lapse, thus a negligible effect of phototoxicity over the 8 minutes of imaging. The field iris was closed to a point so that only the field of view was illuminated. This was to ensure that only the cells being imaged was exposed to laser illumination and the subsequent effect of phototoxicity. To ensure the viability of the sample over the duration of an imaging session, a control experiment was carried out measuring subtrack speed over the time of an imaging session. Using SM-VerCINI, 2 minute time lapses of different FOVs in the same sample, with 2 s strobe intervals were taken over 47 minutes. MreB speed was found to be unperturbed after 42 minutes after cover slip application, before a reduction in speed at 47 minutes **(Figure 3.1.G)**, presumably owing to oxygen or nutrient depletion. Consequently, data were only acquired up to 40 minutes after application of the cover slip in VerCINI experiments.

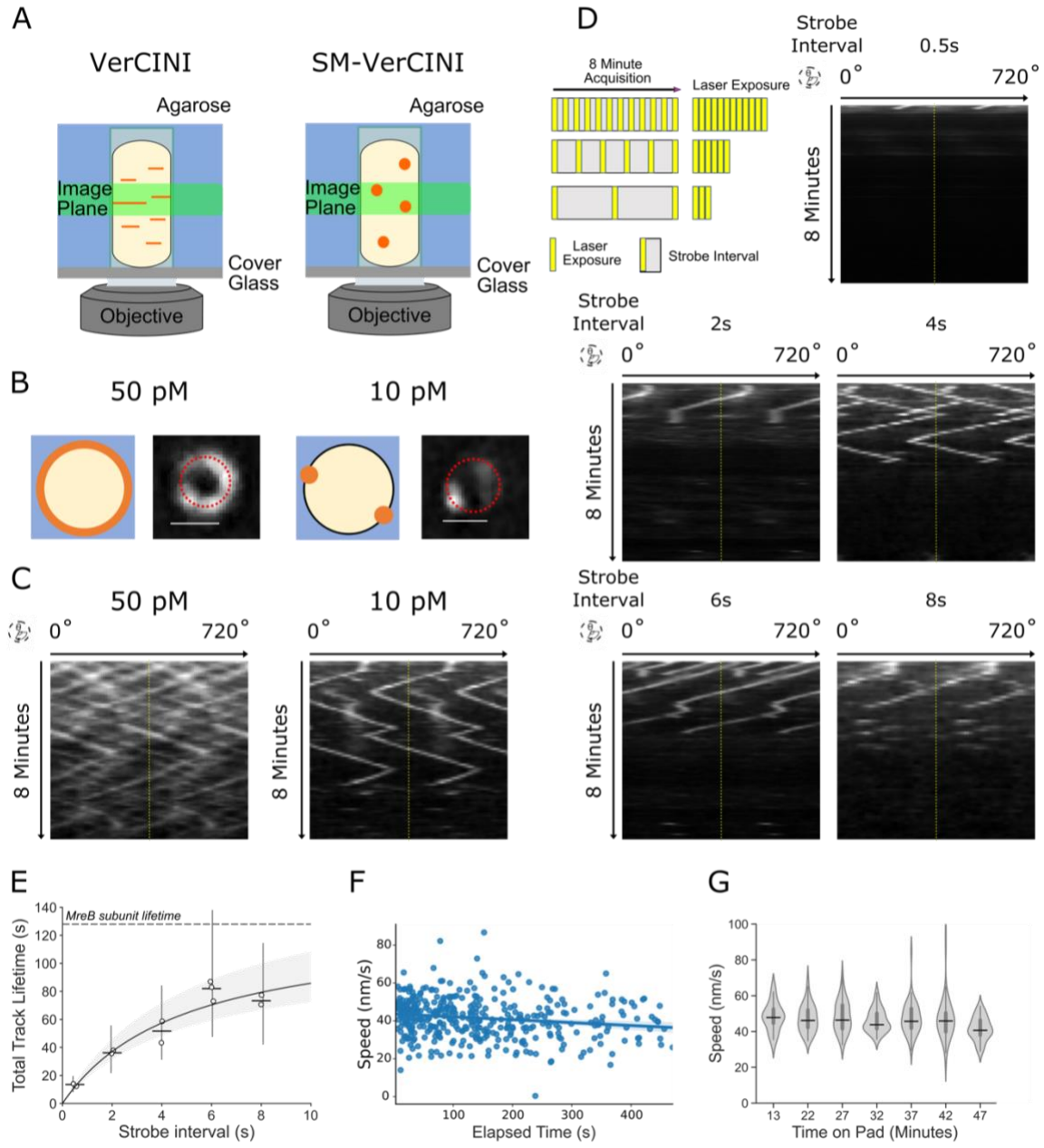

Figure 3.1. Single-Molecule VerCINI setup to observe MreB for whole subunit lifetimes of MreB-HaloTag (JF549) (SM01). **A.** Cartoon representation of VerCINI and Single-Molecule VerCINI setup. **B-C.** Comparison of resolution between VerCINI and Single-Molecule VerCINI. Cells were labelled with 50 pM and 10 pM JF549 for VerCINI and Single-Molecule VerCINI respectively. **B.** Cartoon (left) and actual (right) view from the microscope from VerCINI and Single-Molecule VerCINI. Scale bar, 1 µm. **C.** Resulting kymographs produced from 8-minute time-lapse acquisitions of cells in **B** displayed as signal around 2 times the cell circumference. **D.** Cartoon representation of stroboscopic illumination principle and representative kymographs of 8-minute time lapse acquisitions with various strobe intervals. **E.**

Quantification of observed MreB lifetimes at different strobe intervals. White circles show medians of biological replicates, horizontal lines show overall median while vertical lines show 95 % CI MreB subunit lifetime, corrected for photobleaching. **F.** Representative linear regression control plot used to monitor phototoxicity during an 8-minute time-lapse showing speed of MreB subtracks over the 8-minute acquisition. Blue line shows the linear regression model, while the blue shaded area shows the 95 % CI of the model. **G.** Effect of over an imaging session. Using Single-Molecule VerCINI, 40 s time-lapse acquisitions with 2 s strobe intervals were taken. Violin plots show MreB speeds at different timepoints in the imaging session. Horizontal lines show medians and vertical lines show IQR.

3.2.3 MreB subunits are highly processive, change direction and display state switching much more frequently than previously observed

Using data from the optimised imaging protocol, numerous of MreB dynamics **(Figure 3.2.A)** were measured from the resulting kymographs **(Figure 3.2.B)**. Firstly, the total track lifetime was observed to be a median of 82.00 s [95% CI: 74.00, 88.50] **(Figure 3.2.C)**, which is 10-fold longer than recently published measurements (Dersch et al., 2020). Further, when accounting for photobleaching, the total track lifetime was determined to be 128 s [95% CI: 109s, 164s]. Because it was possible to track MreB for such extended timescales, numerous other dynamics (defined in **Table 2.5.2**) are possible to identify. Total tracks could be separated into processive and static subtracks, with median processive subtrack lifetimes measured as 40.50 s [95% CI: 39.00, 43.00] and median paused subtracks lasting 27.00 s [95% CI: 24.00, 29.50] **(Figure 3.2.C)**. Processivity is a key measurement throughout this study, owing to its implications on glycan strand synthesis. In our standard S750^{glucose}, 30˚C growth conditions, median processivity was measured as 1.61 µm [95% CI: 1.51, 1.69] **(Figure 3.2.D)**, which is more than 3-fold longer than previous measurements (Dersch et al., 2020). MreB tracks were found to have a median total displacement of 2.70 µm [95% CI: 2.45, 2.91] **(Figure 3.2.D)**. Median MreB speed was found to be 40.81 nm/s [95% CI: 40.12, 41.45] **(Figure 3.2.E)**.

The ability to detect switching between processive and paused states is a key benefit of tracking MreB for such long timescales. Indeed, the rates of switching between these states, which were previously observed, but thought to be sporadic events (Olshausen et al., 2013), can be robustly quantified. MreB was found to be in a processive state for a median of 80.64

% of the time, and in a static state for a median of 19.36 % of the time **(Figure 3.2.F)**. Under these imaging conditions, diffusive MreB was not observed owing to the long strobe interval used. While in a processive state, MreB was found to reverse a median 0.36 [95% CI: 0.32, 0.40] times, pause 0.25 [95% CI: 0.22, 0.28] times and unbind 0.61 [95% CI: 0.57, 0.65] times per minute **(Figure 3.2.F)**. Paused MreB was found to initiate motion 0.96 [95% CI: 0.78, 1.15] times and unbind 0.49 [95% CI: 0.41, 0.58] times per minute **(Figure 3.2.F)**. Nucleation events were also observed, with the nucleation of 55.02 % of tracks observed within the time-lapse **(Figure 3.2.G)**. The other 44.98% of tracks were existing already on the cell circumference at the outset of the time-lapse **(Figure 3.2.G)**. Overall, >55 % of processive tracks were found to display state switching properties, either pausing or reversing, this is substantially more than previously reported, where <2 % of tracks were observed to display reversal or pausing events (Billaudeau et al., 2017). This highlights the importance of observing MreB for longer time periods than was previously possible.

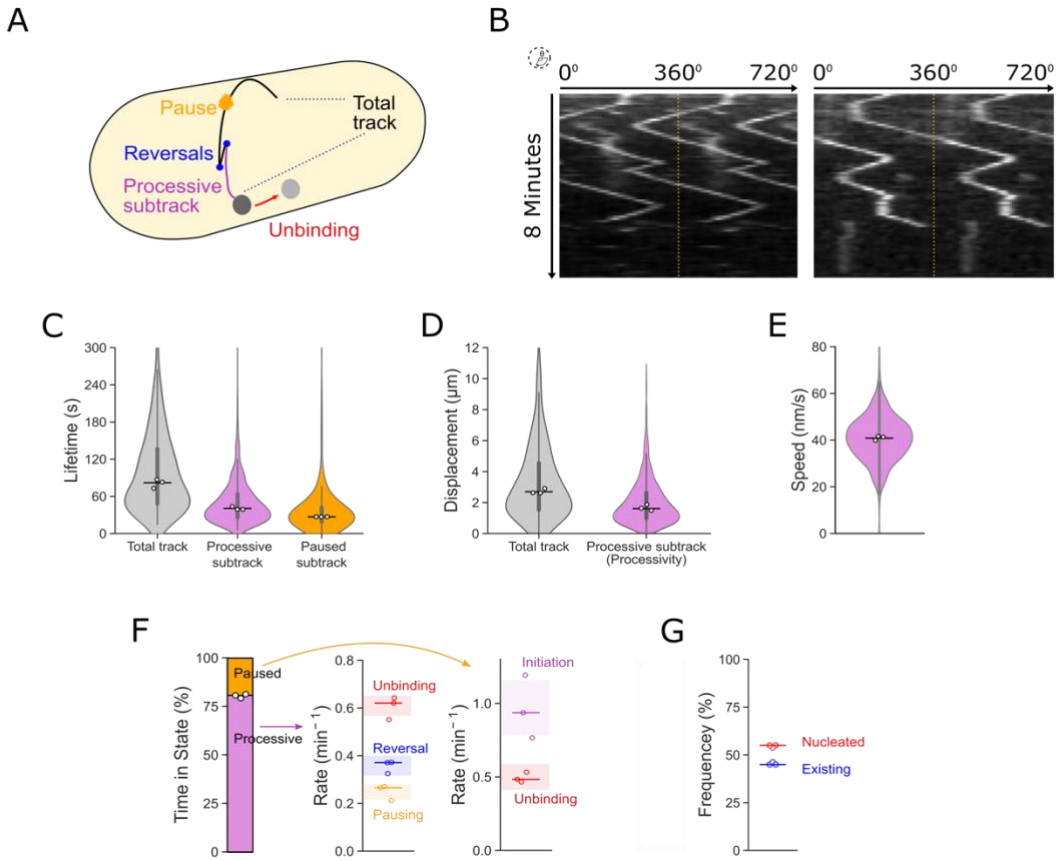

Figure 3.2. Quantification of MreB-HaloTag (JF549) (SM01) dynamics observed using Single-Molecule VerCINI. **A.** Cartoon representation of MreB dynamics observed using Single-Molecule VerCINI. **B.** Exemplar kymographs showing MreB-HaloTag (JF549) signal around the cell circumference over 8-minute time-lapse acquisitions. **C-E.** Violin plots showing lifetimes and displacements of total tracks and subtracks and speeds of processive subtracks. White circles show medians of biological replicates, horizontal lines show overall median while vertical lines show IQR. **F.** Time in processive and static stated and rates of switching from each state. Shaded areas show 95% CI. **G.** Quantification of existing and nucleated tracks. Circles are medians of biological replicates, and horizontal lines are overall medians.

Table 3.2.1. Medians and 95% Cis of MreB-HaloTag dynamics measured by SM-VerCINI shown in **Figure 3.2**.. 3 biological replicates were conducted for this experiment.

	n	Median	95% CI, low	95% CI, high
Total Track Lifetime (s)	647	82.00	74.00	88.50
Processive Subtrack Lifetime (s)	1078	40.50	39	43.00
Paused Subtrack Lifetime (s)	315	27.00	24.00	29.50
Total Displacement (µm)	647	2.70	2.45	2.91
Processivity (µm)	1078	1.61	1.51	1.69
Speed (nm/s)	1078	40.81	40.32	41.45
Time in Processive State (%)	3	80.64		
Reversals per minute ($Rate^{-1}$)	1078	0.36	0.32	0.40
Pauses per minute ($Rate^{-1}$)	1078	0.25	0.22	0.28
Unbind After Processive per minute ($Rate^{-1}$)	1078	0.61	0.57	0.65
Initiation After Pause per minute ($Rate^{-1}$)	315	0.96	0.78	1.15
Unbind After Pause per minute ($Rate^{-1}$)	315	0.49	0.41	0.58

3.3 Discussion

Since the first studies in 2011 revealing motile MreB patches (Domínguez-Escobar et al., 2011; Garner et al., 2011; van Teeffelen et al., 2011), various light microscopy techniques have been employed to observe MreB dynamics in as much detail as possible to study their impact on cell wall construction. Here, single-molecule microscopy has been combined with VerCINI to acquire an in-depth analysis of MreB subunit dynamics not possible using previously used techniques. VerCINI allowed tracking of MreB around the whole cell circumference, removing the limitations of TIRFM, and the increased resolution achieved by single-molecule labelling. Moreover, the high photostability of JF549 and stroboscopic illumination ameliorated the effect of photobleaching of the fluorophore, thus allowing tracking longer than possible with previously used techniques.

The total track lifetime, even once photobleaching has been accounted for, is likely a lower bound of the true MreB subunit lifetime. Many of the tracks analysed were already in progress from the outset of the time-lapse **(Figure 3.2.G)**, meaning the track is truncated and the whole track is not observed. In addition, it is possible that some MreB filaments move out if the focal plane, which is around 500 nm thick, during the trajectory. The impact of these events on the dynamics measured should be limited as multiple studies using various imaging techniques and fusion proteins have demonstrated that most MreB motion is at 90˚ to the long axis of the cell with some variation (Domínguez-Escobar et al., 2011; Garner et al., 2011; van Teeffelen et al., 2011), including the MreB-HaloTag fusion used throughout this study (Hussain et al., 2018). Despite these minor limitations, it has been possible to observe MreB trajectories for longer than previously published.

SIM-TIRF has been used with the aim of measuring whole MreB trajectories (Dersch et al., 2020). The study found MreB trajectories to have a total track lifetime of 8 s. Firstly, GFP was used as the fusion protein, which is much less photostable and prone to photobleaching than JF549 used in this study. It is argued that low laser power at 1 mW/50 μm^2 was used to minimise the effect, however no evidence of the suggested negligible effect of photobleaching was provided, whereas the effect has been explicitly defined in this study **(Figure 3.1.E)**. Also, the use of TIRF illumination in the system is certain to truncate

trajectories, with only a subsection of the cell circumference proximal to the cover slip illuminated. This is a crucial advantage of the use of SM-VerCINI in this work.

The trajectories of single MreB subunits measured is representative of whole MreB filaments, as previous FRAP experiments (Domínguez-Escobar et al., 2011) have ruled out subunit turnover within a filament.

This suggests that the whole MreB trajectories measured are representative of whole filament motion. Moreover, because MreB motion is dependent on peptidoglycan synthesis, MreB trajectories should infer patterns of synthesis carried out by elongasome complexes upon the MreB filament. One of the primary findings of our work was the processivity of MreB. I found that MreB moves 1.6 μm around the circumference **(Figure 3.2.D)** in one direction without interruption, inserting nascent peptidoglycan into the sacculus. This is measured at a similar order of magnitude as the length of single glycan chains isolated from *B. subtilis* and measured *in vitro* using AFM (Hayhurst et al., 2008), consistent with a direct relationship between MreB processivity and initial glycan strand length.

The frequency of reversals and switching between processive and paused states **(Figure 3.2.F)** was also found to be higher than previously reported (Dersch et al., 2020; Olshausen et al., 2013), where such events were sparsely observed. The high frequency of these events supports further a tug-of-war model suggested previously (Olshausen et al., 2013), where multiple molecular motors transiently bind and drive motion of MreB, competing with opposing motors for directionality. However, the findings do not conclusively rule out a template model (Özbaykal et al., 2020) where landmarks in the cell wall dictate arrest or direction change of processive MreB motion. The ability to robustly quantify switching rates between processive and static states, together with reversal rate allowed further investigation into the intricacies of MreB dynamics to give insight into the mechanism and regulation of elongasome motion presented in subsequent chapters of this thesis.

Thus far in this study, a novel approach has been developed to track MreB dynamics, revealing a great deal about how the filament moves processively around the circumference of the cell, pausing and changing direction. Although the data tentatively suggest a tug-of-war model,

further work was needed to probe the mechanism of elongasome dynamics and its role in constructing the peptidoglycan sacculus.

Chapter 4: Effect of growth rate and MltG on MreB dynamics

4.1 Introduction

With an optimised protocol to observe single-molecule MreB dynamics for such long time periods, it is now possible to use the method to explore how dynamics are regulated and how any changes affect cell growth and morphology. Important parameters which can now be robustly measured such as processivity and switching rate between states will give a much more detailed portrayal of how the elongasome moves over time to synthesise peptidoglycan, contributing to cell shape homeostasis.

The relationship between cell growth and elongation rate is well established (Galinier et al., 2021), if not comprehensively defined. MreB has been found to travel faster in rich media compared to poor media (Billaudeau et al., 2017). The changes in MreB dynamics are associated with flotillin mediated membrane fluidity (Zielińska et al., 2020). More recently, it was reported that changes in growth rate brought about by changing the richness of growth media has minor effects on MreB speed, where PrkC was found to modulate MreB filament density and subsequent growth rate by monitoring peptidoglycan precursor levels (Sun and Garner, 2022). The growth rate changes in this study are brought about by merely changing carbon source in S750 media (with the exception of CH and LB media), which is a more robust method to determine how growth rate affects the elongasome. Whereas in the earlier study (Billaudeau et al., 2017), only LB and S media were compared, which have multiple differences in makeup. Both studies do report changes in elongasome density with different growth rate.

When MreB was observed using SIM-TIRF, filament density was found to increase with growth rate, but not proportionally (Dion et al., 2019), suggesting density is not the sole mechanism of elongation rate control by the elongasome. I proposed that MreB dynamics such as processivity or speed as well as filament density may cumulatively contribute to changes in growth and elongation rate.

MreB filaments have been found to localise to areas of greatest principle membrane curvature (Hussain et al., 2018). In addition, in *E. coli*, the transpeptidase, PBP2, was found to identify initial localisation sites for the elongasome, and it is suggested that this is determined

by local landmarks within the cell wall (Özbaykal et al., 2020). These findings suggest that the cell wall itself provides a template for the elongasome to amplify existing peptidoglycan to construct a uniform rod- shaped sacculus. Given that MreB travels in the same orientation of the glycan strands in peptidoglycan. I hypothesised that glycan strand termini provide localisation sites for peptidoglycan synthesis initiation and termination and glycan strand length determines processivity of the elongasome.

MltG is a lytic transglycosylase that has been proposed to terminate glycan strands within peptidoglycan; deletion of *mltG* was found to increase glycan length (Yunck et al., 2016). In this model, the longer glycan strands produced by deletion of *mltG* would cause longer elongasome processivity and less frequent reversals and pauses, owing to fewer termini sites to end active synthesis.

The aim of this chapter was to investigate possible regulators of elongasome dynamics that are not directly associated with the complex itself. Firstly, I aimed to determine if elongasome dynamics provide further regulation of growth rate in addition to density. Also, I aimed to test the peptidoglycan template model by exploring how termination of glycan strands affects MreB dynamics, in particular processivity.

4.2 Results

4.2.1 Effect of media induced growth rate on MreB dynamics

Given the importance of the elongasome on growth rate, I investigated whether elongasome dynamics, as well as density modulated elongation and growth rate. S750^{glucose} was used as the standard growth media for all SM-VerCINI experiments in this study. To reduce growth rate, glucose was replaced with maltose as the sole carbon source in the media and to increase growth rate casamino acids (CAA) were added to S750^{glucose}. Single-molecule MreB dynamics were measured in strain SM01 (*mreB::mreB-HaloTag Δhag::erm^{R}*) in S750^{Maltose} and S750^{CAA} using SM-VerCINI.

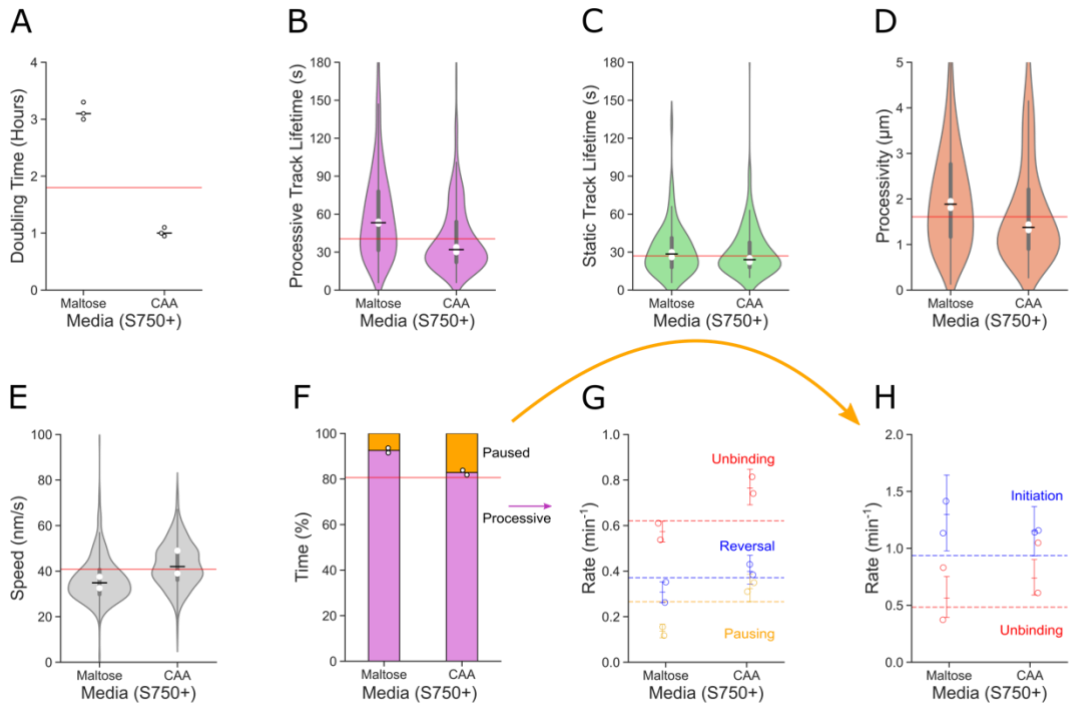

Figure 4.1. Effect of different growth media on growth rate and MreB dynamics. **A.** Growth rate of strain SM01 (*mreB::mreB-HaloTag Δhag::erm^{R}*) in different growth media. **B-I.** MreB-HaloTag (JF549) dynamics measured using SM-VerCINI in strain SM01 (*mreB::mreB-HaloTag Δhag::erm^{R}*) over 8 minute time-lapse acquisitions in different growth media. **B-E.** Violin plots processive and static subtrack lifetime and speed. White circles show medians of biological replicates, horizontal lines show overall median while vertical lines show IQR. Red lines show S750^{glucose} medians. **F-H.** Time in processive and static stated and rates of switching from each

state. Circles show biological replicate medians. Horizontal lines show $S750^{glucose}$ medians. Error bars show 95% CI.

When grown in $S750^{maltose}$, OD_{600} doubling time was a median of 3.1 hours, whereas in $S750^{CAA}$, doubling time was a median of 1.0 hour compared to the doubling time in standard $S750^{glucose}$, which was a median of 1.8 hours (**Figure 4.1.A**).

When cells were cultures in $S750^{maltose}$, single-molecule MreB processive subtrack lifetime and processivity were found to be higher than in standard $S750^{glucose}$ conditions; median processive subtrack lifetime was measured at a median of 53.25 s [95% CI: 48.00, 57.00].with a median difference of 12.75 s [95% CI: 7.00, 16.75] standard $S750^{glucose}$ conditions (**Figure 4.1.B**) and processivity was measured at a median of 1.89 µm [95% CI: 1.76, 2.05], with a median difference of 0.28 µm [95% CI: 0.11, 0.44] (**Figure 4.1.D**) compared to standard $S750^{glucose}$ conditions. In the slower growth conditions, MreB speed was also reduced by a median difference of -5.95 nm/s [95% CI: -6.85, -5.01] compared to $S750^{glucose}$ conditions to 34.85 nm/s [95% CI: 34.17, 35.66] (**Figure 4.1.E**). In contrast, when cells were cultured in $S750^{CAA}$, processive subtrack lifetime was found to decrease, at 32.00 s [95% CI: 30.00, 34.00] by a median difference of -8.49 s [95% CI: 10.99, -5.00} (**Figure 4.1.B**) compared to $S750^{glucose}$. Processivity also reduced to a median of 1.38 µm [95% CI: 1.28, 1.44] by a median difference of -0.23 µm [95% CI: -0.36, -0.13] (**Figure 4.1.D**) compared to standard $S750^{glucose}$. Speed also slightly increased in $S750^{CAA}$ to 42.00 nm/s [95% CI: 40.90, 43.33] by a median difference of 1.18 nm/s [95% CI: 0.01, 2.71] (**Figure 4.1.E**) compared to $S750^{glucose}$.

The above data suggest that elongasome dynamics have a role in growth rate. The differences in dynamics such as speed and processivity are minor in comparison to the differences in growth rate, therefore are not solely responsible for regulation of growth rate. Indeed, the changes in MreB dynamics observed together with changes in elongasome density (Sun and Garner, 2022) may have a cumulative effect on growth rate.

Table 4.2.1. Medians and 95% CIs of MreB-HaloTag dynamics in different growth media measured by SM-VerCINI shown in **Figure 4.1**. 2 biological replicates were conducted for this experiment. Median differences (Δ Median) and CIs on median differences are relative to $S750^{glucose}$ values in **Table 3.2.1** except for comparisons between CAA and Maltose.

	n	Median	95% CI, low	95% CI, high	Δ Median	95% CI, low	95% CI, high
Processive Subtrack Lifetime (s)							
Maltose	484	53.25	48.00	57.00	12.75	7.00	16.75
CAA	498	32.00	30.00	34.00	-8.49	-10.99	-5.00
CAA-Maltose					-21.25	-25.00	-15.00
Processivity (μm)							
Maltose	484	1.89	1.76	2.05	0.28	0.11	0.44
CAA	498	1.38	1.28	1.44	-0.23	-0.36	-0.13
CAA-Maltose					-0.51	-0.68	-0.35
Speed (nm/s)							
Maltose	484	34.86	34.17	35.66	-5.95	-6.85	-5.01
CAA	498	42.00	40.90	43.33	1.18	0.01	2.71

4.2.2 Effect of *ΔmltG* on MreB dynamics

To explore the hypothesis that existing peptidoglycan provides a template track for the elongasome to amplify cylindrical cell wall, the effect of the glycan terminase, MltG on single-molecule MreB dynamics was explored. To delete the non-essential *mltG*, strain SM41 (*mreB::mreB-HaloTag Δhag::erm^R ΔmltG:kan^R*) by transforming SM01 (*mreB::mreB-HaloTag Δhag::erm^R*) with gDNA from *ΔmltG* from the BKK knockout library (Koo et al., 2017). If the template track model was accurate, that the deletion of *mltG* would produce longer glycan strands because of less glycan termination activity and increase processivity of the elongasome. SM-VerCINI was used to observe single-molecule MreB dynamics in the *ΔmltG* background.

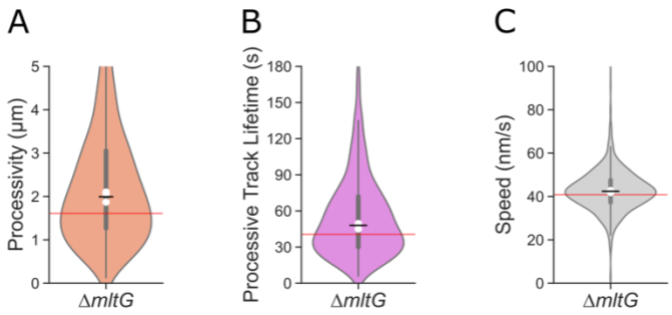

Figure 4.2. Effect of *ΔmltG* on MreB dynamics. MreB-HaloTag (JF549) dynamics measured using SM-VerCINI in strain SM41 (*mreB::mreB-HaloTag Δhag::erm*^{R} *ΔmltG:kan*^{R}) over 8 minute time-lapse acquisitions. **A-C.** Violin plots showing processivity, processive subtrack lifetime and speed. White circles show medians of biological replicates, horizontal lines show overall median while vertical lines show IQR. Red lines show WT (*mreB::mreB-HaloTag Δhag::erm*^{R}) medians.

MreB processivity was found to increase to 1.99 μm [95% CI: 1.88, 2.08], by a median difference of 0.38 μm [95% CI: 0.25, 0.52] compared to WT (**Figure 4.2.A**). MreB was found to travel at a speed consistent with WT, at 42.38 nm/s [95% CI: 41.78, 42.80] (**Figure 4.2.C**), and the increase in processivity seemingly caused by an increase in processive subtrack lifetime to 48.00 s [95% CI: 45.00, 50.00], by a median difference of 7.50 s [95% CI: 4.00, 10.50] (**Figure 4.2.B**). The increase in processivity upon deletion of *mltG* is relatively minor and suggests the role of MltG in regulation of elongasome dynamics is limited.

Table 4.2.2. Medians and 95% Cis of MreB-HaloTag dynamics in SM41 (*mreB::mreB-HaloTag Δhag::erm^R ΔmltG:kan^R*) measured by SM-VerCINI shown in **Figure 4.2**. 3 biological replicates were conducted for this experiment. Median differences (Δ Median) and CIs on median differences are relative to WT (SM01) values in **Table 3.2.1**.

	n	Median	95% CI, low	95% CI, high	Δ Median	95% CI, low	95% CI, high
Processive Subtrack Lifetime (s)							
ΔmltG	1221	48.00	45.00	50.00	7.50	4.00	10.50
Processivity (μm)							
ΔmltG	1221	1.99	1.88	2.08	0.38	0.25	0.52
Speed (nm/s).							
ΔmltG	1221	42.38	41.78	42.80	1.56	0.77	2.25

4.3 Discussion

The ability to observe single-molecule MreB dynamics for such long time periods by the SM-VerCINI method developed and optimised in chapter 3 has allowed in-depth investigation of how complex elongasome dynamics in various conditions. Changes in growth rate induced by different culture media were the first and most crude conditions in which complex MreB dynamics were compared.

Complex MreB dynamics were observed to differ when growth rate was changed by varying culture media. In slower growth conditions, a minor increase in processive subtrack lifetime and processivity was measured, while MreB was found to travel at a slower speed than in standard conditions. When growth rate was increased upon the addition of CAA to growth media, the opposite is true, where processive subtrack lifetime, processivity and speed all increased compared to standard growth conditions. As growth rate increases, the elongasome must increase production of cylindrical cell wall proportionally to maintain a rod-shaped sacculus of uniform length. The changes in dynamics are minor relative to the differences in growth rate between the different media tested. The differences observed therefore must be part of a more holistic response by the elongasome to growth rate, which includes the change in elongasome filament density (Sun and Garner, 2022). Another variable which could contribute to the increase in elongasome dependent peptidoglycan synthesis is stoichiometry of the peptidoglycan synthases on the MreB filament. It is possible that as growth rate increases, more peptidoglycan synthases are recruited to the MreB filament to synthesis more peptidoglycan strands per filament, increasing overall elongasome activity. This theme is explored in chapter 5.

To explore the hypothesis that peptidoglycan provides a template for the elongasome to amplify cylindrical peptidoglycan, MreB dynamics were measured in a *ΔmltG* background whether the changes in cell wall properties caused by deletion of the glycan terminase caused subsequent changes in elongasome dynamics. If this model were accurate, I expected that when *mltG* was deleted, processivity of MreB would increase, because the template would be longer owing to fewer glycan termination events by MltG (Yunck et al., 2016).

When MreB dynamics were measured using SM-VerCINI in a *ΔmltG* background, processivity was found to be slightly longer than that in the WT strain. This finding does support the template track model. Since this experiment was carried out it has been reported that MltG does indeed have lytic glycosyltransferase activity producing shorter glycan strands (Sassine et al., 2021). In the study, MltG was found to compete with aPBPs, but not affect their glycosyltransferase activity. MltG was found to cleave newly synthesised glycans after around 7 disaccharides, however some longer glycans were found in the pulldown experiments. The shorter glycans are thought not thought to be incorporated into the sacculus, rather used for another unknown cellular process because it was found inactive against crosslinked peptidoglycan (Sassine et al., 2021). This conflicts with the basis of my experiment where *ΔmltG* was a means of increasing sacculus glycan strands length to test the template track model.

Chapter 5: Effect of elongasome associated peptidoglycan synthases on MreB dynamics

5.1 Introduction

As growth rate and *ΔmltG* were found to have little effect, I explored whether MreB dynamics were regulated intrinsically by members of the elongasome as proposed previously (Olshausen et al., 2013). The elongasome is a complex of proteins, including peptidoglycan synthases, which assemble upon an MreB filament of ~200 nm in length.

The functionally redundant (Kobayashi et al., 2003) PBP2A (encoded by *pbpA*) and PBPH provide transpeptidase activity to the elongasome (Wei et al., 2003). They have been found to co-localise with the MreB filament *in vivo* (Domínguez-Escobar et al., 2011; Garner et al., 2011). When either *pbpA* or *pbpH* is deleted, MreB speed was reportedly reduced (Domínguez-Escobar et al., 2011). In addition, MreB speed is perturbed upon treatment with transpeptidase targeting antibiotics (Domínguez-Escobar et al., 2011; Garner et al., 2011; van Teeffelen et al., 2011). The dependence of MreB motility on activity of at least one of the transpeptidases, suggests they may be responsible for the regulation of complex MreB dynamics.

RodA is essential (Kobayashi et al., 2003) and is seen to co-localise with and move processively at similar speeds to the elongasome (Domínguez-Escobar et al., 2011) and has more recently been identified as the glycosyltransferase of the complex (Cho et al., 2016; Emami et al., 2017). RodA is the other peptidoglycan synthase in the complex in addition to the PBPs, suggesting it may play a role in regulating the complex dynamics of MreB and the elongasome. Furthermore, when RodA expression is increased or decreased relative to WT levels, cell diameter is found to increase (Dion et al., 2019) showing a dependence of cell shape on the glycosyltransferase. When RodA is depleted, it is likely that the cell widens because of a decrease of elongasome peptidoglycan synthase activity. As RodA is required for glycosyltransferase activity in the elongasome (Emami et al., 2017), when it is depleted there are fewer actively peptidoglycan synthesising complexes. This results in an imbalance of synthesis between aPBPs and the elongasome, resulting in more aPBP synthesised

peptidoglycan and an increased diameter. Why diameter increases with RodA overexpression is more ambiguous. The authors of the study propose that once the elongasome is saturated with RodA, any surplus acts independent of the elongasome, contributing to aPBP peptidoglycan synthesis activity which causes the cell to widen. However, further experimentation is required. In this chapter, I will explore how the elongasome responds to RodA overexpression and aim to shed light on this mechanism.

The stoichiometry of the elongasome is unknown, however it was suggested that multiple molecular motors could bind and unbind to the MreB filament (Olshausen et al., 2013) and this regulates elongasome dynamics. In this model, the number of motors on the filament should affect dynamics such as processivity and switching rates. Active peptidoglycan synthesis drives motion of the elongasome, therefore it is likely that dynamics are regulated by one or more of the elongasome associated peptidoglycan synthases, RodA, PBPA and PBPH **(Figure 1.3)**. MreB dynamics are proposed by Olshausen *et al.* to be regulated by binding and unbinding of peptidoglycan synthases, or molecular motors, to the MreB filament. By altering cellular levels of the molecular motors, the stoichiometry of motors on the filament should subsequently change and affect MreB dynamics. Other studies have provided contrasting evidence that the tug-of-war is unlikely because only one PG strand is synthesized per MreB filament (Billaudeau et al., 2019). Moreover, others have suggested that the cell wall provides a template for amplification of existing peptidoglycan (Höltje, 1998; Hussain et al., 2018).

The aim of this chapter is to further exploit the SM-VerCINI protocol developed in chapter 3 to elucidate the role of elongasome associated peptidoglycan synthases in MreB filament transport. In the chapter, each of the peptidoglycan synthases in the complex will be genetically perturbed to isolate specific regulators of complex MreB dynamics such as processivity and switching rates, and what effect any changes in elongasome dynamics have on sacculus construction and cell shape.

5.2 Results

5.2.1 Effect of single bPBP knockouts on MreB dynamics

Because of previous findings showing MreB speed is reduced upon deletion of either of the elongasome associated transpeptidases (Domínguez-Escobar et al., 2011), SM-VerCINI was used to measure more complex MreB dynamics. Strains SM22 (*mreB::mreB-HaloTag Δhag::erm^R ΔpbpA::kan^R*) and SM23 (*mreB::mreB-HaloTag Δhag::erm^R ΔpbpH::kan^R*) were constructed by transforming SM01 (*mreB::mreB-HaloTag Δhag::erm^R ΔpbpA::kan^R*) with gDNA from the BKE strain library (Koo et al., 2017) to allow observation of single-molecule MreB dynamics in transpeptidase knockout backgrounds.

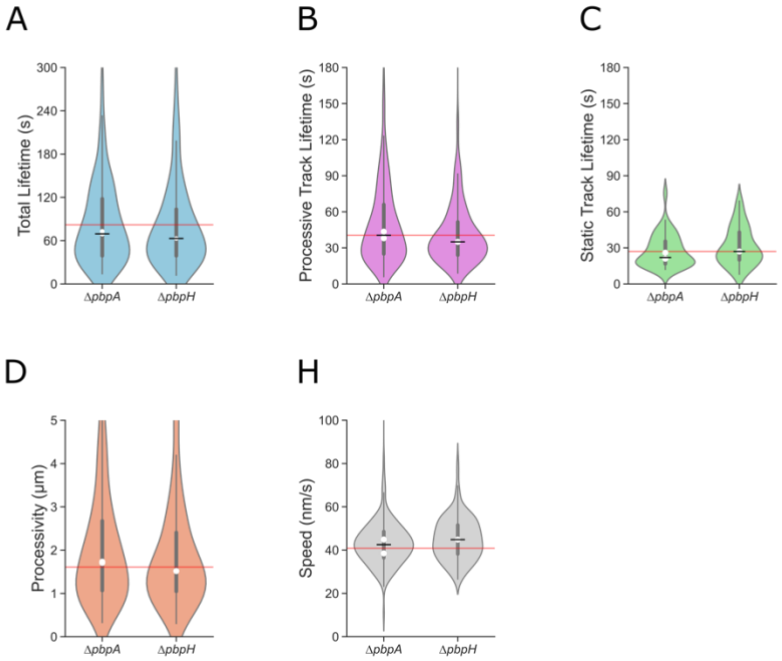

Figure 5.1. Effect of elongasome associated transpeptidase knockouts on MreB dynamics. MreB-HaloTag (JF549) dynamics measured using SM-VerCINI in strains SM22 (*mreB::mreB-HaloTag Δhag::erm^R ΔpbpA::kan^R*) and SM23 (*mreB::mreB-HaloTag Δhag::erm^R ΔpbpH::kan^R*) over 8 minute time-lapse acquisitions. **A-E.** Violin plots showing lifetimes, processivity and speeds. White circles show medians of biological replicates, horizontal lines show overall median while vertical lines show IQR. Red lines show WT (*mreB::mreB-HaloTag Δhag::erm^R*) medians.

Unfortunately, due to time constraints, it was not possible to acquire SM-VerCINI in the *ΔpbpH* strain in replicate, so for more conclusive data, a repeat experiment should be carried out. MreB dynamics in ΔpbpA and *ΔpbpH* were found to be similar to WT (**Figure 5.1**). No changes in were found to suggest that any of the transpeptidases are solely responsible for determining elongasome dynamics. Another biological replicate in the *ΔpbpH* background would help confirm the findings. Unlike previous findings (Domínguez-Escobar et al., 2011), MreB speed was not perturbed when either of the transpeptidases were deleted **(Figure 5.1.H**). These data were unexpected, as they conflict with previous findings that MreB speed is perturbed upon deletion of *pbpA* and *pbpH* (Domínguez-Escobar et al., 2011).

Several differences between the experiments carried out in this project and those by Domínguez-Escobar and colleagues prevent direct comparison. To ensure that the MreB-HaloTag fusion and S750^{glucose} media used in my experiments did not have any compensatory effect on MreB speeds upon transpeptidase deletion, a control experiment was conducted with the use of strain HS553 (*trpC2 mreB::mreB-msfGFP-mreB*). SM26 (*trpC2 mreB::mreB-msfGFP-mreB ΔpbpA::kan*) and SM27 (*trpC2 mreB::mreB-msfGFP-mreB ΔpbpH::kan*) were constructed by transforming HS553 (*trpC2 mreB::mreB-msfGFP-mreB*) with gDNA from the BKK knockout library (Koo et al., 2017).

To determine the effect of single bPBP knockouts on MreB-msf-GFP-MreB speed, HS553 (*trpC2 mreB::mreB-msfGFP-mreB*), SM26 (*trpC2 mreB::mreB-msfGFP-mreB ΔpbpA::kan*) and SM27 (*trpC2 mreB::mreB-msfGFP-mreB ΔpbpH::kan*) were cultured in LB at 30˚C and MreB-msf-GFP-MreB observed using TIRF microscopy. Speeds were measured by manual kymograph analysis (**2.6.3**). The speed perturbation reported (Domínguez-Escobar et al., 2011) when either of the transpeptidases were deleted was not observed in this strain background **(Figure 5.2)**. In *ΔpbpA*, MreB speed reduced minimally to 55.71 nm/s [95% CI: 52.00, 58.50] with a median difference of -2.06 nm/s [95% CI: -6.50, -1.63] compared to WT, whereas speed was seen to increase to 65.00 nm/s [95% CI: 60.36, 65.00] with a median difference of 7.22 nm/s [95% CI: 1.86, 10.90] in comparison to WT *ΔpbpH*, as seen in the SM01 strain background (*mreB::mreB-HaloTag Δhag::erm*^{R}). This supports the data seen in my SM-VerCINI experiments **(Figure 5.1)**.

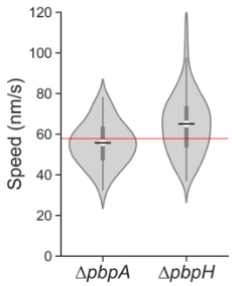

Figure 5.2. Effect of elongasome associated transpeptidase knockouts on MreB speed in *B. subtills* 168CA. Speeds of MreB-msf-GFP-MreB in SM26 (*trpC2 mreB::mreB-msfGFP-mreB ΔpbpA::kan*) and SM27 (*trpC2 mreB::mreB-msfGFP-mreB ΔpbpH::kan*) measured by TIRF microscopy in LB over 40 s time-lapse acquisitions. White circles show medians of biological replicates, horizontal lines show overall median while vertical lines show IQR. Red line shows WT (HS553) (*trpC2 mreB::mreB-msfGFP-mreB*) median.

Because of the functional redundance of the two genes, it is possible that when one of the bPBPs is deleted, the other is sufficient to support WT-like elongasome activity. An attempt was made to construct a strain to knock out *pbpH* and place *pbpA* under an inducible promoter to allow further depletion of elongasome associated transpeptidases, however I was not able to construct this strain during the project.

Table 5.2.1. Medians and 95% Cis of MreB-msfGFP-MreB dynamics HS553 (*trpC2 mreB::mreB-msfGFP-mreB*), SM26 (*trpC2 mreB::mreB-msfGFP-mreB ΔpbpA::kan*) and SM27 (*trpC2 mreB::mreB-msfGFP-mreB ΔpbpH::kan*) measured by TIRF microscopy shown in **Figure 5.2**. Median differences (Δ Median) and CIs on median differences are relative to HS553 values. This experiment was not repeated.

	n	**Median**	**95% CI, low**	**95% CI, high**	**Δ Median**	**95% CI, low**	**95% CI, high**
Speed (nm/s)							
WT (HS553)	187	57.78	54.17	58.50			
ΔpbpA	75	55.71	52.00	58.50	-2.06	-6.50	1.63
ΔpbpH	165	65.00	60.36	65.00	7.22	1.86	10.9

5.2.2 Effect of RodA expression on MreB dynamics

The glycosyltransferase, RodA, was another likely candidate for an intrinsic regulator of elongasome dynamics, which are dependent on peptidoglycan synthesis, and the direction of travel of the complex is in the same orientation of glycan strands. As *rodA* is essential, to explore its role in MreB dynamics an IPTG dependent strain was constructed by transforming SM01 (*mreB::mreB-HaloTag Δhag::erm*^{R}) with gDNA from the published strain YK2245 (*rodA::kan*^{R}*-P*$_{spac}$*-rodA*) (Emami et al., 2017) to produce SM28 (*mreB::mreB-HaloTag Δhag::erm*^{R} *rodA::kan*^{R}*-P*$_{spac}$*-rodA*). For NA plate streaks and overnight cultures, 500 µM IPTG was added to media to allow expression of RodA. For imaging experiments, overnight cultures were washed 3 times in fresh media before resuspension in media and various IPTG concentrations.

Single-molecule MreB dynamics with various levels of RodA induction were measured using SM-VerCINI. RodA expression was induced with various levels of IPTG and 10 µM was found to produce the most similar measurements to WT (*mreB::mreB-HaloTag Δhag::erm*^{R}) (**Figure 5.3.B-D**).

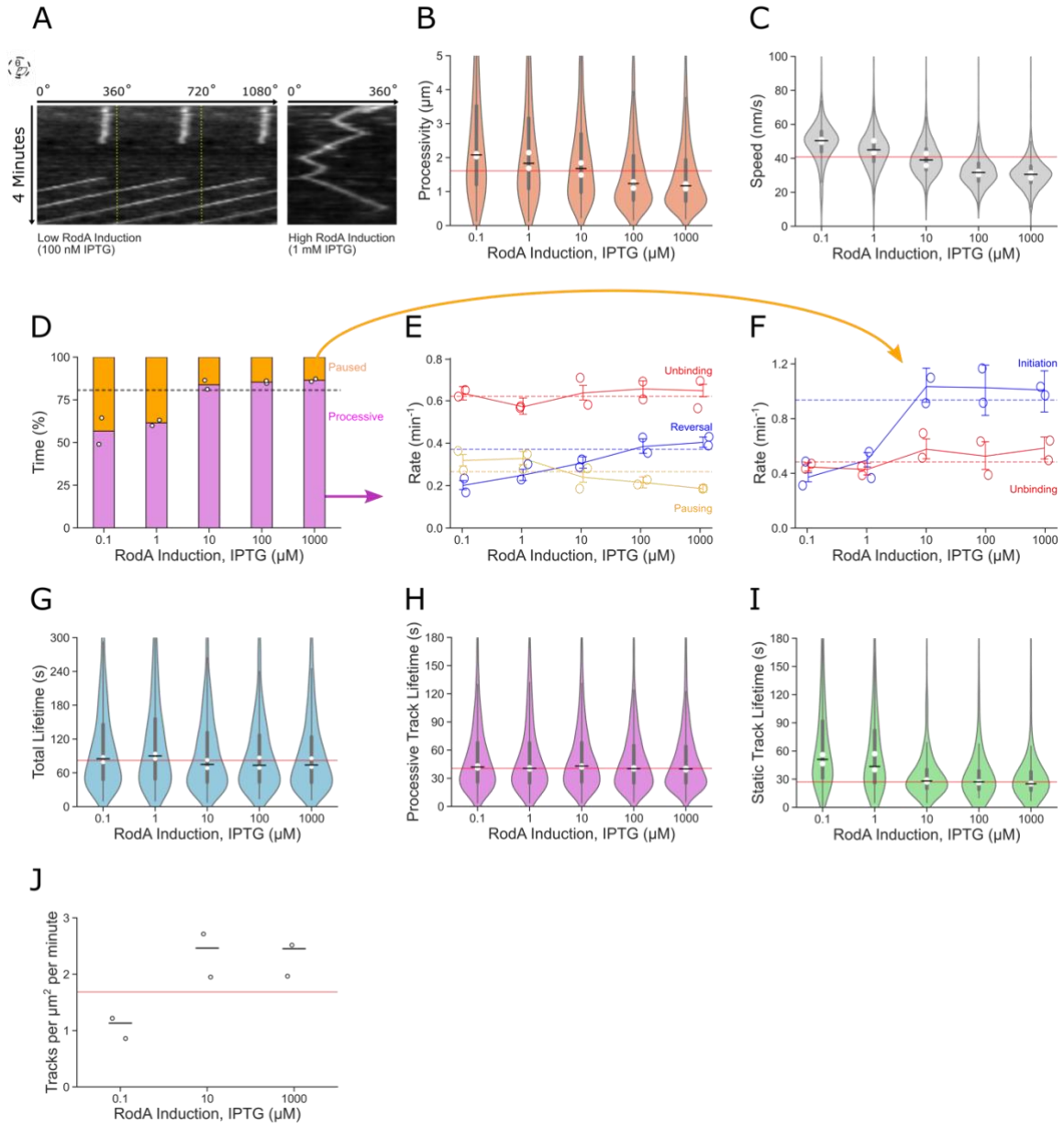

Figure 5.3. Effect of RodA induction levels on MreB dynamics. MreB-HaloTag (JF549) dynamics measured using SM-VerCINI in strain SM28 (*mreB::mreB-HaloTag Δhag::erm*^{R} *rodA::kan*^{R}*-P*$_{spac}$*-rodA*) over 8 minute time-lapse acquisitions with various concentrations of IPTG (**A-I**). **A.** Exemplar kymographs showing MreB-HaloTag (JF549) signal around the cell circumference over 4 minutes out of 8-minute time-lapse acquisitions in low (100 nM) and high (1mM) levels of IPTG dependent RodA induction. **B-C, G-I.** Violin plots showing lifetimes, processivity and speeds. White circles show medians of biological replicates, horizontal lines show overall median while vertical lines show IQR. Red lines show WT (*mreB::mreB-HaloTag Δhag::erm*^{R}) medians. **D-F.** Time in processive and static stated and rates of switching from

each state. Circles show biological replicate medians. Horizontal lines show WT (*mreB::mreB-HaloTag Δhag::erm^R*) medians. Error bars show 95% CI. **J.** Density of processive MreB-HaloTag (JF549) filaments in SM28 (*mreB::mreB-HaloTag Δhag::erm^R rodA::kan^R-P$_{spac}$-rodA*) under different RodA induction levels. Processive tracks were observed using SIM-TIRF microscopy over 1 minute time-lapse acquisitions and quantified using the TrackMate plugin in FIJI. Cell area was determined from brightfield images processed in Ilastik. The number of processive tracks observed in the 1 minute time-lapse was divided by cell area to calculate filament density detailed in **2.7.3- 2.7.4**. White circles show medians of biological replicates, horizontal lines show overall median. Red line shows WT (*mreB::mreB-HaloTag Δhag::erm^R*) median.

When RodA was depleted, processivity and speed of MreB increased. At 100 nM RodA induction levels, MreB processivity was a median of 2.08 µm [95% CI: 1.96, 2.18] with a median difference of 0.40 [95% CI: 0.26, 0.51] at a speed of 50.31 nm/s [95% CI: 49.83, 50.80] with a median difference of 11.31 [95% CI: 10.57, 12.04] relative to 10 µM expression levels **(Figure 5.3.B-C)**. As RodA expression was increased to 1 mM IPTG, speed decreased to 30.55 nm/s [95% CI: 30.21, 30.89] with a median difference of -8.45 [95% CI: -9.14, -7.79] compared to 10 µM induction levels, while processivity also decreased to a median of 1.17 µm [95% CI: 1.12, 1.22] with a median difference of -0.50 [95% CI: -0.59, -0.42] compared to 10 µM **(Figure 5.3.B-C)**. The changes in speed and processivity are apparent in exemplar kymographs **(Figure 5.3.A)**. Processive subtrack lifetime remained constant at around 40 s **(Figure 5.3.H)**.

The differences MreB dynamics between the highest and lowest induction levels are even more pronounced. A median difference in processivity of 0.91 µm [95% CI: 0.78, 1.02] was observed between the 100 nM and 1mM IPTG induction levels, which is a 1.78- fold increase from RodA OE to RodA depletion. A large difference in speed was also found between the two conditions. At highest levels of RodA induction, speed was found to decrease by a median difference of -19.76 nm/s [95% CI: -20.33, -19.13] when compared to the lowest expression levels, a 1.65-fold difference (**Table 5.2.2**).

Upon depletion of RodA, MreB spends much more time in a paused/static state. At 100 nM IPTG induction, MreB spends a median of 43.30 % of the time in a paused state **(Figure 5.3.D)**. As induction is increased, the fraction of static MreB decreases to 16.21 % at 10 µM IPTG induction levels, but only decreases to 15.55 % at 1 mM induction. Moreover, when RodA is

depleted at 100 nM induction, static track lifetime increases to 51.00 s [95% CI: 48.00, 55.50] with a median difference of 23.00 [95% CI: 19.99, 27.99] relative to 10 µM levels of induction, whereas once 10 µM induction is reached, static track lifetime remains relatively constant.

The switching rates between the processive and paused states also inform about the mechanism of MreB filament transport by the elongasome. At the lowest RodA induction level, MreB was found to pause more often and reverse less often, with median reversal and pausing rates 0.18 min^{-1} [95% CI: 0.16, 0.21] and 0.30 min^{-1} [95% CI: 0.28, 0.33] respectively. When RodA induction increased, reversals were more frequent and pauses infrequent. Unbinding rate remained moderately constant independent of RodA induction **(Figure 5.3.E)**. When MreB was in a paused state, at low RodA induction levels, (100 nM or 1 µM IPTG), synthesis initiation events were observed much less frequently, at a similar frequency to unbinding events, whereas when expression was increased to 10 µM and above, synthesis initiation events were observed at a similar frequency to 10 µM **(Figure 5.3.F)**. The total track and subtrack lifetimes were relatively unperturbed regardless of RodA expression **(Figure 5.3.G-H)**.

The change in MreB dynamics upon titration of RodA provide strong evidence of a tug-of-war mechanism of MreB filament transport. At increased RodA levels, more molecular motors are bound to the MreB filament participating in a tig-of-war to determine the direction of travel of the elongasome, characterised by the frequent reversals and low processivity of MreB subunits. The reduction in speed observed in this background is presumably owing to drag caused by the motor acting in the 'losing' direction. When RodA is depleted, MreB filaments have either 0 motor bound, which leads to the increased static lifetimes observed, or 1 motor bound, where the motor in the 'winning' direction is free to move at high speed for long processivities without other opposing motors bound. This model infers that processive MreB filament density increases when RodA expression increases.

To measure processive MreB filament density and provide further evidence of the model, MreB-HaloTag was densely labelled with 500 nM JF549 and observed using SIM-TIRF microscopy for 1 minute time-lapse acquisitions. Brightfield images of each FOV were taken to allow quantification of processive tracks per cell area. When RodA was depleted, processive filament density reduced to 1.13 tracks per μm^2 per minute. When overexpressed,

filament density was similar to density at 10 µM induction levels, with 2.45 processive tracks per μm^2 per minute **(Figure 5.3.J)**. These data concur with the model I propose, where at low RodA levels, there are fewer MreB filaments with bound RodA motors, driving processive motion. Moreover, at high RodA levels, a higher proportion of MreB filaments have at least one bound motor driving motion, increasing processive filament density.

Table 5.2.2. Medians and 95% CIs of MreB-HaloTag dynamics in SM28 (*mreB::mreB-HaloTag Δhag::erm^R rodA::kan^R-P$_{spac}$-rodA*) measured by SM-VerCINI shown in **Figure 5.3**. 2 biological replicates were conducted for this experiment. Median differences (Δ Median) and CIs on median differences are relative to 10 µM induction values, except for comparisons between 1 mM and 100 nM induction.

	n	Median	95% CI, low	95% CI, high	Δ Median	95% CI, low	95% CI, high
Paused Subtrack Lifetime (s)							
100 nM IPTG	1018	51.00	48.00	55.50	23.00	19.99	27.99
1 µM IPTG	670	43.5.0	40.25	46.99	15.50	12.62	20.00
10 µM IPTG	482	28.00	26.00	29.00			
100 µM IPTG	302	27.00	25.00	28.99	-0.99	-4.00	1.50
1 mM IPTG	495	25.00	24.00	27.00	-2.99	-5.00	0.00
Processivity (µm)							
100 nM IPTG	1696	2.08	1.96	2.18	0.40	0.263	0.51
1 µM IPTG	1286	1.83	1.73	1.92	0.15	0.03	0.27
10 µM IPTG	1669	1.68	1.61	1.73			
100 µM IPTG	1254	1.24	1.15	1.31	-0.44	-0.56	-0.35
1 mM IPTG	2351	1.17	1.12	1.22	-0.50	-0.59	-0.42
1mM- 100nM					-0.91	-1.02	-0.78
Speed (nm/s)							
100 nM IPTG	1696	50.31	49.83	50.80	11.31	10.57	12.04
1 µM IPTG	1286	44.97	44.25	45.57	5.974	5.05	6.86
10 µM IPTG	1669	39.00	38.41	39.53			
100 µM IPTG	1254	31.62	31.08	32.24	-7.38	-8.13	-6.56
1 mM IPTG	2351	30.55	30.21	30.89	-8.45	-9.14	-7.79
1mM- 100nM					-19.76	-20.33	-19.13
Time in Processive State (%)							
100 nM IPTG	2	56.7.0					
1 µM IPTG	2	61.49					
10 µM IPTG	2	83.79					
100 µM IPTG	2	85.36					
1 mM IPTG	2	86.45					

Reversals per minute (Rate^{-1})							
100 nM IPTG	1696	0.18	0.16	0.21			
1 µM IPTG	1286	0.23	0.21	0.26			
10 µM IPTG	1669	0.29	0.27	0.32			
100 µM IPTG	1254	0.37	0.34	0.41			
1 mM IPTG	2351	0.39	0.36	0.41			
1mM- 100nM					0.20	0.17	0.24
Pauses per minute (Rate^{-1})							
100 nM IPTG	1696	0.30	0.278	0.33			
1 µM IPTG	1286	0.31	0.28	0.35			
10 µM IPTG	1669	0.22	0.20	0.25			
100 µM IPTG	1254	0.20	0.17	0.23			
1 mM IPTG	2351	0.17	0.15	0.19			
1mM- 100nM					-0.13	-0.17	-0.10
Unbind After Processive per minute (Rate^{-1})							
100 nM IPTG	1696	0.62	0.59	0.65			
1 µM IPTG	1286	0.56	0.52	0.60			
10 µM IPTG	1669	0.62	0.59	0.66			
100 µM IPTG	1254	0.64	0.60	0.68			
1 mM IPTG	2351	0.63	0.60	0.66			
1mM- 100nM					0.01	-0.03	0.06
Initiation After Pause per minute (Rate^{-1})							
100 nM IPTG	1018	0.38	0.34	0.41			
1 µM IPTG	670	0.51	0.46	0.56			
10 µM IPTG	482	1.06	0.94	1.20			
100 µM IPTG	302	1.05	0.84	1.22			
1 mM IPTG	495	1.03	0.87	1.18			
1mM- 100nM					0.66	0.50	0.81
Unbind After Pause per minute (Rate^{-1})							
100 nM IPTG	1018	0.45	0.42	0.49			
1 µM IPTG	670	0.44	0.39	0.48			
10 µM IPTG	482	0.59	0.52	0.67			
100 µM IPTG	302	0.54	0.44	0.64			
1 mM IPTG	495	0.60	0.51	0.68			
1mM- 100nM					0.14	0.06	0.23

5.2.3 Effect of RodA expression on cell wall synthesis

It has previously been reported that non-native RodA expression levels increase cell diameter (Dion et al., 2019). To ensure the same effect was present under my conditions, Nile Red was used to membrane stain cells and measure morphology under different RodA induction levels in SM28 (*mreB::mreB-HaloTag Δhag::erm^R rodA::kan^R-P$_{spac}$-rodA*) **(Figure 5.4.A)**.

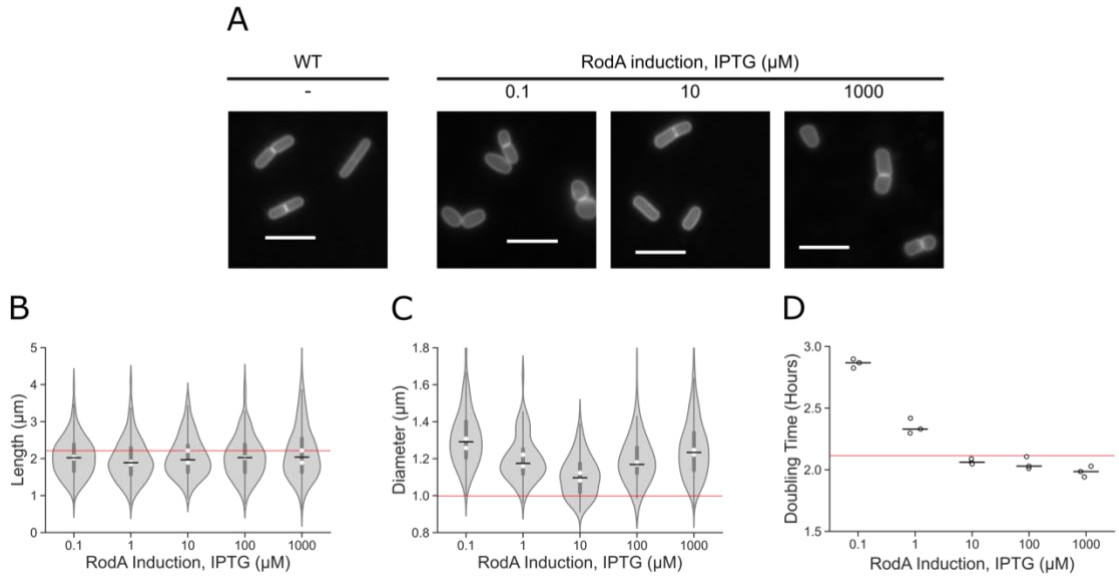

Figure 5.4. Effect of RodA induction levels on cell morphology and growth rate. **A.** Nile red membrane stain images of WT strain, SM01 (*mreB::mreB-HaloTag Δhag::erm*^{R}) and SM28 (*mreB::mreB-HaloTag Δhag::erm*^{R} *rodA::kan*^{R}*-P*$_{spac}$*-rodA*) under various RodA induction levels. Scale bar = 1 μm. **B-C.** Violin plots of cell length and diameter. (*mreB::mreB-HaloTag Δhag::erm*^{R}) medians. **D.** OD_{600} doubling time under various RodA induction levels. White circles show medians of biological replicates, horizontal lines show overall median while vertical lines show IQR. Red lines show WT (*mreB::mreB-HaloTag Δhag::erm*^{R}) median.

Cell length was found to be slightly shorter than WT in the strain, regardless of RodA induction **(Figure 5.4.B)**, and the same cell widening affect was seen when RodA was either depleted or overexpressed **(Figure 5.4.C)**. Though depletion and overexpression were found to have similar effects on cell morphology, they affected growth rate differently **(Figure 5.4.D)**. When RodA was depleted with 100 nM IPTG induction, growth rate slowed to a median doubling time of 2.87 hours. When RodA was overexpressed with 1 mM IPTG, growth rate increased to a median doubling time of 1.99 hours.

The differences in cell diameter observed could be a consequence of changes in processivity of the elongasome. I suggest that at low RodA expression levels, cell diameter increases because there are fewer actively synthesising, processive elongasomes. This means that there is a higher aPBP to elongasome peptidoglycan ratio resulting in a wider cell. When RodA is overexpressed, there are enough actively synthesising elongasomes, however the short

processivities caused by the RodA mediated tug-of-war, leads to shorter cylindrical peptidoglycan strands. The shorter strands have less strength than longer strands and exert less inward force against the cellular turgor pressure, leading to a wider cell.

Growth rate data suggest that when RodA is depleted, not enough elongasome peptidoglycan synthesis is taking place to maintain elongation and cell growth. When RodA is overexpressed, growth rate increases compared to 10 µM induction however, does not increase by a large magnitude, suggesting that growth rate is becoming limited by either aPBP peptidoglycan synthesis activity or a limited amount of other elongasome components. Also, once the MreB filaments in the cell are saturated with RodA, increases levels of RodA creates a surplus of non peptidoglycan synthesising RodA, not affecting growth rate. This suggests that RodA is not acting independently of the elongasome and contributing to aPBP mediated peptidoglycan synthesis.

Table 5.2.3. Medians and 95% Cis of cell diameter in SM28 (*mreB::mreB-HaloTag Δhag::erm^R rodA::kan^R-P$_{spac}$-rodA*) measured by SM-VerCINI shown in **Figure 5.4**. 2 biological replicates were conducted for this experiment. Median differences (Δ Median) and CIs on median differences are relative to 10 µM induction values.

	n	Median	95% CI, low	95% CI, high	Δ Median	95% CI, low	95% CI, high
Cell Diameter (µm)							
100 nM IPTG	215	1.29	1.27	1.32	0.19	0.17	0.23
1 µM IPTG	166	1.17	1.16	1.20	0.08	0.05	0.11
10 µM IPTG	243	1.10	1.08	1.12			
100 µM IPTG	160	1.67	1.16	1.90	0.07	0.05	0.10
1 mM IPTG	262	1.23	1.21	1.26	0.14	0.11	0.17

5.3 Discussion

In this chapter, elongasome associated peptidoglycan synthases were genetically or transcriptionally perturbed to explore their role in regulation of MreB and elongasome dynamics and subsequent cell shape.

When each of the elongasome associated transpeptidases were deleted, no substantial changes in MreB dynamics were observed. The MreB speed in *ΔpbpA* and *ΔpbpH* data presented here conflict with those previously reported (Domínguez-Escobar et al., 2011). I have conducted this experiment in two different strain backgrounds with different MreB fusion proteins and in different media. In previously reported data (Domínguez-Escobar et al., 2011), magnesium, which is known to compensate for many elongasome associated peptidoglycan defects (Tesson et al., 2022) was added to media, suggesting that the fusion protein used was not fully functional. Extra magnesium was not required in any of my experiments. Therefore, I conclude that transpeptidase deletions do not perturb MreB speed.

The MreB dynamics observed in *ΔpbpA* and *ΔpbpH* using SM-VerCINI did show some subtle but putative differences in dynamics, so to fully rule out that transpeptidases have a role in regulating MreB dynamics, a titration strain should be constructed to further reduce the copy number of transpeptidases in the cell. It is possible that when one of the transpeptidases are deleted, it is possible that the cell increases transcription of the other in order to compensate for the deletion.

The ability to titrate RodA expression levels gave great insight into the role of the protein in regulating elongasome dynamics. Changes in RodA levels perturbed MreB processivity and other dynamics. This provides strong evidence that elongasome dynamics are self-regulated by proteins within the complex itself. If dynamics were regulated by an extrinsic factor, such as a template track, processivity would remain constant, and any changes of speed should change subtrack lifetime.

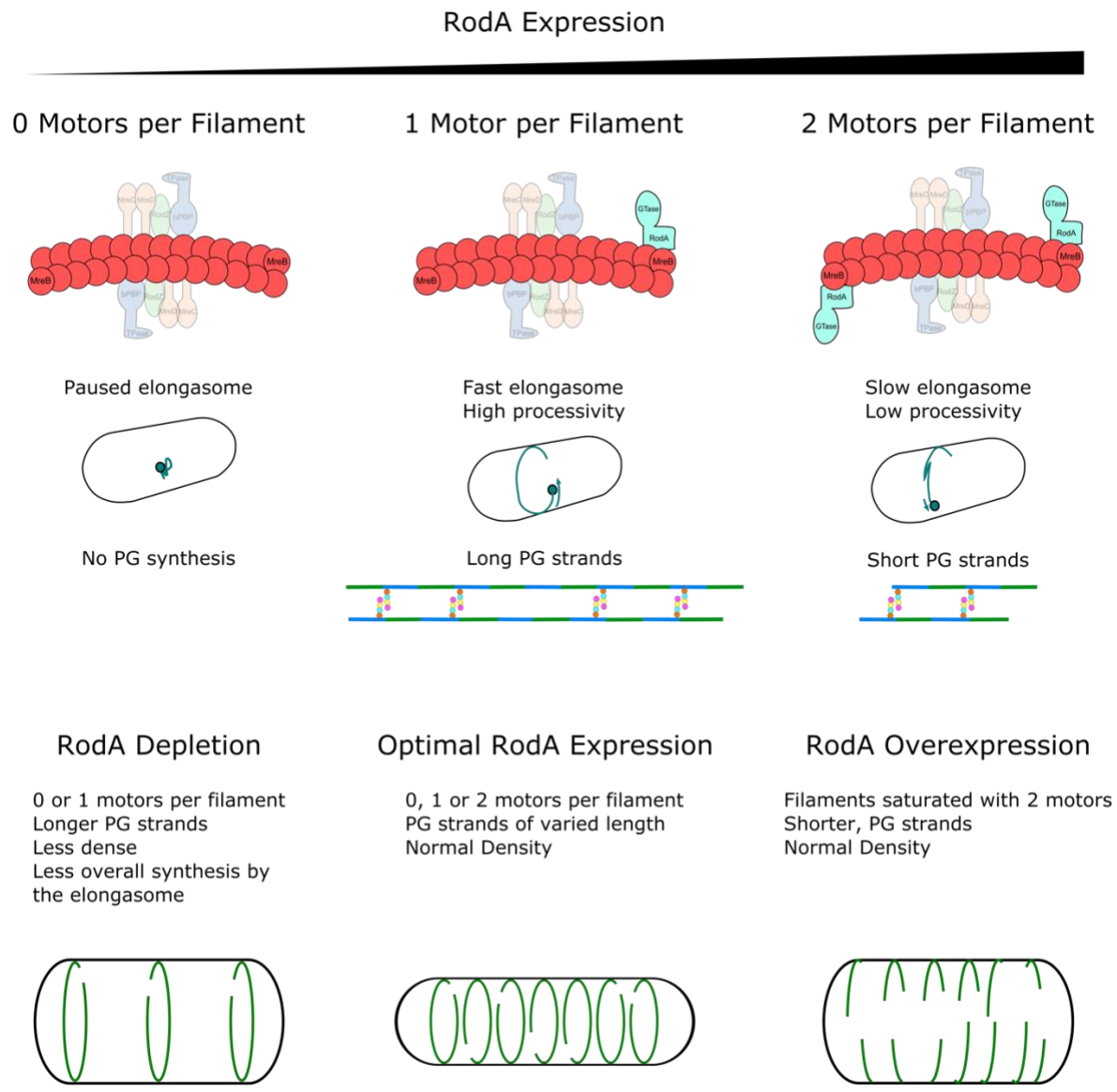

Figure 5.5. Low motor number RodA tug-of-war mechanism regulates elongasome dynamics to determine cell diameter.

At low RodA expression levels, MreB speed increased, as did processivity. However, when RodA levels were increased beyond WT levels, MreB slowed down and processivity was reduced. This was unexpected, as I predicted that MreB speed and processivity would increase with more RodA in the cell providing glycosyltransferase mediated driving force propelling the MreB filament further and faster.

The reduction in speed with RodA overexpression provides evidence of a tug-of-war model. With more RodA in the cell, the MreB filament is likely saturated with RodA, meaning only

around 50% of the subunits bound to the filament are active and driving MreB motion in one direction, while the others could be acting as an opposing force in the other direction and causing drag on the complex. The increase in processivity seen when RodA is depleted suggests that once one RodA is bound to the MreB filament and a whole elongasome is assembled, the complex is free to move processively, and with no other RodA acting in the opposing direction, the complex can move at greater speeds without drag opposing the motion.

The switching rate data also support the tug-of-war model but provide a great deal of refinement. The model proposed (Olshausen et al., 2013) states that multiple motors bind and unbind to the complex causing reversals and sometimes pauses. In this system, pausing should be more frequent at lower motor copy numbers, as it is more likely to have even numbers of motors acting in opposing directions. In addition, reversal rate should increase, as with a low number of motors on the complex, it is more likely that one extra motor binding will tip the balance of the complex and change direction. Also, as copy number is increased, reversals should be less frequent; as more motors are able to bind, it is less likely that even an even number of motors will bind and act in either direction. My data directly contradict this suggestion. As RodA, or motor, numbers are reduced, reversals are much less frequent, whereas when numbers are increased, reversals become more frequent. In light of these findings, I propose a novel model, whereby a low copy number tug-of-war mechanism to determine elongasome dynamics, where RodA acts as the molecular motors driving transport of the MreB filament by active glycosyltransferase activity and peptidoglycan synthesis **(Figure 5.5**). At low RodA levels, 0 or 1 motors are bound to the MreB filament; many filaments are left with no motors, in a paused state with no active peptidoglycan synthesis, while those with 1 motor are moving processively with no opposing force at high speeds resulting in longer peptidoglycan synthesis events. This results in fewer but longer cylindrical peptidoglycan synthesis events. I hypothesise that the reduction in overall elongasome mediated synthesis a wider cell because the aPBP to elongasome synthesis ratio described (Dion et al., 2019) is increased. When motor numbers are increased, MreB filaments are saturated with 2 motors. Here, filaments move more slowly and reverse more often, leading to lower processivity. Each motor is acting in an opposing direction and one of the motors 'wins' leading to MreB filament motion in that direction. How and why the motor wins could

be subject to the presence or absence of other elongasome components, or localised lipid II availability. The mechanism could be similar to that described in eukaryotes, where either one of the motors is stronger than the other, prompting one to win and direct filament transport (Welte, 2004). Alternatively, motors could be coordinated. MreCD has been found to coordinate interactions and activity between transpeptidases and RodA (Liu et al., 2020), so even though I propose RodA as the key regulator of elongasome dynamics, other elongasome components may be important in situations where 2 RodA motors are bound to a filament.

This in turn leads to a high density of elongasome mediated peptidoglycan synthesis events, but the events are shorter. This produces shorter cylindrical peptidoglycan hoops which have a weaker inward force acting against turgor pressure from within the cell. To produce optimal elongasome peptidoglycan synthesis to construct a narrow cell wall, the cell must populate as many MreB filaments as possible with RodA motors, allowing long and frequent synthesis, while ensuring as few filaments as possible are populated with 2 motors. In practice it is likely that a mixed population of MreB filaments with 0,1 or 2 bound motors contribute to synthesis of cylindrical peptidoglycan hoops with varying length.

The increase in cell diameter seen when RodA is depleted is consistent with previously reported data where a general reduction of peptidoglycan synthesis by the elongasome leads to an imbalance of aPBP and elongasome synthesised peptidoglycan producing a wider cell (Dion et al., 2019). More evidence is needed to provide a conclusive link between the overexpression of RodA and increased diameter. The increase in diameter observed is consistent with that seen previously (Dion et al., 2019), but the mechanism of how this occurs isn't conclusive.

Filament density data **(Figure 5.3.J)** reinforce that RodA depletion causes fewer processive synthesis events by the elongasome. However, more evidence is needed to conclusively show that changes in cell diameter under different RodA expression levels are because of changes in MreB processivity leading to structural changes in cylindrical peptidoglycan, and not by RodA acting independent of the elongasome as suggested (Dion et al., 2019).

To provide further evidence my proposed model, MreB dynamics should be measured in a background where the rest of the elongasome is overexpressed to provide more binding sites for RodA. This should reduce cell diameter and dynamics should return to WT levels by restoring the elongasome to RodA ratio which should produce optimal cylindrical peptidoglycan. In addition, if other elongasome are overexpressed with WT levels of RodA expression, this should result in fewer RodA motors available for each MreB filament, increasing processivity and speed and reducing reversal rate. Also, a subunit counting experiment would be useful to determine with certainty how many RodA molecules are bound to each MreB filament. If this model is accurate, no more than 2 should be observed.

In this chapter, I set out to identify any intrinsic regulators of elongasome dynamics. I identified that RodA, the elongasome associated glycosyltransferase, regulates dynamics of the complex *via* a low-copy number tug-of-war mechanism. The changes in elongasome dynamics, specifically processivity are associated with increased cell diameter. I propose that this is owing to differences in localised peptidoglycan construction causing different glycan lengths which in turn affect the cell thinning effect of the elongasome. In addition, it was found that neither PBP2A or PBPH alone have a substantial effect on elongasome dynamics.

Chapter 6: Discussion

At the outset of the project, I aimed to gain insight into the mechanism by which the MreB filament is transported by the elongasome and how this impacts peptidoglycan synthesis and cell shape. I developed an imaging protocol to allow observation of MreB subunits for extended time periods, without the limitation of existing techniques. With the use of SM-VerCINI combined with stroboscopic illumination, MreB subunits were tracked for 10-fold longer than was previously estimated as total track lifetime (Dersch et al., 2020). I tracked MreB subunits for a median total lifetime of 82 s, which is still a measurement constrained by photobleaching; when the effect of photobleaching was accounted for, total lifetime was calculated at a median of 128 s. Other minor limitations, such as tracks deviating away from the short axis of the cell moving out of the FOV likely have a minor impact on total lifetime measurements. The ability to track MreB for such long time periods allowed measurement of several key parameters of dynamics which were previously only possible by extrapolating data acquired with limited techniques (Dersch et al., 2020).

Processivity of MreB and the elongasome is a fundamental measurement in determining both the mechanism of MreB filament transport, and its subsequent effect on PG synthesis. Previous estimates of processivity were produced using TIRF microscopy (Dersch et al., 2020), which inherently truncates tracks with its limited field of illumination. This limitation means that maximum observable processivity of ~500 nm, whereas processivity was measured at a median of 1.6 µm using SM-VerCINI, and up to a median of 2.1 µm under some conditions. Some tracks were observed with a processivity of >5 µm. The processivities measured endorse the hypothesis that length of elongasome synthesised peptidoglycan strands is set by processivity of the complex. The processivities measured are in the same order of magnitude as glycan strand lengths measured by AFM (Hayhurst et al., 2008). These measurements alone do not shed light on whether processivity is set by PG strand length or strand length sets processivity.

Switching rates between processive and paused states were analysed to gain more insight into the mechanism of MreB filament transport. Dynamics such as reversals and pauses have been observed previously (Billaudeau et al., 2017; Olshausen et al., 2013). Again, the ability to observe MreB subunits for such long timescales with the use of SM-VerCINI has allowed

observation of the frequency of these events. More than half of tracks observed displayed were found to undergo state switching, in comparison to <2% of tracks previously quantified (Billaudeau et al., 2017). The high frequency at which MreB was found to display reversal and pausing dynamics suggest a tug-of-war model with multiple filament transport motors acting in opposing directions are battling to direct motion (Olshausen et al., 2013). Until now, evidence of the tug-of-war model was still inconclusive. State switching could also be explained by possible collisions between filaments, although this is disputed as filaments are observed to reverse without other filaments nearby (Reimold et al., 2013). Collisions with landmarks within the cell wall could be the cause of reversals and pauses. In addition, MreB filament density data suggest that only one peptidoglycan strand is synthesised per MreB filament (Billaudeau et al., 2019), refuting the suggestion that multiple active peptidoglycan synthase motors are bound to the filament at once.

With a robust method developed to observe complex MreB subunit dynamics, I set about determining how dynamics are regulated and what this could reveal about how the elongasome adapts to different conditions. The first and most crude variable changed was growth rate by culturing cells in different growth media. MreB filament density has been found to vary dependent on growth rate (Sun and Garner, 2022), but changes in density were not severe enough to fully explain the changes in growth rate observed. Using SM-VerCINI, a small decrease in processivity was found as growth rate increased, while a subtle increase in speed was observed. The data suggest that MreB dynamics are affected by growth media, though the changes observed insufficient to account for the corresponding change in growth rate. Minor changes in speed and processivity likely act in combination with changes in elongasome density (Sun and Garner, 2022) to modulate growth rate. Further work could be carried out to calculate if the cumulative effect of dynamics and filament density are sufficient to account for the changes in growth rate.

I deleted *mltG* and observed the effect of the knockout on MreB dynamics with the rationale that this would produce longer glycan strands in the cell wall, with the absence of the glycan terminase to truncate glycan polymerisation. When *mltG* was deleted, little effect on MreB dynamics was found. It has subsequently been found that MltG does not affect glycan strand length within the sacculus, rather produces shorter glycans for an unknown cellular process (Sassine et al., 2021).

Because active peptidoglycan synthesis is essential for MreB motion (Domínguez-Escobar et al., 2011; Garner et al., 2011; van Teeffelen et al., 2011), I tested the effect of the three known elongasome associated peptidoglycan synthases, PBP2A, PBPH and RodA on MreB dynamics using SM-VerCINI. Single deletions of *pbpA* (encodes PBP2A) and *pbpH* were found to have a negligible effect on MreB dynamics. The two genes are functionally redundant (Kobayashi et al., 2003) so it is likely that when one is deleted, the other is sufficient to maintain WT-like elongasome function. Moreover, in *E. coli*, ~80% of the elongasome associated bPBP, PBP2, has been in a diffusive, inactive state (Özbaykal et al., 2020). This suggests a surplus of bPBP in the cell, so a more drastic reduction in bPBP may be required to fully elucidate the effect of elongasome transpeptidases on MreB dynamics. Construction of a depletion strain, where one of the transpeptidases is knocked out and the other under an inducible promoter would be useful to titrate the amount of bPBP available to the elongasome and determine how this affects MreB dynamics.

RodA is the other peptidoglycan synthase associated with the elongasome, providing glycosyltransferase activity, polymerising glycan strands (Cho et al., 2016; Emami et al., 2017). Single-molecule MreB dynamics were measured with various RodA expression levels using SM-VerCINI. When RodA was depleted, MreB processivity and speed increased. In the depletion experiments, pausing rate increased, whereas reversal rate decreased. When RodA was overexpressed, MreB processivity and speed decreased. When RodA was overexpressed, reversals were seen more frequently, while pauses were less frequently observed. The data provide strong evidence that a tug-of-war model modulates MreB filament transport, but not a multiple motor system that has been previously proposed (Olshausen et al., 2013). Rather, my data suggest a low motor number tug-of-war by RodA is the regulator of MreB dynamics (**Figure 5.5**).

The model I propose is that the MreB filament, which in actuality is an antiparallel double filament (van den Ent et al., 2014), can be populated with either 0, 1 or 2 RodA motors at once, a RodA binding site at each end. When RodA is overexpressed, MreB filaments predominantly have 2 RodA motors bound. In the tug-of-war, one RodA wins and determines the direction of travel of the filament. This motion is slowed, owing to drag of the other RodA motor acting in the opposing direction. Processive subtrack lifetime is consistent, regardless of RodA expression, so the reduction in speed causes reduced processivity. Because each end

of the filament has a RodA bound and primed to initiate synthesis, the filament is more likely to reverse than pause, which is reflected in my switching rate data. When RodA levels are depleted, most MreB filaments have either 0 or 1 RodA bound. In this scenario, the elongasome is free to synthesis peptidoglycan and move at high speed without the hindrance of another RodA acting in the opposing direction. With a constant processive subtrack lifetime, the increase in speed causes higher processivity. At the end of a processive track, a pause is more likely as there is no second RodA primed to initiate synthesis in the opposite direction. The model suggests that only one glycan strand is inserted into the existing sacculus at once with one active RodA per MreB filament. This is supported by previous filament density data and calculations that only one PG strand is synthesised per each MreB filament (Billaudeau et al., 2019).

In the 0, 1 or 2 synthase model, I suggest that one RodA could bind at each end of the MreB antiparallel double filament. Because MreB forms an antiparallel double filament, it is conceivable that RodA has a binding site at either the plus or minus end of one filament. Alternatively, other elongasome proteins like RodA or MreCD could have binding sites at each end of the filament, which could then ensure a RodA synthase to bind the MreB filament at each end. In either scenario, this could orient each RodA synthase in opposing directions, providing motors able to drive MreB dynamics in each direction. The RodA synthesis motor then would drive the whole elongasome in the direction in which it is oriented, presumably because RodA orientation allows access of the glycosyltransferase to the peptidoglycan precursor, lipid II. The process of binding lipid II and insertion into the existing peptidoglycan, and further binding of lipid II by a transpeptidase in the elongasome drives the whole elongasome forward in the direction of peptidoglycan synthesis.

The binding kinetics of other elongasome proteins is yet to be determined beyond the RodA data presented in this work. It is possible that the elongasome assembles and remains so for the duration of a whole MreB track or subtrack. Alternatively, binding and unbinding of proteins like RodZ or the transpeptidases could occur so frequently as to provide peptidoglycan synthesis allowing MreB to move continuously for the duration of a processive subtrack. Also, as elongasome dynamics are dependent on peptidoglycan synthesis, there must be enough lipid II accessible to RodA to allow continuous peptidoglycan synthesis to maintain the high processivities reported in this work.

Further to the work presented in this thesis, unpublished simulations conducted by Séamus Holden show the model to be viable. The simulations show that within a multiple motor tug-of-war, as the number of motors increases, reversal rate substantially decreases and processivity increases. When the simulations are constrained to a maximum of 2 motors per filament, extended pauses were found at low motor numbers, reversal rate increased, reducing processivity as motor numbers increased. The results from simulations are consistent with observations *in vivo* upon titration of RodA (**Figure 5.3**).

Consistent with previously published data (Dion et al., 2019), cell diameter was found to increase under both RodA depletion and overexpression. I speculate that when RodA is depleted, some MreB filaments have one bound RodA and move at high speed synthesising long peptidoglycan strands, while many filaments have no RodA bound and therefore cannot synthesise peptidoglycan. This leads to an imbalance between the two elongation mechanisms where there is more disordered, non-circumferential peptidoglycan synthesised by aPBPs relative to the ordered, circumferential peptidoglycan synthesised by the elongasome. In contrast, when RodA is overexpressed, most MreB filaments are populated with 2 RodA motors, which actively synthesise PG. In this scenario, because of the low processivity of the elongasome, cylindrical peptidoglycan strands are shorter, providing less inward force acting against the turgor pressure of the cell. Under optimal RodA expression levels, enough of the MreB filaments have at least one RodA bound to provide a high enough density of actively peptidoglycan synthesising elongasomes to maintain equilibrium with aPBP synthesised peptidoglycan, while not too many of the filaments have 2 RodA monomers bound as to reduce processivity and subsequent glycan strand length.

To provide further evidence of this model, MreB filament density was measured under RodA depletion and overexpression using SIM-TIRF. I found that indeed, when RodA was depleted, the density of processive MreB filaments reduced, providing further support that RodA depletion increases cell diameter because of a reduction in overall elongasome associated peptidoglycan synthesis. When RodA was overexpressed with 1 mM IPTG, processive filament density increased relative to RodA depletion but did not increase relative to 10 µM IPTG RodA expression, which was the closest induction to WT identified. While this finding does is consistent with the suggestion that higher levels of RodA cause shorter processivity and the

shorter subsequent glycan strands increase cell diameter, further experimentation is required to provide more conclusive evidence.

An experiment where single-molecule MreB dynamics are measured with the overexpression of MreBCD alongside the overexpression of RodA would provide further evidence that changes in elongasome dynamics drive changes in cell diameter. The overexpression of other elongasome components should provide more filaments for the extra RodA to bind and recover cell shape and MreB processivity to normal levels. Osmotic shock experiments could be carried out as in previous studies (Dion et al., 2019) to compare the anisotropy of cells under RodA depletion and overexpression. I predict that the shorter glycans suggested in an overexpression background will give cells a different anisotropy than those with the longer glycans predicted in the depletion background. A molecular counting experiment could also be carried out where RodA is labelled with a fluorescent protein and photobleached using widefield microscopy. The MreB filament is typically shorter than the diffraction limit (Billaudeau et al., 2019), so the number of bleaching steps should correspond to the number of RodA monomers bound to the filament. This should show either 1 or 2 RodA monomers per MreB filament.

Since the first discoveries in 2011 that MreB forms dynamic filaments that move around the cell circumference driven by peptidoglycan synthesis (Domínguez-Escobar et al., 2011; Garner et al., 2011; van Teeffelen et al., 2011), various microscopy based techniques have been used to further understanding of the regulation of dynamics and their impact on peptidoglycan synthesis. The development of SM-VerCINI has been pivotal in allowing more complex analysis of elongasome dynamics to reveal the mechanism of MreB filament transport and its subsequent role in cell shape homeostasis I propose in this thesis.

In future research, it would be interesting to explore the effect of other elongasome components on MreB dynamics. Because MreCD have been identified as regulators of peptidoglycan synthases in the elongasome (Liu et al., 2020), it is possible that they too have a role in regulation of elongasome dynamics by affecting peptidoglycan synthesis. The structure of the peptidoglycan sacculus in *E. coli* differs from that of *B. subtills* in several characteristics. Interestingly, glycan strands are significantly shorter in *E. coli* (Hayhurst et al., 2008; Turner et al., 2018).

To conclude, a novel SM-VerCINI method was developed to allow observation of MreB dynamics for longer time scales than ever before which has allowed in depth exploration into the mechanism of filament transport and the effect of dynamics on cell shape. The data presented shows that the elongasome associated glycosylase, RodA, mediates a low motor number molecular tug-of-war to tune processivity of the elongasome which in turn governs length of cylindrical peptidoglycan and subsequent cell shape. This mode of cargo transport has been proposed for multiple systems in eukaryotes, but to my knowledge, this is the first time such a mechanism has been conclusively shown in prokaryotes.

Chapter 7: References

Alyahya, S.A., Alexander, R., Costa, T., Henriques, A.O., Emonet, T., Jacobs-Wagner, C., 2009. RodZ, a component of the bacterial core morphogenic apparatus. Proc. Natl. Acad. Sci. U.S.A. 106, 1239–1244. https://doi.org/10.1073/pnas.0810794106

Atrih, A., Bacher, G., Allmaier, G., Williamson, M.P., Foster, S.J., 1999. Analysis of Peptidoglycan Structure from Vegetative Cells of Bacillus subtilis 168 and Role of PBP 5 in Peptidoglycan Maturation. J Bacteriol 181, 3956–3966.

Berg, S., Kutra, D., Kroeger, T., Straehle, C.N., Kausler, B.X., Haubold, C., Schiegg, M., Ales, J., Beier, T., Rudy, M., Eren, K., Cervantes, J.I., Xu, B., Beuttenmueller, F., Wolny, A., Zhang, C., Koethe, U., Hamprecht, F.A., Kreshuk, A., 2019. ilastik: interactive machine learning for (bio)image analysis. Nat Methods 16, 1226–1232. https://doi.org/10.1038/s41592-019-0582-9

Billaudeau, C., Chastanet, A., Yao, Z., Cornilleau, C., Mirouze, N., Fromion, V., Carballido-López, R., 2017. Contrasting mechanisms of growth in two model rod-shaped bacteria. Nat Commun 8, 15370. https://doi.org/10.1038/ncomms15370

Billaudeau, C., Yao, Z., Cornilleau, C., Carballido-López, R., Chastanet, A., 2019. MreB Forms Subdiffraction Nanofilaments during Active Growth in Bacillus subtilis. mBio 10, e01879-18. https://doi.org/10.1128/mBio.01879-18

Bisson-Filho, A.W., Hsu, Y.-P., Squyres, G.R., Kuru, E., Wu, F., Jukes, C., Sun, Y., Dekker, C., Holden, S., VanNieuwenhze, M.S., Brun, Y.V., Garner, E.C., 2017. Treadmilling by FtsZ filaments drives peptidoglycan synthesis and bacterial cell division. Science 355, 739–743. https://doi.org/10.1126/science.aak9973

Bork, P., Sander, C., Valencia, A., 1992. An ATPase domain common to prokaryotic cell cycle proteins, sugar kinases, actin, and hsp70 heat shock proteins. Proc. Natl. Acad. Sci. U.S.A. 89, 7290–7294.

Bouhss, A., Trunkfield, A.E., Bugg, T.D.H., Mengin-Lecreulx, D., 2008. The biosynthesis of peptidoglycan lipid-linked intermediates. FEMS Microbiol. Rev. 32, 208–233. https://doi.org/10.1111/j.1574-6976.2007.00089.x

Cabeen, M.T., Jacobs-Wagner, C., 2005. Bacterial cell shape. Nature Reviews Microbiology 3, 601–610. https://doi.org/10.1038/nrmicro1205

Carballido-López, R., Errington, J., 2003. The bacterial cytoskeleton: in vivo dynamics of the actin-like protein Mbl of Bacillus subtilis. Dev. Cell 4, 19–28.

Carballido-López, R., Formstone, A., Li, Y., Ehrlich, S.D., Noirot, P., Errington, J., 2006. Actin Homolog MreBH Governs Cell Morphogenesis by Localization of the Cell Wall Hydrolase LytE. Developmental Cell 11, 399–409. https://doi.org/10.1016/j.devcel.2006.07.017

Cho, H., Wivagg, C.N., Kapoor, M., Barry, Z., Rohs, P.D.A., Suh, H., Marto, J.A., Garner, E.C., Bernhardt, T.G., 2016. Bacterial cell wall biogenesis is mediated by SEDS and PBP polymerase families functioning semi-autonomously. Nat Microbiol 1, 16172. https://doi.org/10.1038/nmicrobiol.2016.172

Cleverley, R.M., Rutter, Z.J., Rismondo, J., Corona, F., Tsui, H.-C.T., Alatawi, F.A., Daniel, R.A., Halbedel, S., Massidda, O., Winkler, M.E., Lewis, R.J., 2019. The cell cycle regulator GpsB functions as cytosolic adaptor for multiple cell wall enzymes. Nat Commun 10. https://doi.org/10.1038/s41467-018-08056-2

Colavin, A., Shi, H., Huang, K.C., 2018. RodZ modulates geometric localization of the bacterial actin MreB to regulate cell shape. Nature Communications 9, 1280. https://doi.org/10.1038/s41467-018-03633-x

Cosgrove, D.J., 2005. Growth of the plant cell wall. Nat Rev Mol Cell Biol 6, 850–861. https://doi.org/10.1038/nrm1746

Cumming, G., Calin-Jageman, R., 2016. Introduction to the New Statistics: Estimation, Open Science, and Beyond. Routledge, New York. https://doi.org/10.4324/9781315708607

Dajkovic, A., Tesson, B., Chauhan, S., Courtin, P., Keary, R., Flores, P., Marlière, C., Filipe, S.R., Chapot-Chartier, M.-P., Carballido-Lopez, R., 2017. Hydrolysis of peptidoglycan is modulated by amidation of meso-diaminopimelic acid and Mg2+ in Bacillus subtilis. Molecular Microbiology 104, 972–988. https://doi.org/10.1111/mmi.13673

Daniel, R.A., Errington, J., 2003. Control of cell morphogenesis in bacteria: two distinct ways to make a rod-shaped cell. Cell 113, 767–776.

de Jong, I.G., Beilharz, K., Kuipers, O.P., Veening, J.-W., 2011. Live Cell Imaging of Bacillus subtilis and Streptococcus pneumoniae using Automated Time-lapse Microscopy. J Vis Exp 3145. https://doi.org/10.3791/3145

Defeu Soufo, H.J., Graumann, P.L., 2004. Dynamic movement of actin-like proteins within bacterial cells. EMBO Rep. 5, 789–794. https://doi.org/10.1038/sj.embor.7400209

Dersch, S., Mehl, J., Stuckenschneider, L., Mayer, B., Roth, J., Rohrbach, A., Graumann, P.L., 2020. Super-Resolution Microscopy and Single-Molecule Tracking Reveal Distinct Adaptive Dynamics of MreB and of Cell Wall-Synthesis Enzymes. Frontiers in Microbiology 11.

Dion, M.F., Kapoor, M., Sun, Y., Wilson, S., Ryan, J., Vigouroux, A., van Teeffelen, S., Oldenbourg, R., Garner, E.C., 2019. Bacillus subtilis cell diameter is determined by the opposing actions of two distinct cell wall synthetic systems. Nat Microbiol 4, 1294–1305. https://doi.org/10.1038/s41564-019-0439-0

Doi, M., Wachi, M., Ishino, F., Tomioka, S., Ito, M., Sakagami, Y., Suzuki, A., Matsuhashi, M., 1988. Determinations of the DNA sequence of the mreB gene and of the gene products of the mre region that function in formation of the rod shape of Escherichia coli cells. J Bacteriol 170, 4619–4624.

Domínguez-Escobar, J., Chastanet, A., Crevenna, A.H., Fromion, V., Wedlich-Söldner, R., Carballido-López, R., 2011. Processive movement of MreB-associated cell wall biosynthetic complexes in bacteria. Science 333, 225–228. https://doi.org/10.1126/science.1203466

Dörr, T., Moynihan, P.J., Mayer, C., 2019. Editorial: Bacterial Cell Wall Structure and Dynamics. Frontiers in Microbiology 10.

Edelstein, A.D., Tsuchida, M.A., Amodaj, N., Pinkard, H., Vale, R.D., Stuurman, N., 2014. Advanced methods of microscope control using μManager software. Journal of Biological Methods 1, e10–e10. https://doi.org/10.14440/jbm.2014.36

Efron, B., 1979. Bootstrap Methods: Another Look at the Jackknife. The Annals of Statistics 7, 1–26. https://doi.org/10.1214/aos/1176344552

Egan Alexander J. F., Biboy Jacob, van't Veer Inge, Breukink Eefjan, Vollmer Waldemar, 2015. Activities and regulation of peptidoglycan synthases. Philosophical Transactions of the Royal Society B: Biological Sciences 370, 20150031. https://doi.org/10.1098/rstb.2015.0031

Emami, K., Guyet, A., Kawai, Y., Devi, J., Wu, L.J., Allenby, N., Daniel, R.A., Errington, J., 2017. RodA as the missing glycosyltransferase in Bacillus subtilis and antibiotic discovery for the peptidoglycan polymerase pathway. Nat Microbiol 2, 16253. https://doi.org/10.1038/nmicrobiol.2016.253

Ent, F. van den, Amos, L.A., Löwe, J., 2001. Prokaryotic origin of the actin cytoskeleton. Nature 413, 39. https://doi.org/10.1038/35092500

Errington, J., 2015. Bacterial morphogenesis and the enigmatic MreB helix. Nature Reviews Microbiology 13, 241–248. https://doi.org/10.1038/nrmicro3398

Figge, R.M., Divakaruni, A.V., Gober, J.W., 2004. MreB, the cell shape-determining bacterial actin homologue, co-ordinates cell wall morphogenesis in Caulobacter crescentus. Molecular Microbiology 51, 1321–1332. https://doi.org/10.1111/j.1365-2958.2003.03936.x

Flärdh, K., 2003. Growth polarity and cell division in Streptomyces. Curr Opin Microbiol 6, 564–571. https://doi.org/10.1016/j.mib.2003.10.011

Formstone, A., Errington, J., 2005. A magnesium-dependent mreB null mutant: implications for the role of mreB in Bacillus subtilis. Mol. Microbiol. 55, 1646–1657. https://doi.org/10.1111/j.1365-2958.2005.04506.x

Foulquier, E., Pompeo, F., Bernadac, A., Espinosa, L., Galinier, A., 2011. The YvcK protein is required for morphogenesis via localization of PBP1 under gluconeogenic growth conditions in Bacillus subtilis. Mol. Microbiol. 80, 309–318. https://doi.org/10.1111/j.1365-2958.2011.07587.x

Galinier, A., Foulquier, E., Pompeo, F., 2021. Metabolic Control of Cell Elongation and Cell Division in Bacillus subtilis. Front Microbiol 12, 697930. https://doi.org/10.3389/fmicb.2021.697930

Garner, E.C., Bernard, R., Wang, W., Zhuang, X., Rudner, D.Z., Mitchison, T., 2011. Coupled, circumferential motions of the cell wall synthesis machinery and MreB filaments in B. subtilis. Science 333, 222–225. https://doi.org/10.1126/science.1203285

Gebhardt, J.C.M., Suter, D.M., Roy, R., Zhao, Z.W., Chapman, A.R., Basu, S., Maniatis, T., Xie, X.S., 2013. Single Molecule Imaging of Transcription Factor Binding to DNA in Live Mammalian Cells. Nat Methods 10, 421–426. https://doi.org/10.1038/nmeth.2411

Glauner, B., 1988. Separation and quantification of muropeptides with high-performance liquid chromatography. Anal. Biochem. 172, 451–464.

Glauner, B., Höltje, J.V., Schwarz, U., 1988. The composition of the murein of Escherichia coli. J. Biol. Chem. 263, 10088–10095.

Grimm, J.B., English, B.P., Chen, J., Slaughter, J.P., Zhang, Z., Revyakin, A., Patel, R., Macklin, J.J., Normanno, D., Singer, R.H., Lionnet, T., Lavis, L.D., 2015. A general method to improve fluorophores for live-cell and single-molecule microscopy. Nat Methods 12, 244–250, 3 p following 250. https://doi.org/10.1038/nmeth.3256

Gurtovenko, A.A., Anwar, J., 2007. Modulating the structure and properties of cell membranes: the molecular mechanism of action of dimethyl sulfoxide. J Phys Chem B 111, 10453–10460. https://doi.org/10.1021/jp073113e

Hamze, K., Julkowska, D., Autret, S., Hinc, K., Nagorska, K., Sekowska, A., Holland, I.B., Séror, S.J., 2009. Identification of genes required for different stages of dendritic swarming in Bacillus subtilis, with a novel role for phrC. Microbiology (Reading) 155, 398–412. https://doi.org/10.1099/mic.0.021477-0

Harz, H., Burgdorf, K., Höltje, J.-V., 1990. Isolation and separation of the glycan strands from murein of Escherichia coli by reversed-phase high-performance liquid chromatography. Analytical Biochemistry 190, 120–128. https://doi.org/10.1016/0003-2697(90)90144-X

Hayhurst, E.J., Kailas, L., Hobbs, J.K., Foster, S.J., 2008. Cell wall peptidoglycan architecture in Bacillus subtilis. Proc Natl Acad Sci U S A 105, 14603–14608. https://doi.org/10.1073/pnas.0804138105

Heidrich, C., Templin, M.F., Ursinus, A., Merdanovic, M., Berger, J., Schwarz, H., de Pedro, M.A., Höltje, J.V., 2001. Involvement of N-acetylmuramyl-L-alanine amidases in cell separation and antibiotic-induced autolysis of Escherichia coli. Mol. Microbiol. 41, 167–178.

Heijenoort, J. van, Gutmann, L., 2000. Correlation between the structure of the bacterial peptidoglycan monomer unit, the specificity of transpeptidation, and susceptibility to β-lactams. PNAS 97, 5028–5030. https://doi.org/10.1073/pnas.97.10.5028

Ho, J., Tumkaya, T., Aryal, S., Choi, H., Claridge-Chang, A., 2019. Moving beyond P values: data analysis with estimation graphics. Nat Methods 16, 565–566. https://doi.org/10.1038/s41592-019-0470-3

Höltje, J.-V., 1998. Growth of the Stress-Bearing and Shape-Maintaining Murein Sacculus of Escherichia coli. Microbiol Mol Biol Rev 62, 181–203.

Höltje, J.V., Mirelman, D., Sharon, N., Schwarz, U., 1975. Novel type of murein transglycosylase in Escherichia coli. Journal of Bacteriology 124, 1067–1076.

Houston, K., Tucker, M.R., Chowdhury, J., Shirley, N., Little, A., 2016. The Plant Cell Wall: A Complex and Dynamic Structure As Revealed by the Responses of Genes under Stress Conditions. Frontiers in Plant Science 7.

Hussain, S., Wivagg, C.N., Szwedziak, P., Wong, F., Schaefer, K., Izoré, T., Renner, L.D., Holmes, M.J., Sun, Y., Bisson-Filho, A.W., Walker, S., Amir, A., Löwe, J., Garner, E.C., 2018. MreB filaments align along greatest principal membrane curvature to orient cell wall synthesis. eLife 7, e32471. https://doi.org/10.7554/eLife.32471

Jalili, N., Laxminarayana, K., 2004. A review of atomic force microscopy imaging systems: application to molecular metrology and biological sciences. Mechatronics 14, 907–945. https://doi.org/10.1016/j.mechatronics.2004.04.005

Johnson, J.W., Fisher, J.F., Mobashery, S., 2013. Bacterial cell-wall recycling. Ann. N. Y. Acad. Sci. 1277, 54–75. https://doi.org/10.1111/j.1749-6632.2012.06813.x

Jones, L.J., Carballido-López, R., Errington, J., 2001. Control of cell shape in bacteria: helical, actin-like filaments in Bacillus subtilis. Cell 104, 913–922. https://doi.org/10.1016/s0092-8674(01)00287-2

Kandler, O., König, H., 1998. Cell wall polymers in Archaea (Archaebacteria). CMLS, Cell. Mol. Life Sci. 54, 305–308. https://doi.org/10.1007/s000180050156

Kawai, Y., Daniel, R.A., Errington, J., 2009. Regulation of cell wall morphogenesis in Bacillus subtilis by recruitment of PBP1 to the MreB helix. Mol. Microbiol. 71, 1131–1144. https://doi.org/10.1111/j.1365-2958.2009.06601.x

Kawai, Y., Mercier, R., Errington, J., 2014. Bacterial Cell Morphogenesis Does Not Require a Preexisting Template Structure. Current Biology 24, 863–867. https://doi.org/10.1016/j.cub.2014.02.053

Klingl, A., Pickl, C., Flechsler, J., 2019. Archaeal Cell Walls. Subcell Biochem 92, 471–493. https://doi.org/10.1007/978-3-030-18768-2_14

Kobayashi, K., Ehrlich, S.D., Albertini, A., Amati, G., Andersen, K.K., Arnaud, M., Asai, K., Ashikaga, S., Aymerich, S., Bessieres, P., Boland, F., Brignell, S.C., Bron, S., Bunai, K.,

Chapuis, J., Christiansen, L.C., Danchin, A., Débarbouille, M., Dervyn, E., Deuerling, E., Devine, K., Devine, S.K., Dreesen, O., Errington, J., Fillinger, S., Foster, S.J., Fujita, Y., Galizzi, A., Gardan, R., Eschevins, C., Fukushima, T., Haga, K., Harwood, C.R., Hecker, M., Hosoya, D., Hullo, M.F., Kakeshita, H., Karamata, D., Kasahara, Y., Kawamura, F., Koga, K., Koski, P., Kuwana, R., Imamura, D., Ishimaru, M., Ishikawa, S., Ishio, I., Le Coq, D., Masson, A., Mauël, C., Meima, R., Mellado, R.P., Moir, A., Moriya, S., Nagakawa, E., Nanamiya, H., Nakai, S., Nygaard, P., Ogura, M., Ohanan, T., O'Reilly, M., O'Rourke, M., Pragai, Z., Pooley, H.M., Rapoport, G., Rawlins, J.P., Rivas, L.A., Rivolta, C., Sadaie, A., Sadaie, Y., Sarvas, M., Sato, T., Saxild, H.H., Scanlan, E., Schumann, W., Seegers, J.F.M.L., Sekiguchi, J., Sekowska, A., Séror, S.J., Simon, M., Stragier, P., Studer, R., Takamatsu, H., Tanaka, T., Takeuchi, M., Thomaides, H.B., Vagner, V., van Dijl, J.M., Watabe, K., Wipat, A., Yamamoto, H., Yamamoto, M., Yamamoto, Y., Yamane, K., Yata, K., Yoshida, K., Yoshikawa, H., Zuber, U., Ogasawara, N., 2003. Essential Bacillus subtilis genes. Proc Natl Acad Sci U S A 100, 4678–4683. https://doi.org/10.1073/pnas.0730515100

Koo, B.-M., Kritikos, G., Farelli, J.D., Todor, H., Tong, K., Kimsey, H., Wapinski, I., Galardini, M., Cabal, A., Peters, J.M., Hachmann, A.-B., Rudner, D.Z., Allen, K.N., Typas, A., Gross, C.A., 2017. Construction and Analysis of Two Genome-scale Deletion Libraries for Bacillus subtilis. Cell Syst 4, 291-305.e7. https://doi.org/10.1016/j.cels.2016.12.013

Kuk, A.C.Y., Hao, A., Guan, Z., Lee, S.-Y., 2019. Visualizing conformation transitions of the Lipid II flippase MurJ. Nature Communications 10, 1736. https://doi.org/10.1038/s41467-019-09658-0

Kumar, S., Rubino, F.A., Mendoza, A.G., Ruiz, N., 2018. The bacterial lipid II flippase MurJ functions by an alternating-access mechanism. J. Biol. Chem. jbc.RA118.006099. https://doi.org/10.1074/jbc.RA118.006099

Leaver, M., Errington, J., 2005. Roles for MreC and MreD proteins in helical growth of the cylindrical cell wall in Bacillus subtilis. Mol. Microbiol. 57, 1196–1209. https://doi.org/10.1111/j.1365-2958.2005.04736.x

Levin, P.A., Margolis, P.S., Setlow, P., Losick, R., Sun, D., 1992. Identification of Bacillus subtilis genes for septum placement and shape determination. J. Bacteriol. 174, 6717–6728.

Liu, X., Biboy, J., Consoli, E., Vollmer, W., den Blaauwen, T., 2020. MreC and MreD balance the interaction between the elongasome proteins PBP2 and RodA. PLoS Genet 16, e1009276. https://doi.org/10.1371/journal.pgen.1009276

Liu, X., Meiresonne, N.Y., Bouhss, A., den Blaauwen, T., 2018. FtsW activity and lipid II synthesis are required for recruitment of MurJ to midcell during cell division in Escherichia coli. Molecular Microbiology 109, 855–884. https://doi.org/10.1111/mmi.14104

Luisier, F., Vonesch, C., Blu, T., Unser, M., 2010. Fast interscale wavelet denoising of Poisson-corrupted images. Signal Process. 90, 415–427. https://doi.org/10.1016/j.sigpro.2009.07.009

Mary, H., Rueden, C., Ferreira, T., 2016. KymographBuilder: Release 1.2.4. https://doi.org/10.5281/zenodo.56702

Mayer, J.A., Amann, K.J., 2009. Assembly properties of the Bacillus subtilis actin, MreB. Cell Motil. Cytoskeleton 66, 109–118. https://doi.org/10.1002/cm.20332

Meeske, A.J., Sham, L.-T., Kimsey, H., Koo, B.-M., Gross, C.A., Bernhardt, T.G., Rudner, D.Z., 2015. MurJ and a novel lipid II flippase are required for cell wall biogenesis in Bacillus subtilis. Proc. Natl. Acad. Sci. U.S.A. 112, 6437–6442. https://doi.org/10.1073/pnas.1504967112

Mercier, R., Kawai, Y., Errington, J., 2014. General principles for the formation and proliferation of a wall-free (L-form) state in bacteria. eLife 3, e04629. https://doi.org/10.7554/eLife.04629

Mignolet, J., Holden, S., Bergé, M., Panis, G., Eroglu, E., Théraulaz, L., Manley, S., Viollier, P.H., 2016. Functional dichotomy and distinct nanoscale assemblies of a cell cycle-controlled bipolar zinc-finger regulator. eLife 5. https://doi.org/10.7554/eLife.18647

Monds, R.D., Lee, T.K., Colavin, A., Ursell, T., Quan, S., Cooper, T.F., Huang, K.C., 2014. Systematic Perturbation of Cytoskeletal Function Reveals a Linear Scaling Relationship between Cell Geometry and Fitness. Cell Reports 9, 1528–1537. https://doi.org/10.1016/j.celrep.2014.10.040

Monteiro, J.M., Fernandes, P.B., Vaz, F., Pereira, A.R., Tavares, A.C., Ferreira, M.T., Pereira, P.M., Veiga, H., Kuru, E., VanNieuwenhze, M.S., Brun, Y.V., Filipe, S.R., Pinho, M.G., 2015. Cell shape dynamics during the staphylococcal cell cycle. Nat Commun 6, 8055. https://doi.org/10.1038/ncomms9055

Muchová, K., Chromiková, Z., Barák, I., 2013. Control of Bacillus subtilis cell shape by RodZ. Environ. Microbiol. 15, 3259–3271. https://doi.org/10.1111/1462-2920.12200

Münch, D., Sahl, H.-G., 2015. Structural variations of the cell wall precursor lipid II in Gram-positive bacteria — Impact on binding and efficacy of antimicrobial peptides. Biochimica et Biophysica Acta (BBA) - Biomembranes, Bacterial Resistance to Antimicrobial Peptides 1848, 3062–3071. https://doi.org/10.1016/j.bbamem.2015.04.014

Niklas, K.J., 2004. The Cell Walls that Bind the Tree of Life. BioScience 54, 831–841. https://doi.org/10.1641/0006-3568(2004)054[0831:TCWTBT]2.0.CO;2

Olshausen, P. v., Defeu Soufo, H.J., Wicker, K., Heintzmann, R., Graumann, P.L., Rohrbach, A., 2013. Superresolution Imaging of Dynamic MreB Filaments in B. subtilis—A Multiple-Motor-Driven Transport? Biophys J 105, 1171–1181. https://doi.org/10.1016/j.bpj.2013.07.038

Ouzounov, N., Nguyen, J.P., Bratton, B.P., Jacobowitz, D., Gitai, Z., Shaevitz, J.W., 2016. MreB Orientation Correlates with Cell Diameter in Escherichia coli. Biophys. J. 111, 1035–1043. https://doi.org/10.1016/j.bpj.2016.07.017

Özbaykal, G., Wollrab, E., Simon, F., Vigouroux, A., Cordier, B., Aristov, A., Chaze, T., Matondo, M., van Teeffelen, S., 2020. The transpeptidase PBP2 governs initial localization and activity of the major cell-wall synthesis machinery in E. coli. eLife 9, e50629. https://doi.org/10.7554/eLife.50629

Pasquina-Lemonche, L., Burns, J., Turner, R.D., Kumar, S., Tank, R., Mullin, N., Wilson, J.S., Chakrabarti, B., Bullough, P.A., Foster, S.J., Hobbs, J.K., 2020. The Architecture of the Gram Positive Bacterial Cell Wall. Nature 582, 294–297. https://doi.org/10.1038/s41586-020-2236-6

Pereira, A.C., Paiva, A., Saraiva, I.H., Costa, T., Henriques, A.O., Matzapetakis, M., 2015. Chemical shift assignments and secondary structure determination of the ectodomain of Bacillus subtilis morphogenic protein RodZ. Biomol NMR Assign 9, 285–288. https://doi.org/10.1007/s12104-014-9593-8

Reimold, C., Defeu Soufo, H.J., Dempwolff, F., Graumann, P.L., 2013. Motion of variable-length MreB filaments at the bacterial cell membrane influences cell morphology. Mol. Biol. Cell 24, 2340–2349. https://doi.org/10.1091/mbc.E12-10-0728

Reith, J., Mayer, C., 2011. Peptidoglycan turnover and recycling in Gram-positive bacteria. Appl. Microbiol. Biotechnol. 92, 1–11. https://doi.org/10.1007/s00253-011-3486-x

Reyes-Lamothe, R., Sherratt, D.J., 2019. The bacterial cell cycle, chromosome inheritance and cell growth. Nat Rev Microbiol 17, 467–478. https://doi.org/10.1038/s41579-019-0212-7

Salje, J., van den Ent, F., de Boer, P., Löwe, J., 2011. Direct Membrane Binding by Bacterial Actin MreB. Mol Cell 43, 478–487. https://doi.org/10.1016/j.molcel.2011.07.008

Sarkar, P., Yarlagadda, V., Ghosh, C., Haldar, J., 2017. A review on cell wall synthesis inhibitors with an emphasis on glycopeptide antibiotics †The authors declare no competing interests. Medchemcomm 8, 516–533. https://doi.org/10.1039/c6md00585c

Sassine, J., Pazos, M., Breukink, E., Vollmer, W., 2021. Lytic transglycosylase MltG cleaves in nascent peptidoglycan and produces short glycan strands. The Cell Surface 7, 100053. https://doi.org/10.1016/j.tcsw.2021.100053

Sauvage, E., Kerff, F., Terrak, M., Ayala, J.A., Charlier, P., 2008. The penicillin-binding proteins: structure and role in peptidoglycan biosynthesis. FEMS Microbiology Reviews 32, 234–258. https://doi.org/10.1111/j.1574-6976.2008.00105.x

Scheffers, D.-J., Jones, L.J.F., Errington, J., 2004. Several distinct localization patterns for penicillin-binding proteins in Bacillus subtilis. Mol. Microbiol. 51, 749–764.

Schindelin, J., Arganda-Carreras, I., Frise, E., Kaynig, V., Longair, M., Pietzsch, T., Preibisch, S., Rueden, C., Saalfeld, S., Schmid, B., Tinevez, J.-Y., White, D.J., Hartenstein, V., Eliceiri, K., Tomancak, P., Cardona, A., 2012. Fiji: an open-source platform for biological-image analysis. Nat Methods 9, 676–682. https://doi.org/10.1038/nmeth.2019

Shaevitz, J.W., Gitai, Z., 2010. The Structure and Function of Bacterial Actin Homologs. Cold Spring Harb Perspect Biol 2, a000364. https://doi.org/10.1101/cshperspect.a000364

Sham, L.-T., Butler, E.K., Lebar, M.D., Kahne, D., Bernhardt, T.G., Ruiz, N., 2014. Bacterial cell wall. MurJ is the flippase of lipid-linked precursors for peptidoglycan biogenesis. Science 345, 220–222. https://doi.org/10.1126/science.1254522

Shi, H., Bratton, B.P., Gitai, Z., Huang, K.C., 2018. How to Build a Bacterial Cell: MreB as the Foreman of E. coli Construction. Cell 172, 1294–1305. https://doi.org/10.1016/j.cell.2018.02.050

Shih, Y.-L., Le, T., Rothfield, L., 2003. Division site selection in Escherichia coli involves dynamic redistribution of Min proteins within coiled structures that extend between the two cell poles. PNAS 100, 7865–7870. https://doi.org/10.1073/pnas.1232225100

Sun, Y., Garner, E., 2022. PrkC kinase modulates MreB filament and bacteria growth by monitoring cell wall precursor lipid II. Biophysical Journal 121, 150a. https://doi.org/10.1016/j.bpj.2021.11.1974

Swulius, M.T., Chen, S., Jane Ding, H., Li, Z., Briegel, A., Pilhofer, M., Tocheva, E.I., Lybarger, S.R., Johnson, T.L., Sandkvist, M., Jensen, G.J., 2011. Long helical filaments are not seen encircling cells in electron cryotomograms of rod-shaped bacteria. Biochem. Biophys. Res. Commun. 407, 650–655. https://doi.org/10.1016/j.bbrc.2011.03.062

Taheri-Araghi, S., Bradde, S., Sauls, J.T., Hill, N.S., Levin, P.A., Paulsson, J., Vergassola, M., Jun, S., 2015. Cell-Size Control and Homeostasis in Bacteria. Current Biology 25, 385–391. https://doi.org/10.1016/j.cub.2014.12.009

Teeffelen, S. van, Wang, S., Furchtgott, L., Huang, K.C., Wingreen, N.S., Shaevitz, J.W., Gitai, Z., 2011. The bacterial actin MreB rotates, and rotation depends on cell-wall assembly. PNAS 108, 15822–15827. https://doi.org/10.1073/pnas.1108999108

Tesson, B., Dajkovic, A., Keary, R., Marlière, C., Dupont-Gillain, C.C., Carballido-López, R., 2022. Magnesium rescues the morphology of Bacillus subtilis mreB mutants through its inhibitory effect on peptidoglycan hydrolases. Sci Rep 12, 1137. https://doi.org/10.1038/s41598-021-04294-5

Thévenaz, P., Ruttimann, U.E., Unser, M., 1998. A pyramid approach to subpixel registration based on intensity. IEEE Trans Image Process 7, 27–41. https://doi.org/10.1109/83.650848

Tinevez, J.-Y., Perry, N., Schindelin, J., Hoopes, G.M., Reynolds, G.D., Laplantine, E., Bednarek, S.Y., Shorte, S.L., Eliceiri, K.W., 2017. TrackMate: An open and extensible platform for single-particle tracking. Methods, Image Processing for Biologists 115, 80–90. https://doi.org/10.1016/j.ymeth.2016.09.016

Tiyanont, K., Doan, T., Lazarus, M.B., Fang, X., Rudner, D.Z., Walker, S., 2006. Imaging peptidoglycan biosynthesis in Bacillus subtilis with fluorescent antibiotics. Proc Natl Acad Sci U S A 103, 11033–11038. https://doi.org/10.1073/pnas.0600829103

Tokunaga, M., Imamoto, N., Sakata-Sogawa, K., 2008. Highly inclined thin illumination enables clear single-molecule imaging in cells. Nat Methods 5, 159–161. https://doi.org/10.1038/nmeth1171

Turner, R.D., Mesnage, S., Hobbs, J.K., Foster, S.J., 2018. Molecular imaging of glycan chains couples cell-wall polysaccharide architecture to bacterial cell morphology. Nature Communications 9, 1263. https://doi.org/10.1038/s41467-018-03551-y

Typas, A., Banzhaf, M., Gross, C.A., Vollmer, W., 2012. From the regulation of peptidoglycan synthesis to bacterial growth and morphology. Nature Reviews Microbiology 10, 123–136. https://doi.org/10.1038/nrmicro2677

Typas, A., Banzhaf, M., Gross, C.A., Vollmer, W., 2011. From the regulation of peptidoglycan synthesis to bacterial growth and morphology. Nat Rev Microbiol 10, 123–136. https://doi.org/10.1038/nrmicro2677

van den Ent, F., Izoré, T., Bharat, T.A., Johnson, C.M., Löwe, J., 2014. Bacterial actin MreB forms antiparallel double filaments. eLife 3, e02634. https://doi.org/10.7554/eLife.02634

van Heijenoort, J., 2007. Lipid intermediates in the biosynthesis of bacterial peptidoglycan. Microbiol. Mol. Biol. Rev. 71, 620–635. https://doi.org/10.1128/MMBR.00016-07

van Teeffelen, S., Renner, L.D., 2018. Recent advances in understanding how rod-like bacteria stably maintain their cell shapes. F1000Res 7, 241. https://doi.org/10.12688/f1000research.12663.1

van Teeffelen, S., Wang, S., Furchtgott, L., Huang, K.C., Wingreen, N.S., Shaevitz, J.W., Gitai, Z., 2011. The bacterial actin MreB rotates, and rotation depends on cell-wall assembly. Proc Natl Acad Sci U S A 108, 15822–15827. https://doi.org/10.1073/pnas.1108999108

van Teeseling, M.C.F., de Pedro, M.A., Cava, F., 2017. Determinants of Bacterial Morphology: From Fundamentals to Possibilities for Antimicrobial Targeting. Front. Microbiol. 8. https://doi.org/10.3389/fmicb.2017.01264

VanNieuwenhze, M.S., Mauldin, S.C., Zia-Ebrahimi, M., Aikins, J.A., Blaszczak, L.C., 2001. The Total Synthesis of Lipid I. J. Am. Chem. Soc. 123, 6983–6988. https://doi.org/10.1021/ja016082o

Vollmer, W., Blanot, D., de Pedro, M.A., 2008. Peptidoglycan structure and architecture. FEMS Microbiol Rev 32, 149–167. https://doi.org/10.1111/j.1574-6976.2007.00094.x

Vollmer, W., Seligman, S.J., 2010. Architecture of peptidoglycan: more data and more models. Trends Microbiol. 18, 59–66. https://doi.org/10.1016/j.tim.2009.12.004

Ward, J.B., 1973. The chain length of the glycans in bacterial cell walls. Biochemical Journal 133, 395–398. https://doi.org/10.1042/bj1330395

Wei, Y., Havasy, T., McPherson, D.C., Popham, D.L., 2003. Rod shape determination by the Bacillus subtilis class B penicillin-binding proteins encoded by pbpA and pbpH. J Bacteriol 185, 4717–4726. https://doi.org/10.1128/jb.185.16.4717-4726.2003

Welte, M.A., 2004. Bidirectional Transport along Microtubules. Current Biology 14, R525–R537. https://doi.org/10.1016/j.cub.2004.06.045

Westfall, C.S., Levin, P.A., 2017. Bacterial Cell Size: Multifactorial and Multifaceted. Annu. Rev. Microbiol. 71, 499–517. https://doi.org/10.1146/annurev-micro-090816-093803

Whatmore, A.M., Reed, R.H., 1990. Determination of turgor pressure in Bacillus subtilis: a possible role for K+ in turgor regulation. J. Gen. Microbiol. 136, 2521–2526. https://doi.org/10.1099/00221287-136-12-2521

Whitley, K.D., Jukes, C., Tregidgo, N., Karinou, E., Almada, P., Cesbron, Y., Henriques, R., Dekker, C., Holden, S., 2021. FtsZ treadmilling is essential for Z-ring condensation and septal constriction initiation in Bacillus subtilis cell division. Nat Commun 12, 2448. https://doi.org/10.1038/s41467-021-22526-0

Whitley, K.D., Middlemiss, S., Jukes, C., Dekker, C., Holden, S., 2022. High-resolution imaging of bacterial spatial organization with vertical cell imaging by nanostructured immobilization (VerCINI). Nat Protoc 17, 847–869. https://doi.org/10.1038/s41596-021-00668-1

Wu, L.J., Errington, J., 2011. Nucleoid occlusion and bacterial cell division. Nat Rev Microbiol 10, 8–12. https://doi.org/10.1038/nrmicro2671

Yoshii, Y., Niki, H., Shiomi, D., 2019. Division-site localization of RodZ is required for efficient Z ring formation in Escherichia coli. Mol. Microbiol. https://doi.org/10.1111/mmi.14217

Yunck, R., Cho, H., Bernhardt, T.G., 2016. Identification of MltG as a potential terminase for peptidoglycan polymerization in bacteria. Mol Microbiol 99, 700–718. https://doi.org/10.1111/mmi.13258

Zhang, B., Gao, Y., Zhang, L., Zhou, Y., 2021. The plant cell wall: Biosynthesis, construction, and functions. Journal of Integrative Plant Biology 63, 251–272. https://doi.org/10.1111/jipb.13055

Zielińska, A., Savietto, A., de Sousa Borges, A., Martinez, D., Berbon, M., Roelofsen, J.R., Hartman, A.M., de Boer, R., Van der Klei, I.J., Hirsch, A.K., Habenstein, B., Bramkamp, M., Scheffers, D.-J., 2020. Flotillin-mediated membrane fluidity controls peptidoglycan synthesis and MreB movement. eLife 9, e57179. https://doi.org/10.7554/eLife.57179

Chapter 8: Appendix

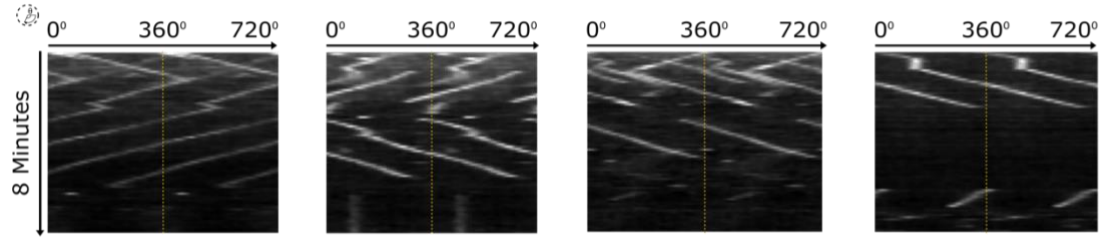

Figure 8.1. Further examples of kymographs presented in **Figure 3.2**.

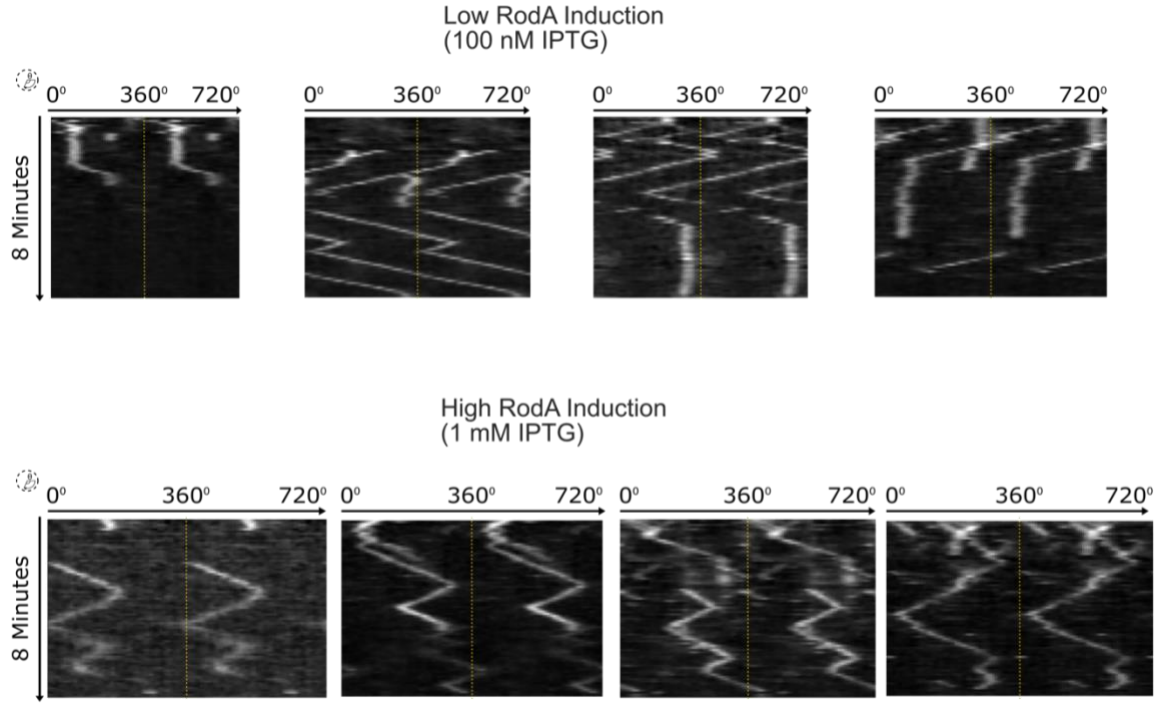

Figure 8.2. Further examples of kymographs presented in **Figure 5.3**.